ETH zürich

DLR

Hybrid AI–Physical Modeling in Interferometric SAR

Bridging Data-Driven and Physics-Based Approaches for Enhanced Parameter Retrieval

Islam Mansour

2025

Diss. ETH No. 31267

DISS. ETH NO. 31267

HYBRID AI–PHYSICAL MODELING IN INTERFEROMETRIC SAR

BRIDGING DATA-DRIVEN AND PHYSICS-BASED APPROACHES FOR ENHANCED PARAMETER RETRIEVAL

A thesis submitted to attain the degree of

DOCTOR OF SCIENCES

(Dr. sc. ETH Zurich)

PRESENTED BY

ISLAM MANSOUR

born on 01.03.1993

accepted on the recommendation of

Prof. Dr. Irena Hajnsek

Dr. Ronny Hänsch

Prof. Anna Hogg

Prof. Dr. Ralph Dubayah

2025

Islam Mansour

Hybrid AI–Physical Modeling in Interferometric SAR: Bridging Data-Driven and Physics-Based Approaches for Enhanced Parameter Retrieval,

DOI: 10.3929/ethz-c-000783509

Dedicated to my parents and grandparents,
for their unwavering belief in me,
for giving me opportunities they never had,
to the soil and the Nile of Egypt, where the journey began,
and to all who inspired this work along the journey of life.

Gewidmet meinen Eltern und Großeltern,
für ihren unerschütterlichen Glauben an mich,
für die Chancen, die sie mir ermöglicht haben
und selbst nie hatten,
dem Boden und dem Nil Ägyptens, wo die Reise begann,
und allen, die diese Arbeit auf dem Weg des Lebens inspiriert haben.

إهداء إلى والديّ وأجدادي،
لإيمانهم الثابت بي،
ولإتاحتهم لي الفرص التي لم تُتح لهم،
وإلى تراب مصر ونيلها، حيث بدأت الرحلة،
وإلى كل من ألهم هذا العمل في رحلة الحياة.

"Knowledge that does not take you beyond yourself is far worse than ignorance."
— Ibn ʿArabī

ABSTRACT

Interferometric Synthetic Aperture Radar (InSAR) has become an essential remote sensing tool for retrieving glacier surface elevation and forest parameters, both of which are recognized as Essential Climate Variables (ECVs) by the Global Climate Observing System (GCOS). Its all-weather, day-and-night capability and global coverage make it particularly valuable for long-term Earth observation. The retrieval of geo- and biophysical parameters from InSAR traditionally relies on electromagnetic scattering models that describe how radar waves interact with Earth's surfaces and targets, such as the Random Volume over Ground (RVoG) model for forests and the Uniform Volume model for glacier penetration. While physics-based models offer valuable, domain-consistent interpretations, their dependence on simplified assumptions can limit accuracy and introduce systematic biases, especially when dealing with underdetermined or ill-posed inverse problems. In contrast, machine learning (ML) approaches excel at modeling empirical relationships in multi-dimensional feature spaces but suffer from poor generalization and limited physical interpretability. This cumulative thesis introduces hybrid AI-physical modeling frameworks that leverage both the domain knowledge of physical models and the adaptability of machine learning to enhance TanDEM-X InSAR parameter retrieval in forest and glacier environments.

Hybrid modeling—also known as semi-parametric modeling—merges physically interpretable models with data-driven components to capture complex, nonlinear relationships. This approach has improved extrapolation capabilities and enhanced interpretability, at least since the early 1990s, across various scientific domains. This thesis extends the hybrid modeling paradigm to InSAR-based parameter retrieval, embedding domain knowledge into the learning process to enable more accurate and physically consistent estimates. The proposed frameworks overcome the limitations of purely physical or machine learning models while maintaining interpretability and generalizability.

The research comprises three interconnected studies that progressively develop and validate the hybrid modeling approach. The first study introduces a foundational framework for forest height estimation using single-baseline, single-polarization TanDEM-X interferometric coherence. A multilayer perceptron (MLP) predicts the coefficients of a vertical reflectivity profile—parameterized by Legendre polynomials—from InSAR measurements and topographic descriptors, which subsequently drive a physical inversion model. Validation across tropical forest sites demonstrates the method's ability to generalize across diverse acquisition geometries while maintaining physical consistency.

The second study builds upon the framework and integrates Landsat multi-spectral features into the feature input space to assess the improved performance of multi-modality. Beyond physically interpretable variables, the hybrid model allows for accounting for subtle variations in forest structure that InSAR data alone do not resolve. In this case, incorporating optical data improves the forest height estimates, with quantitative evaluations showing a reduction in Root Mean Square Error (RMSE) by 13.5% and Mean Absolute Error (MAE) by 16.6% compared to the hybrid model using InSAR features alone.

The third study extends the hybrid approach to cryospheric applications, developing a hybrid framework for correcting penetration bias in InSAR-derived digital elevation models over the Greenland Ice Sheet. The method combines parametric vertical scattering profiles (Exponential and Weibull) with an MLP that predicts profile parameters from InSAR features. Validation against NASA IceBridge Airborne Topographic Mapper (ATM) data shows that the hybrid Exponential model achieves elevation errors of 0.52 m while maintaining robustness across unseen acquisition geometries. These improvements demonstrate the advantages of embedding physical knowledge within data-driven models.

This thesis establishes hybrid AI-physical modeling as a scalable and transferable framework for estimating geophysical and biophysical parameters from InSAR data. The proposed methods directly apply to ongoing and upcoming satellite missions, including TanDEM-X, GEDI, and ESA Biomass. Through the physically consistent integration of multi-modal data sources—including radar, optical, and LiDAR—this work advances the development

of interpretable and generalizable parameter retrieval methods that maintain physical knowledge while adapting to real-world complexity.

ZUSAMMENFASSUNG

Das Interferometrische Synthetic Aperture Radar (InSAR) hat sich zu einem unverzichtbaren Fernerkundungsinstrument für die Ableitung der Oberflächentopographie von Gletschern und von Waldparametern entwickelt – beides Schlüsselgrößen, die vom Global Climate Observing System (GCOS) als Essential Climate Variables (ECVs) anerkannt sind. Aufgrund seiner Fähigkeit zur wetterunabhängigen, tag- und nachtaktiven Datenerfassung mit globaler Abdeckung eignet sich InSAR besonders für die langfristige Erdbeobachtung. Obwohl physikalische Modelle eine hohe Interpretierbarkeit und konsistente Ergebnisse innerhalb ihrer Domäne liefern, schränken vereinfachende Annahmen ihre Genauigkeit ein und können insbesondere bei unterbestimmten oder schlecht gestellten inversen Problemen systematische Fehler verursachen. Im Gegensatz dazu zeichnen sich Methoden des maschinellen Lernens (ML) durch ihre Fähigkeit aus, empirische Zusammenhänge in hochdimensionalen Merkmalsräumen zu modellieren, leiden jedoch unter begrenzter Generalisierbarkeit und eingeschränkter physikalischer Interpretierbarkeit. Diese kumulative Dissertation verbindet beide Paradigmen durch die Entwicklung hybrider Modellierungsansätze, die die Robustheit physikalischer Modelle mit der Anpassungsfähigkeit datengetriebener ML-Methoden kombinieren. Ziel ist es, die Ableitung geophysikalischer Parameter aus TanDEM-X-InSAR-Daten in bewaldeten und vergletscherten Umgebungen zu verbessern.

Hybride Modellierung – häufig als semi-parametrische hybride Modellierung bezeichnet – verknüpft explizit physikalisch interpretierbare Modelle, die auf grundlegenden Prinzipien beruhen, mit datengetriebenen Komponenten, die komplexe, nichtlineare Zusammenhänge erfassen. Dieses Konzept entstand Anfang der 1990er Jahre und wurde seither in verschiedenen wissenschaftlichen Anwendungen eingesetzt. Es zeigte Vorteile wie verbesserte Extrapolationsfähigkeit, geringeren Datenbedarf und erhöhte Interpretierbarkeit. Im Kontext der InSAR-basierten Ableitung geo- und biophysikalischer Parameter zielt diese Arbeit darauf ab, das

hybride Modellierungskonzept weiterzuentwickeln, um datengetriebene und physikalische Ansätze für eine verbesserte Parameterschätzung miteinander zu verbinden. Durch die Einbettung von Domänenwissen in den Lernprozess überwinden die vorgeschlagenen Frameworks die Einschränkungen rein physikalischer oder ausschließlich ML-basierter Modelle und ermöglichen eine genauere, interpretierbare und besser generalisierbare Rückführung wichtiger InSAR-Parameter.

Die erste Studie stellt ein hybrides Modell zur Schätzung der Waldhöhe vor, das auf Kohärenz Daten einer Basislinie und einer Polarisation von TanDEM-X basiert. Ein Multilayer-Perceptron (MLP) wird trainiert, um die Koeffizienten eines vertikalen Reflektivitätsprofils – parametrisiert durch Legendre-Polynome – ausschließlich aus InSAR-Messungen und topographischen Merkmalen vorherzusagen. Dieses Profil wird anschließend in ein physikalisches Modell eingebettet, um die Waldhöhe zu invertieren. Validierungen an tropischen Waldstandorten mit unterschiedlichen Aufnahmegeometrien zeigen, dass der Ansatz gute Generalisierungseigenschaften aufweist, ohne die physikalische Konsistenz zu verlieren.

Die zweite Studie erweitert das hybride Modell, indem multispektrale, optische Merkmale aus Landsat-Bilddaten in den Merkmalsraum integriert werden. Obwohl diese Merkmale nicht direkt über physikalische Zusammenhänge mit der Waldhöhe in Verbindung gebracht werden können, erweitern sie den Merkmalsraum über physikalisch interpretierbare Größen hinaus. Dadurch kann die ML-Komponente latente, nicht offensichtliche Muster und Zusammenhänge in mehrdimensionalen Datenräumen erkennen, die strukturelle Defizite des ursprünglichen Modells kompensieren, welches ausschließlich auf TanDEM-X-Merkmalen basiert. Die Studie untersucht, inwieweit diese zusätzlichen Merkmale die Vorhersageleistung und Generalisierbarkeit verbessern. Die Ergebnisse zeigen signifikante Leistungssteigerungen, insbesondere in topographisch komplexen oder geometrisch mehrdeutigen Szenarien.

Die dritte Studie wendet das hybride Modellierungskonzept auf die Schätzung der Signaleindringtiefe in InSAR-abgeleiteten digitalen Höhenmodellen über dem grönländischen Eisschild an. Hierzu wird ein physikalisch informiertes ML-Framework vorgestellt, das Höhenabweichungen aufgrund des Eindringens der Radarsignale

in Schnee und Eis korrigiert. Die Methode kombiniert parametrische vertikale Streuprofildarstellungen (exponentiell und Weibull) mit einem MLP, das deren Parameter aus InSAR-Merkmalen vorhersagt. Experimente mit unterschiedlichen Trainingsszenarien – von Interpolation bis Extrapolation – zeigen, dass das hybride Modell geringere Fehler und eine bessere Generalisierbarkeit erzielt als rein physikalische oder rein datengetriebene Ansätze.

Diese Arbeit etabliert hybride KI–physikalische Modellierung als skalierbares und übertragbares Framework zur Ableitung geophysikalischer Parameter aus InSAR-Daten. Die vorgeschlagenen Methoden sind unmittelbar auf aktuelle und kommende Satellitenmissionen wie TanDEM-X, GEDI und ESA Biomass anwendbar. Durch die physikalisch konsistente Integration multimodaler Datenquellen – einschließlich Radar-, optischer und LiDAR-Daten – stellt diese Arbeit einen ersten Ansatz dar, um die hybride Modellierung gezielt für die Ableitung geophysikalischer Parameter aus InSAR-Daten zu entwickeln, mit dem Ziel, domänenübergreifend interpretierbare, generalisierbare und physikalisch fundierte Modelle zu schaffen.

ACKNOWLEDGEMENTS

This work would not have been possible without significant support from many people. I am deeply grateful for the continuous guidance and encouragement from Irena, Georg, and Ronny, particularly during the challenging final months. Special thanks to Irena for her final push in the last few days and to Georg for his concise and valuable feedback. Thanks to Michael for offering me the position at UniBw while allowing me to work on my thesis. I also extend my sincere appreciation to Ralph Dubayah and Anna E. Hogg for agreeing to review this thesis, and I wish Matthias Braun a speedy recovery. I am very grateful to Karin Schneider from the Doctoral Administration at ETH for her prompt responses to my emails and her exceptional support in facilitating the administrative processes.

I am deeply grateful to Kostas, whom I met at the DPG Frühjahrstagungen 2019—an encounter that introduced me to the group and connected me with Irena and Giuseppe. This meeting eventually led to my master's thesis at TUM, where Michael Eineder and Richard Bamler first opened my eyes to the world of SAR. Kostas has continually challenged and inspired me to refine my scientific thinking and reasoning. His passion for new ideas—and for espresso—was infectious. I fondly recall our long walks and shared activities in Zurich with Irena and Nikita.

I also thank Alberto Moreira for his invaluable support, genuine care, and dedication to all PhD students.

My heartfelt thanks go to my colleagues of the PolInSAR group at DLR and the Earth Observation group at ETH. Special thanks to Ronny, Georg, and Noelia for their steady support, and to Noelia and her family for their warm hospitality in Alicante. I am grateful to Thomas for our lively discussions, Nikita and Roman for their companionship in group activities and hikes, Lea for the memorable sailing at Chiemsee, Ben for introducing me to sailplane, and Kristina for the cheerful chats. Patricia's cakes brightened many days. I also thank Paloma for the shared DLR courses, Changhyun

for being a great office mate, and Subhadip for the spontaneous adventures.

I would like to thank Anastasia, Jose Luis, Paola, Daniel, Ragini, Sergio, Dominik, Simon, and Sindhu for their friendship and support, and Fairouz for sharing the office with me during my last months at DLR. I am also grateful to many others at DLR for their kindness and collegial spirit.

At DLR, I had the privilege of serving on the PhD candidates' council (Promovierendenvertretung), advocating for doctoral researchers—especially international ones—in collaboration with the international office, the DLR board (with Anke Kaysser-Pyzalla), and Helmholtz Juniors.

I am grateful to Christoph and Philipp for their IT support, and to the TerraByte team and the Leibniz Supercomputing Center for providing the computational resources essential to this work.

Thanks to my friends Arshad, Mohamed, Sherif, and many others with whom I shared the revolutionary days in Egypt, experiences I deeply cherish. My most profound appreciation goes to my mother and father for their patience and support and for granting me the freedom to travel and pursue my ambitions despite the difficulty of being away from them and seeing them grow older. I am grateful to them for providing me with opportunities to pursue my education, which they were unable to achieve in their lives. Thanks to my grandmother, I had a beautiful childhood with her before she passed away. I am grateful to my grandparents, who have shaped my life with their kindness and good hearts. Finally, I would like to thank my family, including my mother, father, grandmother, Eman, Amir, and Ildikó, for their invaluable support and kind hearts.

To everyone I have crossed paths with during this journey: thank you. This section cannot begin to list you all, but I carry your support and impact with me.

With love to all.

"Let yourself be silently drawn by the strange pull of what you really love. It will not lead you astray."

— Jalāl al-Dīn Rūmī

CONTENTS

ACRONYMS

AGB	Above-Ground Biomass.
AI	Artificial Intelligence.
ALOS-2	Advanced Land Observing Satellite-2.
ATM	Airborne Topographic Mapper.
BIOMASS	Biomass Observation Mission for Information, Assessment, Science and Services.
C-band	Radar C-band (4–8 GHz).
CryoSat-2	Cryosphere Satellite-2.
DEM	Digital Elevation Model.
DL	Deep Learning.
DLR	German Aerospace Center.
DSM	Digital Surface Model.
DTM	Digital Terrain Model.
ECV	Essential Climate Variable.
ESA	European Space Agency.
GCOS	Global Climate Observing System.
GEDI	Global Ecosystem Dynamics Investigation.
Harmony	ESA Earth Explorer Mission for Monitoring Earth's Surface Dynamics.
HoA	Height of Ambiguity.
IceBridge	NASA's Operation IceBridge.
ICESat-2	Ice, Cloud, and land Elevation Satellite 2.
InSAR	Interferometric Synthetic Aperture Radar.
Landsat	NASA–USGS Earth Observation Satellite Program.
L-band	Radar L-band (1–2 GHz).
LiDAR	Light Detection and Ranging.

LVIS	Land, Vegetation, and Ice Sensor.
ML	Machine Learning.
MLP	Multi-Layer Perceptron.
NASA	National Aeronautics and Space Administration.
NISAR	NASA–ISRO Synthetic Aperture Radar Mission.
P-band	Radar P-band (225–390 MHz; long-wavelength microwave band).
Pol-InSAR	Polarimetric-Interferometric SAR.
PolSAR	Polarimetric SAR.
REDD+	Reducing Emissions from Deforestation and forest Degradation, and the role of conservation, sustainable management of forests, and enhancement of forest carbon stocks.
RV	Random Volume.
RVoG	Random Volume over Ground Model.
SAR	Synthetic Aperture Radar.
S-band	Radar S-band (2–4 GHz).
Sentinel-1	Copernicus Sentinel-1 (C-band SAR Mission).
SLC	Single Look Complex.
S-RVoG	Random Volume over Ground Model with slope.
TanDEM-X	TerraSAR-X add-on for Digital Elevation Measurements.
TDX	TanDEM-X.
TSX	TerraSAR-X.
X-band	Radar X-band (8–12 GHz).

Part I

Foundations and Background

1

INTRODUCTION

Climate change is one of the most critical issues facing our time, necessitating accurate and continuous monitoring of Earth's ecosystems. Global changes can be largely observed using remote sensing technologies, particularly through spaceborne systems. Both forest structure and ice sheet elevation are among the most important Earth observation parameters related to the impacts of climate change, influencing the carbon cycle as well as global mass balance.

Forest height, a key structural parameter, serves as a crucial proxy for Above-Ground Biomass (AGB), which the Global Climate Observing System (GCOS) recognizes as an Essential Climate Variable (ECV) [1]. Accurate forest height measurements enable a better understanding of carbon storage, biodiversity patterns, and the impacts of deforestation [2], [3]. Similarly, precise elevation measurements of ice sheets—another GCOS-defined ECV—provide critical data for assessing global mass balance and projecting sea-level changes. These measurements provide an asset for climate adaptation strategies and local-global policy decisions [4], [5].

1.1 MOTIVATION AND RELEVANCE

The motivation for this thesis is both scientific and application-driven: reliable, physically consistent retrievals of forest height and ice-sheet elevation are indispensable for understanding and predicting Earth system change. Both variables are recognized by the GCOS as ECVs [1]; systematic errors in their estimation propagate into carbon budget assessments, cryospheric mass balance, and ultimately climate model evaluation, as well as risk-informed adaptation and mitigation planning [4]. The technological developments pursued here—hybrid AI–physical models for Interferometric Synthetic Aperture Radar (InSAR)—are therefore motivated by the need to reduce these uncertainties in ways that remain interpretable, scalable, and traceable to first principles.

FORESTS AND THE CARBON CYCLE. Forest height underpins wall-to-wall estimation of AGB, change detection, and biodiversity-relevant structure [2], [3]. Single-baseline InSAR forest height inversions, however, are ill-posed and sensitive to canopy architecture, terrain, and acquisition geometry, which induces systematic biases—particularly in tall, structurally heterogeneous tropical forests, where uncertainties are higher [6]. Improving retrieval fidelity and generalization directly supports questions regarding succession, degradation, recovery, and spatial heterogeneity of carbon fluxes relevant to Reducing Emissions from Deforestation and forest Degradation, and the role of conservation, sustainable management of forests, and enhancement of forest carbon stocks (REDD+) monitoring and ecosystem policy.

ICE SHEETS AND SEA-LEVEL RISE. Over snow and ice, X-band penetration into firn shifts the effective scattering phase center below the physical surface, thereby biasing elevation unless corrected. The magnitude of this penetration bias can reach meters and varies with microphysical properties (density, grain size, layering, liquid water content) and season [7], [8], [9], [10]. Inconsistent corrections introduce systematic errors into elevation change and mass balance estimates, propagating uncertainty into sea-level projections used for coastal risk assessment [4]. Methods that capture the governing physics while adapting to spatial and temporal variability are therefore essential for credible cryospheric indicators.

WHY A HYBRID APPROACH. Purely physical models offer interpretability but rely on simplifying assumptions regarding vertical scattering and reflectivity profiles, which limit their transferability. Conversely, purely data-driven models can capture complex relationships but may violate physical constraints and perform poorly with imbalanced datasets. By embedding physical constraints within flexible learning, hybrid modeling addresses the shared bottleneck in both forests and ice: linking observed interferometric coherence to a physically plausible vertical profile under single-baseline constraints and propagating that link to parameters of scientific interest (forest height; penetration-corrected elevation). The innovations developed here are therefore positioned as methodological instruments in support of process-level Earth

system science, aligned with GCOS/IPCC priorities for actionable and scalable ECVs [1], [4].

Over the past two decades, InSAR has become essential for retrieving geo- and biophysical parameters such as surface elevation, glacial topography, and forest structure [11], [12], [13]. These measurements are crucial for understanding the impacts of climate change. They also support natural resource management and environmental monitoring on a global scale. As the first and only bistatic radar interferometer in space, the TanDEM-X mission from the German Aerospace Center (DLR) marks a turning point in the evolution of InSAR-based Earth Observation. Its unique configuration of two satellites — TerraSAR-X (TSX) and TanDEM-X (TDX) — flying in close formation has established new standards in interferometric measurements by eliminating temporal decorrelation effects. This capability has enabled unprecedented accuracy in global digital elevation models and opened new possibilities for monitoring dynamic Earth processes [14], [15].

At first glance, forest height estimation and ice-sheet elevation may appear to be unrelated challenges. However, both involve similar issues—volume scattering, baseline limitations, and model assumptions—that affect the reliability of physical parameter retrieval. More accurate retrievals directly support real-world needs: for forests, they inform estimates of carbon stocks and impacts on biodiversity; for ice sheets, they enhance mass-balance calculations, which are essential for sea-level projections. The subsequent sections illustrate how both domains benefit from the hybrid AI modeling approach, which bridges data-driven techniques with physical modeling in a unified framework for InSAR parameter retrieval.

1.1.1 *Forest Height Estimation*

In forest applications, TanDEM-X provides valuable single-baseline measurements that have revolutionized our ability to monitor forest structure globally. However, the complex nature of forest environments presents inherent challenges for any single-baseline system. For example, a single baseline configuration faces fundamental physical limitations in regions such as Gabon, which has highly diverse natural forests with heights ranging from a few meters to

over 50 meters [16]. The relationship between the interferometric phase and forest height varies significantly across this range, affecting measurement sensitivity. This interaction creates an inherent trade-off where the single baseline, while optimal for global Digital Elevation Model (DEM) generation, results in varying sensitivity to height variations depending on forest height [17], [18], [19]. This natural variation in forest structure leads to systematic biases in height estimates, typically resulting in underestimations for taller forests and overestimations for shorter ones [6]. While multi-baseline observations would be ideal for addressing these challenges, such space-borne mission capabilities do not currently exist. Thus, the limited solution space necessitates simplification of the underlying forest structure, which is reflected in the parameterization of the vertical reflectivity profile.

Advanced methodologies combining TanDEM-X data with other sources, such as Global Ecosystem Dynamics Investigation (GEDI), have demonstrated promising results in improving the accuracy of forest height estimation. These approaches have performed well in complex tropical environments, where traditional methods alone are insufficient and often introduce larger biases [6], [16], [20], [21]. Recent advancements in machine learning and deep learning techniques have demonstrated the potential to estimate forest height directly using TanDEM-X features [22], [23], [24]. However, these methods often lack the integration of domain knowledge into the learning process, thereby limiting their generalizability and transferability for application to specific sites or regions.

1.1.2 *Snow and Ice Interactions*

In snow and ice environments, X-band radar signals interact with the medium in complex ways, leading to signal penetration and resulting in systematic elevation biases—known as penetration biases—that vary significantly with snow conditions. Recent studies have shown that penetration biases can reach several meters, significantly affecting elevation measurements in polar regions [7], [8], [9], [10]. The interaction of microwaves with natural snow cover is particularly complex because snow consists of heterogeneous mixtures of ice grains and air, whose properties are dynamically influenced by environmental conditions such as temperature and

metamorphic processes [25]. These fundamental physical characteristics result in penetration biases that vary considerably with snow density, moisture content, and seasonal conditions, presenting challenges comparable to those encountered in forest height estimation.

Traditional approaches to addressing these biases have relied on empirical corrections or simplified physical models. However, these methods often struggle to capture the full complexity of snow-ice interactions. Physical models require detailed knowledge of snow properties that are often unavailable at the necessary spatial and temporal scales. Empirical corrections, while practical, may not adequately account for the dynamic nature of snow conditions and their impact on radar penetration. Recent data-driven approaches have shown promise in modeling penetration bias directly from the observation space; however, similar to their forest counterparts, they often lack physical constraints and face challenges in generalization [7], [26].

The challenges in snow/ice and forest applications highlight a common requirement: methods capable of parameter retrieval in complex, dynamic environments while maintaining physical consistency. These challenges present an opportunity to develop more sophisticated methodological frameworks designed to effectively address these limitations.

1.1.3 *Research Context and Opportunities*

Machine Learning (ML) has emerged as a promising alternative for addressing these limitations in both forest and cryosphere applications. By leveraging large datasets and powerful computational algorithms, ML approaches can learn data-driven mappings from input features to target variables, offering significant adaptability and flexibility. However, these methods often struggle with interpretability and generalization, particularly in inverse problems such as parameter retrieval, where incorporating domain knowledge and physical constraints is crucial. Without these constraints, ML models risk producing results that are inconsistent with established physical principles, thereby limiting their utility in real-world applications.

To overcome these challenges, a hybrid framework that combines the strengths of physical modeling and machine learning has gained traction. By embedding physical constraints into the learning process, hybrid approaches capitalize on the adaptability of ML while preserving the interpretability and rigor of physical models. This integration enables the development of models that can generalize across diverse scenarios and conditions, ultimately improving the accuracy and reliability of geo- and biophysical parameter retrieval. For example, hybrid methods can address systematic biases in forest height estimation and penetration biases in snow-covered regions by leveraging both data-driven insights and physical principles.

This thesis builds on this emerging paradigm, proposing a hybrid AI–physical modeling framework tailored for InSAR parameter retrieval. By bridging data-driven and physics-based approaches, it addresses critical gaps in the current state-of-the-art, offering a path toward more accurate, robust, and interpretable models. The proposed framework has the potential to advance the remote sensing field and contribute to broader environmental and climate research efforts, where reliable and precise geo- and bio-physical measurements are essential yet constrained by the availability of reference data.

1.2 BACKGROUND AND RELATED WORK

1.2.1 *Synthetic Aperture Radar (SAR)*

Synthetic Aperture Radar (SAR) represents an active microwave remote sensing technology that has revolutionized Earth observation capabilities since its inception in the 1950s [27]. Operating independently of solar illumination and largely unaffected by atmospheric conditions, SAR systems transmit electromagnetic pulses at microwave frequencies—typically X-band (8-12 GHz), C-band (4-8 GHz), or L-band (1-2 GHz)—and record the backscattered signals from Earth's surface [11], [28]. The SAR principle utilizes the platform's motion to create a synthesized large antenna aperture, enabling high spatial resolution through the coherent processing of received signals. This synthetic aperture technique enables high resolution in the azimuth (along-track) direction, while the pulse

bandwidth determines range (across-track) resolution [29]. The complex-valued SAR measurements contain both amplitude and phase: the amplitude corresponds to the physical backscattering intensity from the target and is influenced by surface roughness, geometry, and dielectric properties; the phase encodes the two-way travel path length from the sensor to the target, precise to a fraction of the wavelength [30]. Modern spaceborne SAR systems (e.g., TanDEM-X, Sentinel-1, and ALOS-2) operate with resolutions ranging from sub-meter to tens of meters and are widely used for a full range of applications, including topographic mapping, deformation monitoring, and environmental assessment [14], [31]. The coherent nature of SAR measurements—particularly the preservation of phase information—is the basis for more advanced techniques such as interferometry, polarimetry, and tomography, which provide three-dimensional imaging [32], [33], [34].

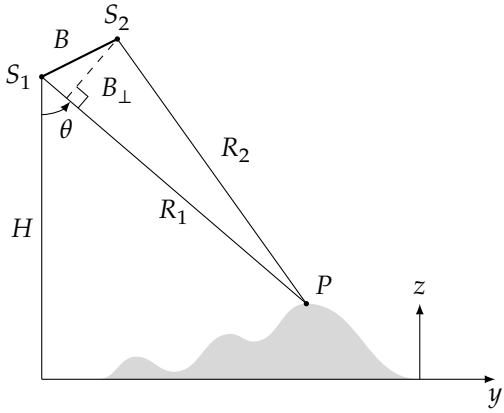

Figure 1.1: Illustration of Interferometric SAR acquisition geometry. The radar platform positions S_1 and S_2 are shown, connected by the baseline B with a perpendicular component $B_\perp$. The range vectors R_1 and R_2 extend from the radar platforms to the target P. The incidence angle θ and altitude H are also indicated.

1.2.2 *Radar Interferometry*

Radar interferometry leverages the phase of radar signals—typically from Synthetic Aperture Radar (SAR)—to detect subtle changes in the distance between the sensor and the Earth's surface. Here, we focus on across-track InSAR, where two complex-valued radar images are acquired from slightly different positions across-track [32], [35], [36], [37]. This configuration, utilizing either two antennas (single-pass) or two satellite passes (repeat-pass), allows the same scene to be observed from different viewing geometries (across-track baselines) that are perpendicular to the flight path (see Figure 1.1).

A prominent example of single-pass interferometry is the TanDEM-X mission, which consists of two satellites—TSX and TDX—flying in close formation [13], [14], [38]. This bistatic configuration enables the simultaneous acquisition of SAR images from slightly offset positions across the track, effectively eliminating temporal decorrelation. Consequently, it facilitates precise and consistent phase measurements. This capability makes TanDEM-X especially well-suited for generating high-resolution global DEMs and for applications such as estimating forest height [14], [39].

The resulting phase difference between the two images is directly related to the surface topography. This phase-to-height mapping technique was first proposed by Graham [35]. For further details, we refer the reader to [32], [40], [41].

When the acquisitions are simultaneous, it is termed single-pass interferometry; when they are acquired sequentially with a temporal separation, it is referred to as repeat-pass interferometry. The sensitivity of the interferometric phase to surface height depends on the effective spatial baseline. It is expressed through the vertical wavenumber κ_z, defined as:

$$\kappa_z = m\frac{2\pi}{\lambda}\frac{B_\perp}{R_1 \sin(\theta)}, \tag{1.1}$$

where θ is the incidence angle, $B_\perp$ is the perpendicular baseline component, λ is the radar wavelength, R_1 is the slant range, and m is a factor that equals 2 for monostatic and 1 for bistatic acquisitions.

The Height of Ambiguity (HoA) represents the elevation change corresponding to a full 2π phase shift and is defined as:

$$HoA = \frac{2\pi}{\kappa_z}. \tag{1.2}$$

1.2.3 *Interferometric Coherence*

Interferometric coherence measures the statistical similarity of two signals, which is the correlation between two SAR images for given pixels. The underlying scattering mechanisms influence this measure, rendering coherence not only a quality metric but also a valuable source of information regarding surface and subsurface properties. We can utilize it to evaluate the quality of the interferometric measurements. The measured interferometric coherence ($\tilde{\gamma}$) between two interferometric images s_1 and s_2 is expressed as follows [37], [41], [42]:

$$\tilde{\gamma} = \frac{\langle s_1 s_2^* \rangle}{\sqrt{\langle |s_1|^2 \rangle \langle |s_2|^2 \rangle}}, \tag{1.3}$$

where $\langle \cdot \rangle$ denotes spatial averaging, and * represents the complex conjugate.

To transform SAR data into coherence-based information products, Figure 1.2 illustrates the TanDEM-X processing chain employed in this thesis. This workflow demonstrates the systematic approach from raw data to final products, highlighting the key processing steps for coherence estimation and parameter retrieval in this thesis.

Of particular interest to this thesis are the coherence losses observed in various environments. Coherence is often reduced in forests due to volume scattering within the canopy. Thus, decorrelation is introduced as the radar signal penetrates and reflects within the vertical structure of the forest. This reduction in coherence carries valuable structural information about the canopy and is directly related to forest height [43], [44]. Similarly, coherence decreases over glaciated and snow-covered regions, where radar signals penetrate into subsurface snow and firn layers [45], [46],

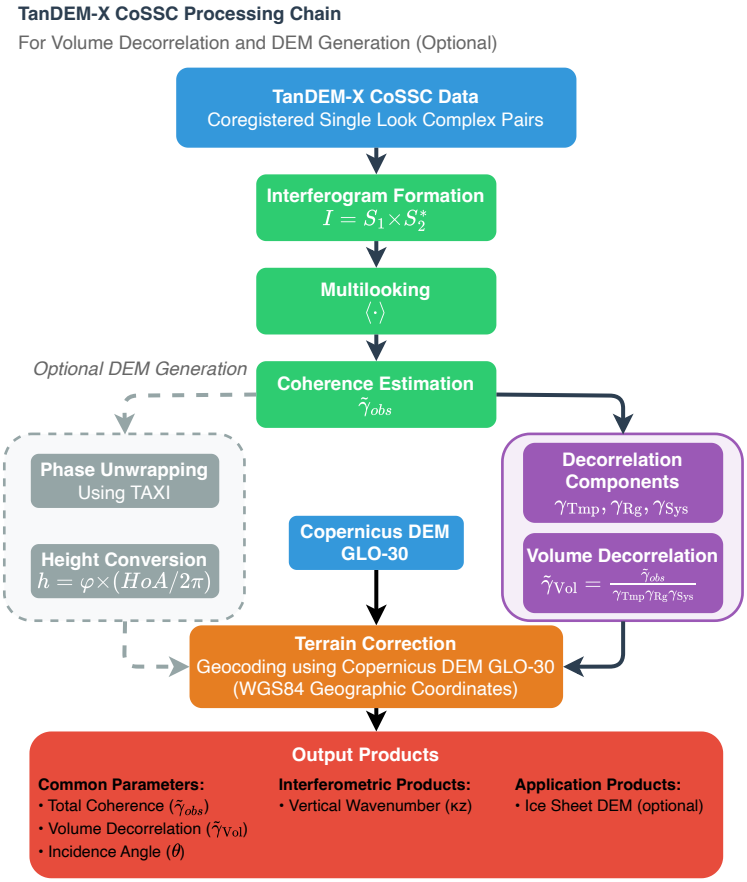

Figure 1.2: TanDEM-X Coherence Processing Chain. The workflow illustrates the systematic processing of TanDEM-X CoSSC (Coregistered Single Look Complex) data pairs, from interferogram formation through coherence estimation to final product generation. Key processing steps include multilooking, coherence estimation, and the separation of different decorrelation components (γ_{Tmp}, γ_{Rg}, γ_{Sys}). The chain produces various output parameters including total coherence ($\tilde{\gamma}_{\mathrm{obs}}$), volume decorrelation ($\tilde{\gamma}_{\mathrm{Vol}}$), and optional DEM products, all geocoded using the Copernicus DEM GLO-30 reference.

[47], [48]. In these cryospheric environments, the vertical distribution of dielectric inhomogeneities—caused by grain size variability, layering, and density gradients—results in phase decorrelation due to multiple scattering events.

To systematically analyze these coherence variations, we must understand their component sources. This understanding leads us to examine the specific decorrelation mechanisms in the following section.

1.2.3.1 *Sources of Decorrelation*

The magnitude of the complex quantity of interferometric coherence, $|\tilde{\gamma}|$, ranges from 0 (no correlation) to 1 (total correlation). A value near total correlation indicates small changes in the underlying scattering geometry, while a value approaching zero implies strong decorrelation—often due to noise, temporal changes, or baseline decorrelation. These variations in coherence contain valuable information about the scattering characteristics of different surfaces, which this thesis exploits for parameter retrieval.

The observed coherence can be decomposed into distinct physical contributions. Several factors contribute to the reduction in measured interferometric coherence, which can be factored as [32], [43], [49], [50]:

$$\tilde{\gamma}_{\text{obs}} = \gamma_{\text{Tmp}} \cdot \gamma_{\text{Rg}} \cdot \gamma_{\text{Sys}} \cdot \tilde{\gamma}_{\text{Vol}}, \tag{1.4}$$

where:

- γ_{Tmp} refers to the temporal decorrelation that is caused by scene changes between acquisitions.
- γ_{Rg} is the range spectral decorrelation caused by baseline-induced spectral separation.
- γ_{Sys} is the system decorrelation resulting from noise and quantization.
- $\tilde{\gamma}_{\text{Vol}}$ represents the volume decorrelation resulting from within-volume scattering.

For the TanDEM-X mission — the primary data source in this thesis — the simultaneous (bistatic) acquisition of images eliminates temporal decorrelation, meaning $\gamma_{\text{Tmp}} \approx 1$. This advantageous characteristic allows us to isolate other sources of decorrelation more effectively.

The system decorrelation term, γ_{Sys}, quantifies coherence loss from instrumental and processing factors. It can be factorized into three major sources: thermal noise, quantization noise, and azimuth ambiguities. These can be expressed as [14], [36], [51], [52]:

$$\gamma_{\text{Sys}} = \gamma_{\text{SNR}} \cdot \gamma_{\text{Quant}} \cdot \gamma_{\text{Amb}}, \tag{1.5}$$

where:

- γ_{SNR} represents the decorrelation caused by thermal noise.
- γ_{Quant} accounts for the quantization noise introduced during analog-to-digital conversion. For 3-bit quantization, it typically takes a value of around 0.98 to 0.99.
- γ_{Amb} represents the coherence loss due to azimuth ambiguities, which arise from Doppler aliasing and the suppression of sidelobes.

This decomposition reveals that even under ideal conditions (i.e., with negligible temporal decorrelation), system-induced factors ($\gamma_{\text{Sys}} < 1$) impose an upper limit on achievable coherence. After accounting for these system and geometry effects, the remaining volume decorrelation term $\tilde{\gamma}_{\text{Vol}}$ in Eq. 1.4 becomes the central focus of this thesis, as it encodes the structural information essential for both forest height estimation and penetration bias correction in ice sheets. This connection between volume decorrelation and physical structure forms the foundation for the hybrid modeling approaches proposed in subsequent chapters.

1.2.3.2 *Volume Decorrelation and Scattering Profile*

With $\tilde{\gamma}_{\text{Vol}}$ identified as the central information carrier in our coherence decomposition, we now turn to the main challenge for

modeling it: how can we relate this measurable quantity to the physical structure of the target medium? This relationship is essential for retrieving parameters such as forest height and penetration depth. The fundamental concept is recognizing that volume decorrelation arises from the three-dimensional distribution of scatterers within the target medium. This distribution can be represented as a vertical scattering profile $f(z)$, which describes how scattering power varies along the vertical axis z. Throughout this thesis, we refer to this function as the "vertical reflectivity profile" when discussing forest applications and as the "vertical scattering profile" when addressing ice and snow media. This terminological distinction is purely conventional.

When radar waves interact with this distributed scattering medium, the resulting volume decorrelation $\tilde{\gamma}_{\text{Vol}}$ encodes information about the vertical structure. Mathematically, this relationship is expressed through a Fourier-like integral transform [42], [44], [53], [54], [55]:

$$\tilde{\gamma}_{\text{Vol}}(\kappa_z) \;=\; e^{j\,\kappa_z\,z_0}\,\frac{\int f(z)\,\exp(j\,\kappa_z\,z)\,dz}{\int f(z)\,dz}, \tag{1.6}$$

where z_0 denotes the ground elevation, and κ_z is the vertical wavenumber, as defined earlier in Eq. 1.4. This equation reveals that volume decorrelation is effectively a normalized complex Fourier transform of the vertical structure function $f(z)$, with the exponential term $e^{j\,\kappa_z\,z_0}$ accounting for the reference phase at z_0.

This formulation creates a crucial bridge between observable radar measurements (coherence) and the physical structure of the medium we wish to characterize. The challenge, however, lies in the inverse problem: given limited observations of $\tilde{\gamma}_{\text{Vol}}$ (typically at a single κ_z value in TanDEM-X data), how can we reconstruct the complete vertical reflectivity profile for forests or the vertical scattering profile for ice? This inverse problem constitutes the core technical challenge addressed in this thesis. For forest environments, we need to determine canopy height and structure; for snow and ice, we must account for signal penetration depth to correct elevation measurements.

The subsequent sections will outline our adaptation of this general framework for specific applications. We will also explain how our hybrid approach combines physical constraints with machine learning techniques to effectively address the limitations inherent in traditional inversion methods.

1.2.4 *Forest Volume Decorrelation*

For forest environments, we adapt the general volume decorrelation equation (Eq. 1.6) to incorporate specific boundary conditions, where scattering occurs within the finite canopy layer [37], [41], [42]:

$$\tilde{\gamma}_{\text{Vol}}(\kappa_z) \;=\; e^{j\,\kappa_z\,z_0}\,\frac{\int_0^{h_v} f(z)\,\exp(j\,\kappa_z\,z)\,\mathrm{d}z}{\int_0^{h_v} f(z)\,\mathrm{d}z}, \tag{1.7}$$

where z_0 is the reference ground level, κ_z is the vertical wavenumber, h_v is the forest height, and $f(z)$ represents the vertical reflectivity profile.

A significant challenge in forest height retrieval from single-baseline InSAR (e.g., TanDEM-X) is the fundamental ill-posedness of reconstructing $f(z)$ from limited observations [6], [19], [21], [38], [54], [56], [57]. The physical reality further complicates this task, as forest canopies exhibit complex vertical structures and varying terrain, both of which affect the scattering profile. Figure 1.3 illustrates this reality, showing how the canopy extends from ground level (z_0) to the top ($z_0 + h_v$).

Earlier approaches, such as the Random Volume (RV), Random Volume over Ground (RVoG), and S-RVoG (with slope) models, made simplifying assumptions about $f(z)$ to facilitate parameter retrieval; however, these assumptions restrict their generalizability across diverse forest ecosystems [17], [53], [54], [55], [58], [59], [60], [61]. Recent advances have explored integrating additional data sources, such as GEDI LiDAR profiles, to better constrain and derive the vertical reflectivity profile [6], [21].

Our approach builds upon these foundations while introducing a hybrid modeling framework. We represent $f(z)$ using a Legendre series expansion, the coefficients of which are estimated through ML. This ML component maps observables (e.g., volume coher-

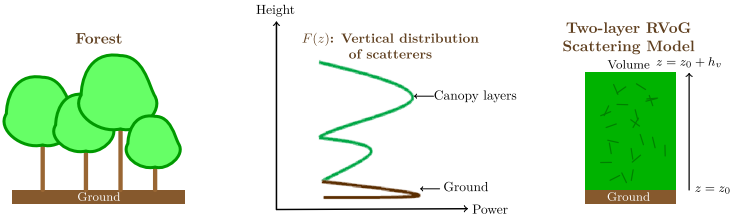

Figure 1.3: Schematic illustration of (left) a forest canopy, (middle) the vertical scattering profile $f(z)$ showing the distribution of scatterers from ground to canopy top, and (right) a simplified two-layer RVoG model. The canopy volume extends from $z = z_0$ to $z = z_0 + h_v$.

ence, acquisition geometry) to expansion coefficients while being constrained by the physics in Eq. 1.7. We detail this methodology in Chapter 2, which demonstrates its application to forest height estimation in Gabon, and we extend it in Chapter 3 by integrating multi-spectral imagery to further refine $f(z)$.

1.2.5 *Snow/Ice Volume Decorrelation*

While forests present a bounded scattering volume above the ground, snow and ice environments introduce a different challenge: radar signal penetration into subsurface layers. This penetration creates a downward-extending scattering volume that shifts the effective phase center below the surface—a phenomenon known as penetration bias, which systematically affects InSAR-derived elevation measurements.

For these media, we adapt the volume decorrelation model (Eq. 1.6) as [62], [63], [64]:

$$\tilde{\gamma}_{\text{Vol}}(\kappa_z) \;=\; e^{j\,\kappa_z\, z_0}\,\frac{\displaystyle\int_{-\infty}^{0} f(z)\,\exp(j\,\kappa_{z_{\text{Vol}}}\, z)\,\mathrm{d}z}{\displaystyle\int_{-\infty}^{0} f(z)\,\mathrm{d}z}, \tag{1.8}$$

where z_0 is the air–snow or air–ice interface, $f(z)$ is the vertical scattering profile extending downward from this interface, and notably, $\kappa_{z_{\text{Vol}}}$ is the in-volume vertical wavenumber that accounts for refraction effects.

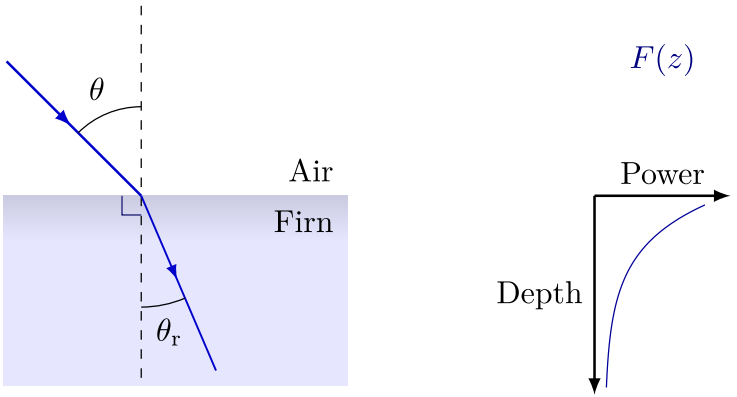

Figure 1.4: Schematic representation of radar penetration into snow and ice, showing (left) the interferometric geometry at the air–firn interface with incident angle θ and refracted angle θ_r, and (right) exponential scattering profile for the UV physical model assumptions.

A critical physical consideration in snow/ice penetration is the refraction effect at the air-medium interface. As shown in Figure 1.4, when radar signals encounter the air-snow/ice boundary, the incident wave at angle θ refracts to angle θ_r according to Snell's law. This refraction modifies the in-volume vertical wavenumber $\kappa_{z_{Vol}}$ according to [64]:

$$\kappa_{z_{Vol}} = \kappa_z \sqrt{\epsilon_r} \frac{\cos(\theta)}{\cos(\theta_r)} \tag{1.9}$$

where ϵ_r is the real part of the relative permittivity of the snow/ice medium. The refraction angle θ_r can be determined from Snell's law as $\theta_r = \arcsin(\sin\theta/\sqrt{\epsilon_r})$. This relationship captures how the propagation of electromagnetic waves changes upon entering the medium—the higher permittivity of snow and ice (typically $\epsilon_r' \approx 1.4$–3.2 depending mainly on density) causes the wave to bend more toward the vertical and alters the effective vertical wavenumber [8], [64], [65], [66]. This refraction effect must be carefully accounted for when modeling volume decorrelation and estimating penetration bias. However, TanDEM-X DEMs are produced

under the *free-space* assumption; thus, the penetration bias correction must also adopt the *free-space* vertical wavenumber κ_z.

Unlike forest scenarios with a bounded vertical extent, snow and ice can exhibit scattering that extends much deeper, depending on medium properties such as density, grain size, and liquid water content [7], [67]. Traditional approaches, such as the Uniform Volume (UV) model, assume constant extinction with depth, yielding an exponential scattering profile [63], [64]. However, this simplified model often fails to capture the complexity of real-world snow and ice structures, leading to inaccurate estimates of penetration bias.

More recent developments have introduced the Weibull scattering profile [9], which offers greater flexibility in representing varying extinction rates with depth. While potentially more realistic, this model is not invertible from single-polarization, single-baseline coherence at the pixel level. In contrast, this capability is achievable through the closed-form solution of the UV model.

In Chapter 4, we extend our hybrid modeling framework to this challenging environment, demonstrating how it can effectively estimate penetration bias in Greenland ice sheets by learning the parameterization of vertical scattering profiles from limited observations while adhering to physical constraints.

1.2.6 *Hybrid Modeling: Broader Research Applications*

Recent advancements in ML have demonstrated substantial potential in various applications, including medical applications, natural language processing, complex pattern recognition, image analysis, and remote sensing [68], [69], [70], [71], [72], [73]. Formally, ML can be framed as the task of learning a mapping function:

$$f : \mathcal{X} \rightarrow \mathcal{Y}, \tag{1.10}$$

which, for input variables $\mathbf{x} \in \mathcal{X}$, predicts target variables $y \in \mathcal{Y}$ by minimizing a suitable loss function over the training data. One example is the Multi-Layer Perceptron (MLP), a feed-forward neural network with an input layer, one or more hidden layers, and an output layer, as illustrated in Figure 1.5. Although ML initially seemed to directly compete with traditional fundamental modeling

research, there is a growing recognition of the synergies between ML and physical modeling. Integrating data-driven and physics-based approaches has shown added benefits and expanded capabilities across various scientific and engineering applications [74], [75], [76], [77], [78], [79], [80], [81].

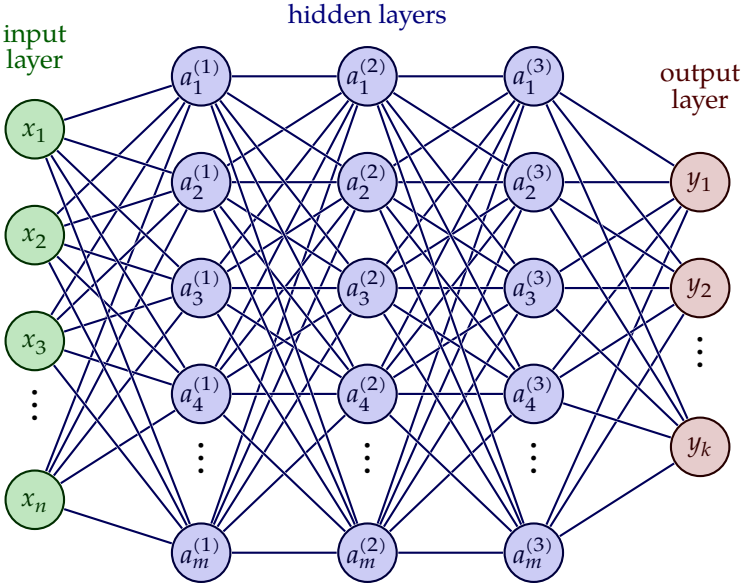

Figure 1.5: A schematic representation of a MLP architecture, showing an input layer $\{x_1, x_2, \ldots, x_n\}$, multiple hidden layers $\{a_m^{(l)}\}$, and an output layer $\{y_1, y_2, \ldots, y_k\}$. Each connection is associated with learnable weights and, typically, a bias term.

Hybrid modeling — often referred to as hybrid semi-parametric modeling — combines physical models grounded in first principles with data-driven approaches, such as ML, to exploit the strengths of both paradigms. This concept originated in the early 1990s [82], [83], [84], [85], [86], [87], when researchers demonstrated that integrating fundamental knowledge into neural networks could enhance extrapolation performance, reduce data requirements, and improve model interpretability. Hybrid modeling explicitly refers to systems in which a parametric component—derived from physical principles with interpretable parameters—combines with

a non-parametric component that captures complex, data-driven behavior. Recent studies have further validated these benefits by embedding physical constraints within ML frameworks [88], [89], [90]

In the context of geo- and biophysical parameter retrieval from InSAR data, traditional model-based approaches often rely on simplifying assumptions to represent complex scattering processes. Such simplifications can lead to systematic errors, including underestimations of forest heights in regions such as Gabon and penetration biases in snow-covered areas like Greenland. By integrating machine learning with physical models, the thesis proposes to adapt a hybrid framework to enhance parameter retrieval using InSAR data.

1.3 RESEARCH OBJECTIVES

The increasing complexity of Earth observation data and the limitations of traditional physical models highlight the urgent need for more sophisticated parameter retrieval methods. This is particularly pronounced in InSAR applications, where simplified physical models often struggle to capture complex scattering processes in forests and ice sheets, leading to systematic errors in parameter estimation. These challenges underscore the need for approaches that can maintain physical consistency while adapting to the complexities of the real-world.

This thesis aims to advance the integration of machine learning with physical models in InSAR parameter retrieval, termed hybrid modeling. The research comprises three self-contained contributions that address the challenges of combining data-driven and physics-based approaches. Each contribution develops innovative methodologies for parameter retrieval from InSAR data, accompanied by comprehensive validation that demonstrates the advantages of hybrid modeling frameworks.

The following section outlines the specific research objectives and questions addressed in each of these three contributions.

1.3.1 *Hybrid ML Forest Height Estimation From TanDEM-X InSAR*

This study presents an innovative approach to enhancing forest height estimation from single-baseline TanDEM-X data. Traditional model-based approaches rely on simplified assumptions about vertical reflectivity profiles, which often lead to systematic errors in height estimation, particularly in areas with complex forest structures. Additionally, the limited observation space of single-baseline acquisitions poses significant challenges for reliable parameter retrieval. These limitations highlight the need for more robust and adaptive methods that can maintain physical consistency while capturing complex forest characteristics.

To address these challenges, this research aims to develop a hybrid framework that combines the flexibility of machine learning with the constraints of physical models. Building on the concept of vertical reflectivity profiles, a novel approach using multilayer perceptron networks is introduced to predict profile coefficients that drive a physical inversion model. This method enables a more accurate estimation of forest height while preserving the interpretability of physical models.

The investigation is guided by three key research questions:

1. How can machine learning be effectively integrated with physical models to improve forest height estimation from single-baseline InSAR data?
2. What improvements in accuracy and generalization can be achieved through hybrid modeling compared to traditional approaches?
3. How does the framework perform across different forest types and terrain conditions?

1.3.2 *Hybrid Forest Height Estimation from TanDEM-X and Landsat Data*

The retrieval of forest parameters from InSAR data often encounters challenges in capturing subtle variations in forest structure that impact height estimation. While existing InSAR-based techniques have proven effective in many scenarios, their performance can be limited by the single-modality nature of the observations. These

challenges make it difficult to achieve reliable and accurate results using conventional methods, particularly in areas with complex terrain or varying forest density.

To address these limitations and enhance parameter retrieval accuracy, this study proposes an extended hybrid framework that integrates multi-spectral optical data with InSAR measurements. By leveraging complementary information from different sensor modalities, the framework aims to improve forest height estimation while maintaining physical consistency in the inversion process. The research focuses on developing solutions for physically consistent multi-modal data fusion.

The study is structured around three key research questions:

1. How can optical multi-spectral data be effectively integrated into the hybrid modeling framework while maintaining physical consistency?

2. What improvements in forest height estimation accuracy can be achieved through multi-modal data fusion?

3. How does the multi-modal framework perform under different acquisition geometries and terrain conditions?

1.3.3 *Hybrid AI–Physical Modeling for X-band InSAR DEMs: Greenland*

Accurate elevation measurements over ice sheets are crucial for monitoring climate change impacts and understanding cryospheric processes. However, X-band InSAR measurements over snow and ice are affected by signal penetration, which introduces systematic biases in the derived digital elevation models. This penetration bias varies with snow and ice conditions, making it challenging to correct using conventional physical models alone. These challenges highlight the need for more sophisticated approaches that can adapt to varying surface conditions while maintaining physical consistency.

To address this, the study focuses on developing a hybrid framework for penetration bias correction in X-band InSAR DEMs over the Greenland Ice Sheet. The framework combines parametric physical models with machine learning components to achieve more accurate and robust bias estimation. This approach enables

adaptive bias correction while preserving the interpretability of physical scattering models.

The study seeks to address the following three key research questions:

1. How can hybrid modeling effectively address penetration bias in X-band InSAR DEMs over ice sheets?
2. What advantages does the hybrid approach offer over purely physical or purely ML methods?
3. How well does the framework generalize across different acquisition geometries and surface conditions?

1.4 THESIS ORGANIZATION

The remainder of the thesis is structured according to the research objectives stated in section 1.3, which focus on the development and validation of the hybrid modeling framework. The thesis is organized as follows:

- **Chapter 2 (Hybrid Modeling for Forest Height Estimation):** In this chapter, the proposed framework's first application, forest height estimation, is presented. A detailed methodology is introduced to address the first objective. This is achieved by reconstructing the vertical scattering profile using a series expansion, Legendre polynomials, which derive coefficients using an MLP, taking InSAR features as inputs. Then, the reconstructed profile simulates the coherence for a given forest height, derived from LiDAR, to train the MLP model. The chapter discusses the limitations of model-based and data-driven approaches and how we address them in the hybrid-based approach while enforcing physical constraints. The experimental results from three sites in Gabon are provided to assess the method's performance, robustness, and generalizability.
- **Chapter 3 (multi-modal Data Integration for Forest Parameter Retrieval):** This chapter extends the hybrid framework by incorporating auxiliary data—specifically, optical multispectral imagery from Landsat—as an additional input to

the ML components to improve forest height retrieval. To address the second objective, it outlines the integration strategy within the inversion process and evaluates the resulting improvements in retrieval accuracy under challenging terrain and acquisition conditions.

- **Chapter 4 (Hybrid Modeling for Penetration Bias Correction in X-band InSAR DEMs):** Focusing on snow- and ice-covered regions in Greenland, this chapter adapts the hybrid framework to address the penetration biases inherent in X-band InSAR measurements concerning the third objective. The methodology for estimating the scattering profile is detailed, and a comparative study is presented in which pure physical, data-driven, and hybrid methods are evaluated under different training scenarios to demonstrate generalizability and performance.

- **Chapter 5 (Conclusions):** The final chapter summarizes the main outcomes of the research, reflecting on the contributions and limitations of the developed hybrid modeling approaches. It also discusses the potential implications for future remote sensing applications and outlines directions for further research, including extensions to additional geophysical and biophysical parameter retrieval problems.

REFERENCES

[1] A. Belward, M. Bourassa, M. Dowell, s. briggs, H. (Dolman, K. Holmlund, R. Husband, S. Quegan, A. Simmons, B. Sloyan, D. Stammer, K. Steffen, T. Tanhua, M. Verstraete, C. Richter, S. Eggleston, K. Hill, C. Tassone, B. Mora, and S. Saatchi, *The Global Observing System for Climate: Implementation Needs*. 2016 (cited on pages 3, 5).

[2] T. Le Toan, S. Quegan, M. W. J. Davidson, H. Balzter, P. Paillou, K. Papathanassiou, S. Plummer, F. Rocca, S. Saatchi, H. Shugart, and L. Ulander, "The BIOMASS Mission: Mapping Global Forest Biomass to Better Understand the Terrestrial Carbon Cycle," *Remote Sensing of Environment*, DESDynI VEG-3D Special Issue, vol. 115, no. 11, 2850, 2011. DOI: 10.1016/j.rse.2011.03.020 (cited on pages 3, 4).

[3] C. Kuenzer, A. Bluemel, S. Gebhardt, V. Q. Tuan, and S. Dech, "Remote Sensing of Mangrove Ecosystems: A Review," *REMOTE SENSING*, vol. 3, no. 5, 878, 2011. DOI: 10.3390/rs3050878 (cited on pages 3, 4).

[4] J. Mingle, "IPCC Special Report on the Ocean and Cryosphere in a Changing Climate," *NEW YORK REVIEW OF BOOKS*, vol. 67, no. 8, 49, 2020 (cited on pages 3–5).

[5] J. Gao, "Bathymetric Mapping by Means of Remote Sensing: Methods, Accuracy and Limitations," *PROGRESS IN PHYSICAL GEOGRAPHY-EARTH AND ENVIRONMENT*, vol. 33, no. 1, 103, 2009. DOI: 10.1177/0309133309105657 (cited on page 3).

[6] C. Choi, V. Cazcarra-Bes, R. Guliaev, M. Pardini, K. P. Papathanassiou, W. Qi, J. Armston, and R. O. Dubayah, "Large-Scale Forest Height Mapping by Combining TanDEM-X and GEDI Data," *IEEE Journal of Selected Topics in Applied Earth Observations and Remote Sensing*, vol. 16, 2374, 2023. DOI: 10.1109/JSTARS.2023.3244866 (cited on pages 4, 6, 16).

[7] S. Abdullahi, B. Wessel, M. Huber, A. Wendleder, A. Roth, and C. Kuenzer, "Estimating Penetration-Related X-Band InSAR Elevation Bias: A Study over the Greenland Ice Sheet," *Remote Sensing*, vol. 11, no. 24, 2903, 2019. DOI: 10.3390/rs11242903 (cited on pages 4, 6, 7, 19).

[8] G. Fischer, M. Jäger, K. P. Papathanassiou, and I. Hajnsek, "Modeling the Vertical Backscattering Distribution in the Percolation Zone of the Greenland Ice Sheet With SAR Tomography," *IEEE Journal of Selected Topics in Applied Earth Observations and Remote Sensing*, vol. 12, no. 11, 4389, 2019. DOI: 10.1109/JSTARS.2019.2951026 (cited on pages 4, 6, 18).

[9] G. Fischer, K. P. Papathanassiou, and I. Hajnsek, "Modeling and Compensation of the Penetration Bias in InSAR DEMs of Ice Sheets at Different Frequencies," *IEEE Journal of Selected Topics in Applied Earth Observations and Remote Sensing*, vol. 13, 2698, 2020. DOI: 10.1109/JSTARS.2020.2992530 (cited on pages 4, 6, 19).

[10] H. Rott, S. Scheiblauer, J. Wuite, L. Krieger, D. Floricioiu, P. Rizzoli, L. Libert, and T. Nagler, "Penetration of interferometric radar signals in Antarctic snow," *The Cryosphere*, vol. 15, no. 9, 4399, 2021. DOI: 10.5194/tc-15-4399-2021 (cited on pages 4, 6).

[11] A. Moreira, P. Prats-Iraola, M. Younis, G. Krieger, I. Hajnsek, and K. P. Papathanassiou, "A tutorial on synthetic aperture radar," *IEEE Geoscience and Remote Sensing Magazine*, vol. 1, no. 1, 6, 2013. DOI: 10/gfj2jw (cited on pages 5, 8).

[12] B. Rabus, M. Eineder, A. Roth, and R. Bamler, "The Shuttle Radar Topography Mission—a New Class of Digital Elevation Models Acquired by Spaceborne Radar," *ISPRS Journal of Photogrammetry and Remote Sensing*, vol. 57, no. 4, 241, 2003. DOI: 10.1016/S0924-2716(02)00124-7 (cited on page 5).

[13] I. Hajnsek, T. Busche, S. Abdullahi, M. Bachmann, S. V. Baumgartner, A. Bojarski, J.-L. Bueso-Bello, T. Esch, T. Fritz, A. Alonso-Gonzalez, C. Gonzalez, L. Huang, T. Kraus, M. Lachaise, S. Li, F. L. Dekker, K. Maier, M. Martone, P. Milillo, J. Mittermayer, M. Nannini, K. Papathanassiou, M. Pardini, M. Pinheiro, P. Prats-Iraola, P. Rizzoli, M. Rodriguez-Cassola, A. Roth, M. Schandri, R. Scheiber, U. Steinbrecher,

B. Schweisshelm, M. Villano, L. J. Warmedinger, B. Wessel, G. Krieger, M. Zink, and A. Moreira, "TanDEM-X: The 4D Mission Phase for Earth Surface Dynamics: Science Activities Highlights and New Data Products after 15 Years of Bistatic Operations," *IEEE Geoscience and Remote Sensing Magazine*, 2, 2025. DOI: 10.1109/MGRS.2024.3525403 (cited on pages 5, 10).

[14] G. Krieger, A. Moreira, H. Fiedler, I. Hajnsek, M. Werner, M. Younis, and M. Zink, "TanDEM-X: A Satellite Formation for High-Resolution SAR Interferometry," *IEEE Transactions on Geoscience and Remote Sensing*, vol. 45, no. 11, 3317, 2007. DOI: 10.1109/TGRS.2007.900693 (cited on pages 5, 9, 10, 14).

[15] P. Rizzoli, M. Martone, C. Gonzalez, C. Wecklich, D. Borla Tridon, B. Bräutigam, M. Bachmann, D. Schulze, T. Fritz, M. Huber, B. Wessel, G. Krieger, M. Zink, and A. Moreira, "Generation and Performance Assessment of the Global TanDEM-X Digital Elevation Model," *ISPRS Journal of Photogrammetry and Remote Sensing*, vol. 132, 119, 2017. DOI: 10.1016/j.isprsjprs.2017.08.008 (cited on page 5).

[16] W. Qi, J. Armston, C. Choi, A. Stovall, S. Saarela, M. Pardini, L. Fatoyinbo, K. Papathanassiou, A. Pascual, and R. Dubayah, "Mapping Large-Scale Pantropical Forest Canopy Height by Integrating GEDI Lidar and TanDEM-X InSAR Data," *Remote Sensing of Environment*, vol. 318, 114534, 2025. DOI: 10.1016/j.rse.2024.114534 (cited on page 6).

[17] I. Hajnsek, F. Kugler, S.-K. Lee, and K. P. Papathanassiou, "Tropical-Forest-Parameter Estimation by Means of Pol-InSAR: The INDREX-II Campaign," *IEEE Transactions on Geoscience and Remote Sensing*, vol. 47, no. 2, 481, 2009. DOI: 10.1109/TGRS.2008.2009437 (cited on pages 6, 16).

[18] R. N. Treuhaft, B. D. Chapman, J. R. Dos Santos, F. G. Gonçalves, L. V. Dutra, P. M. L. A. Graça, and J. B. Drake, "Vegetation profiles in tropical forests from multibaseline interferometric synthetic aperture radar, field, and lidar measurements," *Journal of Geophysical Research*, vol. 114, D23110, D23 2009. DOI: 10.1029/2008JD011674 (cited on page 6).

[19] F. Kugler, Seung-Kuk Lee, I. Hajnsek, and K. P. Papathanassiou, "Forest Height Estimation by Means of Pol-InSAR Data Inversion: The Role of the Vertical Wavenumber," *IEEE Transactions on Geoscience and Remote Sensing*, vol. 53, no. 10, 5294, 2015. DOI: 10.1109/TGRS.2015.2420996 (cited on pages 6, 16).

[20] W. Qi, S. Saarela, J. Armston, G. Ståhl, and R. Dubayah, "Forest Biomass Estimation over Three Distinct Forest Types Using TanDEM-X InSAR Data and Simulated GEDI Lidar Data," *Remote Sensing of Environment*, vol. 232, 2019. DOI: 10.1016/J.RSE.2019.111283 (cited on page 6).

[21] R. Guliaev, V. Cazcarra-Bes, M. Pardini, and K. Papathanassiou, "Forest Height Estimation by Means of TanDEM-X InSAR and Waveform Lidar Data," *IEEE Journal of Selected Topics in Applied Earth Observations and Remote Sensing*, vol. 14, 3084, 2021. DOI: 10.1109/JSTARS.2021.3058837 (cited on pages 6, 16).

[22] D. Carcereri, P. Rizzoli, D. Ienco, and L. Bruzzone, "A Deep Learning Framework for the Estimation of Forest Height From Bistatic TanDEM-X Data," *IEEE Journal of Selected Topics in Applied Earth Observations and Remote Sensing*, vol. 16, 8334, 2023. DOI: 10.1109/JSTARS.2023.3310209 (cited on page 6).

[23] J.-L. Bueso-Bello, D. Carcereri, M. Martone, C. González, P. Posovszky, and P. Rizzoli, "Deep Learning for Mapping Tropical Forests with TanDEM-X Bistatic InSAR Data," *Remote Sensing*, vol. 14, no. 16, 3981, 2022. DOI: 10.3390/rs14163981 (cited on page 6).

[24] J. Bao, N. Zhu, R. Chen, B. Cui, W. Li, and B. Yang, "Estimation of Forest Height Using Google Earth Engine Machine Learning Combined with Single-Baseline TerraSAR-X/TanDEM-X and LiDAR," *Forests*, vol. 14, no. 10, 1953, 2023. DOI: 10.3390/f14101953 (cited on page 6).

[25] C. Mätzler, "Applications of the interaction of microwaves with the natural snow cover," *Remote Sensing Reviews*, vol. 2, no. 2, 259, 1987. DOI: 10.1080/02757258709532086 (cited on page 7).

[26] A. B. Campos, M. Braun, and P. Rizzoli, "On the Potential of Bistatic Insar Features for Monitoring Ice Sheets Properties and Estimating Surface Elevation Bias," in *IGARSS 2024 - 2024 IEEE International Geoscience and Remote Sensing Symposium*, Athens, Greece: IEEE, 2024, 143. DOI: 10.1109/IGARSS53475.2024.10640443 (cited on page 7).

[27] J. C. Curlander and R. N. McDonough, *Synthetic Aperture Radar: Systems and Signal Processing* (Wiley Series in Remote Sensing and Image Processing). John Wiley & Sons, 1991 (cited on page 8).

[28] I. H. Woodhouse, *Introduction to Microwave Remote Sensing*. CRC Press, 2017. DOI: 10.1201/9781315272573 (cited on page 8).

[29] I. G. Cumming and F. H.-c. Wong, *Digital Processing of Synthetic Aperture Radar Data: Algorithms and Implementation*. Artech House, 2005, 625 pp. (cited on page 9).

[30] J. A. Richards, *Remote Sensing with Imaging Radar*. Springer Science & Business Media, 2009, 376 pp. (cited on page 9).

[31] R. Torres, P. Snoeij, D. Geudtner, D. Bibby, M. Davidson, E. Attema, P. Potin, B. Rommen, N. Floury, M. Brown, I. N. Traver, P. Deghaye, B. Duesmann, B. Rosich, N. Miranda, C. Bruno, M. L'Abbate, R. Croci, A. Pietropaolo, M. Huchler, and F. Rostan, "GMES Sentinel-1 Mission," *Remote Sensing of Environment*, The Sentinel Missions - New Opportunities for Science, vol. 120, 9, 2012. DOI: 10.1016/j.rse.2011.05.028 (cited on page 9).

[32] R. Bamler and P. Hartl, "Synthetic aperture radar interferometry," *Inverse Problems*, vol. 14, no. 4, R1, 1998. DOI: 10.1088/0266-5611/14/4/001 (cited on pages 9, 10, 13).

[33] S. Cloude and E. Pottier, "A Review of Target Decomposition Theorems in Radar Polarimetry," *IEEE Transactions on Geoscience and Remote Sensing*, vol. 34, no. 2, 498, 1996. DOI: 10.1109/36.485127 (cited on page 9).

[34] I. Hajnsek and Y.-L. Desnos, Eds., *Polarimetric Synthetic Aperture Radar: Principles and Application* (Remote Sensing and Digital Image Processing). Cham: Springer International Publishing, 2021, vol. 25. DOI: 10.1007/978-3-030-56504-6 (cited on page 9).

[35] L. Graham, "Synthetic Interferometer Radar for Topographic Mapping," *Proceedings of the IEEE*, vol. 62, no. 6, 763, 1974. DOI: 10.1109/PROC.1974.9516 (cited on page 10).

[36] F. Gatelli, A. Monti Guamieri, F. Parizzi, P. Pasquali, C. Prati, and F. Rocca, "The wavenumber shift in SAR interferometry," *IEEE Transactions on Geoscience and Remote Sensing*, vol. 32, no. 4, 855, 1994. DOI: 10.1109/36.298013 (cited on pages 10, 14).

[37] S. Cloude, *Polarisation: Applications in Remote Sensing*. Oxford University Press, 2009. DOI: 10.1093/acprof:oso/9780199569731.001.0001 (cited on pages 10, 11, 16).

[38] G. Krieger, M. Zink, M. Bachmann, B. Bräutigam, D. Schulze, M. Martone, P. Rizzoli, U. Steinbrecher, J. Walter Antony, F. De Zan, I. Hajnsek, K. Papathanassiou, F. Kugler, M. Rodriguez Cassola, M. Younis, S. Baumgartner, P. López-Dekker, P. Prats, and A. Moreira, "TanDEM-X: A radar interferometer with two formation-flying satellites," *Acta Astronautica*, vol. 89, 83, 2013. DOI: 10.1016/j.actaastro.2013.03.008 (cited on pages 10, 16).

[39] G. Krieger, K. P. Papathanassiou, and S. R. Cloude, "Spaceborne polarimetric SAR interferometry: Performance analysis and mission concepts," *Eurasip Journal on Applied Signal Processing*, vol. 2005, no. 20, 3272, 2005. DOI: 10/ft5mp5 (cited on page 10).

[40] R. F. Hanssen, *Radar Interferometry: Data Interpretation and Error Analysis* (Remote Sensing and Digital Image Processing), F. Van Der Meer, red. Dordrecht: Springer Netherlands, 2001, vol. 2. DOI: 10.1007/0-306-47633-9 (cited on page 10).

[41] P. Rosen, S. Hensley, I. Joughin, F. Li, S. Madsen, E. Rodriguez, and R. Goldstein, "Synthetic aperture radar interferometry," *Proceedings of the IEEE*, vol. 88, no. 3, 333, 2000. DOI: 10.1109/5.838084 (cited on pages 10, 11, 16).

[42] S. Cloude and K. Papathanassiou, "Polarimetric SAR interferometry," *IEEE Transactions on Geoscience and Remote Sensing*, vol. 36, no. 5, 1551, 1998. DOI: 10.1109/36.718859 (cited on pages 11, 15, 16).

[43] J. O. Hagberg, L. M. Ulander, and J. Askne, "Repeat-pass SAR interferometry over forested terrain," *IEEE Transactions on Geoscience and Remote Sensing*, vol. 33, no. 2, 331, 1995. DOI: 10.1109/TGRS.1995.8746014 (cited on pages 11, 13).

[44] R. N. Treuhaft, S. N. Madsen, M. Moghaddam, and J. J. van Zyl, "Vegetation characteristics and underlying topography from interferometric radar," *Radio Science*, vol. 31, no. 6, 1449, 1996. DOI: 10.1029/96RS01763 (cited on pages 11, 15).

[45] H. A. Zebker and R. M. Goldstein, "Topographic mapping from interferometric synthetic aperture radar observations," *Journal of Geophysical Research: Solid Earth*, vol. 91, 4993, B5 1986. DOI: 10.1029/JB091iB05p04993 (cited on page 11).

[46] I. Joughin, D. Winebrenner, M. Fahnestock, R. Kwok, and W. Krabill, "Measurement of ice-sheet topography using satellite-radar interferometry," *Journal of Glaciology*, vol. 42, no. 140, 10, 1996. DOI: 10.3189/S0022143000030483 (cited on page 11).

[47] E. Weber Hoen and H. Zebker, "Penetration depths inferred from interferometric volume decorrelation observed over the Greenland Ice Sheet," *IEEE Transactions on Geoscience and Remote Sensing*, vol. 38, no. 6, 2571, 2000. DOI: 10.1109/36.885204 (cited on page 13).

[48] E. Rignot, K. Echelmeyer, and W. Krabill, "Penetration depth of interferometric synthetic-aperture radar signals in snow and ice," *Geophysical Research Letters*, vol. 28, no. 18, 3501, 2001. DOI: 10.1029/2000GL012484 (cited on page 13).

[49] J. Askne, P. Dammert, L. Ulander, and G. Smith, "C-band repeat-pass interferometric SAR observations of the forest," *IEEE Transactions on Geoscience and Remote Sensing*, vol. 35, no. 1, 25, 1997. DOI: 10.1109/36.551931 (cited on page 13).

[50] H. Zebker and J. Villasenor, "Decorrelation in interferometric radar echoes," *IEEE Transactions on Geoscience and Remote Sensing*, vol. 30, no. 5, 950, 1992. DOI: 10.1109/36.175330 (cited on page 13).

[51] M. Martone, B. Bräutigam, P. Rizzoli, C. Gonzalez, M. Bachmann, and G. Krieger, "Coherence evaluation of TanDEM-X interferometric data," *ISPRS Journal of Photogrammetry and Remote Sensing*, Innovative Applications of SAR Interferometry from modern Satellite Sensors, vol. 73, 21, 2012. DOI: 10.1016/j.isprsjprs.2012.06.006 (cited on page 14).

[52] M. Martone, B. Bräutigam, and G. Krieger, "Quantization Effects in TanDEM-X Data," *IEEE Transactions on Geoscience and Remote Sensing*, vol. 53, no. 2, 583, 2015. DOI: 10.1109/TGRS.2014.2325976 (cited on page 14).

[53] R. N. Treuhaft and P. R. Siqueira, "Vertical structure of vegetated land surfaces from interferometric and polarimetric radar," *Radio Science*, vol. 35, no. 1, 141, 2000. DOI: 10.1029/1999RS900108 (cited on pages 15, 16).

[54] K. Papathanassiou and S. Cloude, "Single-baseline polarimetric SAR interferometry," *IEEE Transactions on Geoscience and Remote Sensing*, vol. 39, no. 11, 2352, 2001. DOI: 10.1109/36.964971 (cited on pages 15, 16).

[55] S. Cloude and K. Papathanassiou, "Three-stage inversion process for polarimetric SAR interferometry," *IEE Proceedings - Radar, Sonar and Navigation*, vol. 150, no. 3, 125, 2003. DOI: 10/b59cx5 (cited on pages 15, 16).

[56] F. Kugler, D. Schulze, I. Hajnsek, H. Pretzsch, and K. P. Papathanassiou, "TanDEM-X Pol-InSAR Performance for Forest Height Estimation," *IEEE Transactions on Geoscience and Remote Sensing*, vol. 52, no. 10, 6404, 2014. DOI: 10.1109/TGRS.2013.2296533 (cited on page 16).

[57] R. Treuhaft, F. Gonzalves, J. R. Dos Santos, M. Keller, M. Palace, S. N. Madsen, F. Sullivan, and P. M. L. A. Graca, "Tropical-Forest Biomass Estimation at X-Band From the Spaceborne TanDEM-X Interferometer," *IEEE Geoscience and Remote Sensing Letters*, vol. 12, no. 2, 239, 2015. DOI: 10.1109/LGRS.2014.2334140 (cited on page 16).

[58] R. N. Treuhaft, S. N. Madsen, M. Moghaddam, and J. J. van Zyl, "Vegetation Characteristics and Underlying Topography from Interferometric Radar," *Radio Science*, vol. 31, no. 6, 1449, 1996. DOI: 10.1029/96RS01763 (cited on page 16).

[59] C. López-Martínez and A. Alonso-González, "Assessment and Estimation of the RVoG Model in Polarimetric SAR Interferometry," *IEEE Transactions on Geoscience and Remote Sensing*, vol. 52, no. 6, 3091, 2014. DOI: 10.1109/TGRS.2013.2269614 (cited on page 16).

[60] F. Garestier, P. C. Dubois-Fernandez, and K. P. Papathanassiou, "Pine Forest Height Inversion Using Single-Pass X-Band PolInSAR Data," *IEEE Transactions on Geoscience and Remote Sensing*, vol. 46, no. 1, 59, 2008. DOI: 10.1109/TGRS.2007.907602 (cited on page 16).

[61] H. Lu, Z. Suo, R. Guo, and Z. Bao, "S-RVoG model for forest parameters inversion over underlying topography," *Electronics Letters*, vol. 49, no. 9, 618, 2013. DOI: 10.1049/el.2012.4467 (cited on page 16).

[62] J. Dall, S. N. Madsen, K. Keller, and R. Forsberg, "Topography and penetration of the Greenland Ice Sheet measured with Airborne SAR Interferometry," *Geophysical Research Letters*, vol. 28, no. 9, 1703, 2001. DOI: 10.1029/2000GL011787 (cited on page 17).

[63] J. Dall, "InSAR Elevation Bias Caused by Penetration Into Uniform Volumes," *IEEE Transactions on Geoscience and Remote Sensing*, vol. 45, no. 7, 2319, 2007. DOI: 10.1109/TGRS.2007.896613 (cited on pages 17, 19).

[64] J. J. Sharma, I. Hajnsek, K. P. Papathanassiou, and A. Moreira, "Estimation of Glacier Ice Extinction Using Long-Wavelength Airborne Pol-InSAR," *IEEE Transactions on Geoscience and Remote Sensing*, vol. 51, no. 6, 3715, 2013. DOI: 10.1109/TGRS.2012.2220855 (cited on pages 17–19).

[65] S. Hong, "Detection of Small-Scale Roughness and Refractive Index of Sea Ice in Passive Satellite Microwave Remote Sensing," *Remote Sensing of Environment*, vol. 114, no. 5, 1136, 2010. DOI: 10.1016/j.rse.2009.12.015 (cited on page 18).

[66] A. Arenas-Pingarron, P. V. Brennan, and H. Corr, "Refraction Angle Calculation in Multilayered Ice for Wide-Beam Airborne Radar," in *IGARSS 2018 - 2018 IEEE International Geoscience and Remote Sensing Symposium*, Valencia: IEEE, 2018, 4146. DOI: 10.1109/IGARSS.2018.8518277 (cited on page 18).

[67] S. Leinss, G. Parrella, and I. Hajnsek, "Snow Height Determination by Polarimetric Phase Differences in X-Band SAR Data," *IEEE Journal of Selected Topics in Applied Earth Observations and Remote Sensing*, vol. 7, no. 9, 3794, 2014. DOI: 10.1109/JSTARS.2014.2323199 (cited on page 19).

[68] E. Cambria and B. White, "Jumping NLP Curves: A Review of Natural Language Processing Research [Review Article]," *IEEE Computational Intelligence Magazine*, vol. 9, no. 2, 48, 2014. DOI: 10.1109/MCI.2014.2307227 (cited on page 19).

[69] M. W. Libbrecht and W. S. Noble, "Machine Learning Applications in Genetics and Genomics," *Nature Reviews Genetics*, vol. 16, no. 6, 321, 2015. DOI: 10.1038/nrg3920 (cited on page 19).

[70] Y. Lecun, Y. Bengio, and G. Hinton, "Deep Learning," *Nature*, vol. 521, no. 7553, 436, 2015. DOI: 10.1038/nature14539 (cited on page 19).

[71] X. X. Zhu, D. Tuia, L. Mou, G.-S. Xia, L. Zhang, F. Xu, and F. Fraundorfer, "Deep Learning in Remote Sensing: A Comprehensive Review and List of Resources," *IEEE Geoscience and Remote Sensing Magazine*, vol. 5, no. 4, 8, 2017. DOI: 10.1109/MGRS.2017.2762307 (cited on page 19).

[72] L. Ma, Y. Liu, X. Zhang, Y. Ye, G. Yin, and B. A. Johnson, "Deep Learning in Remote Sensing Applications: A Meta-Analysis and Review," *ISPRS Journal of Photogrammetry and Remote Sensing*, vol. 152, 166, 2019. DOI: 10.1016/j.isprsjprs.2019.04.015 (cited on page 19).

[73] J. G. Greener, S. M. Kandathil, L. Moffat, and D. T. Jones, "A Guide to Machine Learning for Biologists," *Nature Reviews Molecular Cell Biology*, vol. 23, no. 1, 40, 2022. DOI: 10.1038/s41580-021-00407-0 (cited on page 19).

[74] J.-W. Lee and J.-H. Oh, "Hybrid Learning of Mapping and its Jacobian in Multilayer Neural Networks," *Neural Computation*, vol. 9, no. 5, 937, 1997. DOI: 10.1162/neco.1997.9.5.937 (cited on page 20).

[75] D. Kochkov, J. A. Smith, A. Alieva, Q. Wang, M. P. Brenner, and S. Hoyer, "Machine Learning–Accelerated Computational Fluid Dynamics," *Proceedings of the National Academy of Sciences*, vol. 118, no. 21, e2101784118, 2021. DOI: 10.1073/pnas.2101784118 (cited on page 20).

[76] S. Ardabili, A. Mosavi, and A. R. Várkonyi-Kóczy, "Advances in Machine Learning Modeling Reviewing Hybrid and Ensemble Methods," in *Engineering for Sustainable Future*, A. R. Várkonyi-Kóczy, Ed., vol. 101, Cham: Springer International Publishing, 2020, 215. DOI: 10.1007/978-3-030-36841-8_21 (cited on page 20).

[77] S. Kurz, H. De Gersem, A. Galetzka, A. Klaedtke, M. Liebsch, D. Loukrezis, S. Russenschuck, and M. Schmidt, "Hybrid modeling: towards the next level of scientific computing in engineering," *Journal of Mathematics in Industry*, vol. 12, no. 1, 8, 2022. DOI: 10.1186/s13362-022-00123-0 (cited on page 20).

[78] P. B. Gibson, W. E. Chapman, A. Altinok, L. Delle Monache, M. J. DeFlorio, and D. E. Waliser, "Training machine learning models on climate model output yields skillful interpretable seasonal precipitation forecasts," *Communications Earth & Environment*, vol. 2, no. 1, 1, 2021. DOI: 10.1038/s43247-021-00225-4 (cited on page 20).

[79] V. M. Krasnopolsky and M. S. Fox-Rabinovitz, "Complex hybrid models combining deterministic and machine learning components for numerical climate modeling and weather prediction," *Neural Networks*, vol. 19, no. 2, 122, 2006. DOI: 10.1016/j.neunet.2006.01.002 (cited on page 20).

[80] G. Weisz. "Hybrid Modeling - Combining Physics and Machine Learning to Understand Multiphase Transient Flow," Turbulent Flux, Accessed: Apr. 25, 2023. [Online]. Available: https://turbulentflux.com/combining-physics-and-machine-learning-to-understand-multiphase-transient-flow/ (cited on page 20).

[81] A. M. Schweidtmann, D. Zhang, and M. von Stosch, "A Review and Perspective on Hybrid Modeling Methodologies," *Digital Chemical Engineering*, vol. 10, 100136, 2024. DOI: 10.1016/j.dche.2023.100136 (cited on page 20).

[82] D. C. Psichogios and L. H. Ungar, "A Hybrid Neural Network-First Principles Approach to Process Modeling," *AIChE Journal*, vol. 38, no. 10, 1499, 1992. DOI: 10.1002/aic.690381003 (cited on page 20).

[83] H.-T. Su, N. Bhat, P. Minderman, and T. McAvoy, "INTEGRATING NEURAL NETWORKS WITH FIRST PRINCIPLES MODELS FOR DYNAMIC MODELING," in *Dynamics and Control of Chemical Reactors, Distillation Columns and Batch Processes*, Elsevier, 1993, 327. DOI: 10.1016/B978-0-08-041711-0.50054-4 (cited on page 20).

[84] M. A. Kramer, M. L. Thompson, and P. M. Bhagat, "Embedding Theoretical Models in Neural Networks," in *1992 American Control Conference*, 1992, 475. DOI: 10.23919/ACC.1992.4792111 (cited on page 20).

[85] T. A. Johansen and B. A. Foss, "Representing and Learning Unmodeled Dynamics with Neural Network Memories," in *1992 American Control Conference*, 1992, 3037. DOI: 10.23919/ACC.1992.4792705 (cited on page 20).

[86] M. L. Thompson and M. A. Kramer, "Modeling Chemical Processes Using Prior Knowledge and Neural Networks," *AIChE Journal*, vol. 40, no. 8, 1328, 1994. DOI: 10.1002/aic.690400806 (cited on page 20).

[87] M. P. Perrone and L. N. Cooper, "When Networks Disagree: Ensemble Methods for Hybrid Neural Networks," in *How We Learn; How We Remember: Toward an Understanding of Brain and Neural Systems*, ser. World Scientific Series in 20th Century Physics Volume 10, vol. Volume 10, WORLD SCIENTIFIC, 1995, 342. DOI: 10.1142/9789812795885_0025 (cited on page 20).

[88] A. Koppa, D. Rains, P. Hulsman, R. Poyatos, and D. G. Miralles, "A Deep Learning-Based Hybrid Model of Global Terrestrial Evaporation," *Nature Communications*, vol. 13, no. 1, 1912, 2022. DOI: 10.1038/s41467-022-29543-7 (cited on page 21).

[89] M. Reichstein, G. Camps-Valls, B. Stevens, M. Jung, J. Denzler, N. Carvalhais, and Prabhat, "Deep Learning and Process Understanding for Data-Driven Earth System Science," *Nature*, vol. 566, no. 7743, 195, 2019. DOI: 10.1038/s41586-019-0912-1 (cited on page 21).

[90] P. Clark Di Leoni, A. Mazzino, and L. Biferale, "Inferring Flow Parameters and Turbulent Configuration with Physics-Informed Data Assimilation and Spectral Nudging," *Physical Review Fluids*, vol. 3, no. 10, 104604, 2018. DOI: 10.1103/PhysRevFluids.3.104604 (cited on page 21).

Part II

Collected Papers

2

HYBRID MACHINE LEARNING FOREST HEIGHT ESTIMATION FROM TANDEM-X INSAR

Islam Mansour[1,2], Konstantinos Papathanassiou[1], Ronny Hänsch[1], and Irena Hajnsek[1,2]

1 Microwaves and Radar Institute, German Aerospace Center DLR, Germany
2 Institute of Environmental Engineering, ETH Zurich, Switzerland

Article published in *IEEE Journal of Selected Topics in Applied Earth Observations and Remote Sensing*
Citation: I. Mansour et al., "Hybrid Machine Learning Forest Height Estimation From TanDEM-X InSAR," *IEEE Transactions on Geoscience and Remote Sensing*, vol. 63, 1, 2025, DOI: 10.1109/TGRS.2024.3520387

Key findings:

- Developed a novel hybrid model combining machine learning with physical models for forest height estimation from single-baseline TanDEM-X data.
- Validated model across different tropical forest sites showing good generalization capabilities.

Author's contributions:

- Developed the novel hybrid modeling methodology.
- Created and processed datasets from TanDEM-X acquisitions.
- Performed data analysis and validation.

Co-author's contributions:

- K. Papathanassiou: Provided guidance and expertise on physical model development and underlying radar remote sensing principles.
- R. Hänsch: Provided guidance and expertise on machine learning component development and its optimization.
- I. Hajnsek: Provided supervision and guidance on overall research direction.
- All co-authors collectively contributed to the method development, result discussion, and manuscript revision.

Abstract

Combining machine learning (ML) with physical models can significantly impact retrieval algorithms designed to invert geophysical parameters from remote sensing data. Such hybrid models integrate physical knowledge with domain expertise through a joint architecture, potentially enhancing performance by increasing the efficiency and flexibility of the physical model as well as the generalization and interpretability of the ML predictions. This work introduces a hybrid model for estimating forest height using single-baseline, single-polarization TanDEM-X interferometric coherence measurements. In this model, the vertical reflectivity profile is derived as a function of input features, including topographic and acquisition geometry descriptors, using a multilayer perceptron network. This profile is then used to invert forest height by leveraging the established physical relationship connecting the vertical reflectivity profile to forest height. The developed model is applied and validated on several TanDEM-X acquisitions over tropical sites with different acquisition geometries, and its performance is assessed against reference data derived from airborne LiDAR measurements.

Keywords

Accuracy, Coherence, Decorrelation, Forest height, Forestry, Geophysical measurements, InSAR, Polynomials, Reflectivity, Remote sensing, TanDEM-X, Training, Vegetation, forest height, forest height estimation, forest structure, hybrid modeling, interferometry, machine learning, machine learning (ML), physical modeling, remote sensing, synthetic aperture radar, temporal decorrelation, topographic effects

2.1 INTRODUCTION

Accurate measurements of forest height are relevant for forest inventory, forest disturbance and carbon sequestration monitoring [1], [2], [3], [4], [5]. SAR interferometry, combined with polarimetric and/or spatial baseline diversity, is today one of the established remote sensing techniques for obtaining continuous forest height estimates of significant accuracy at large spatial scales. The related approaches are in first line model-based, exploring the inherent sensitivity of interferometric measurements to the 3D distribution of scatterers within forests. Model-based forest height inversion performance is well-understood and validated across various frequencies, from X- to P-band, for different forest and terrain conditions [6], [7], [8], [9], [10], [11], [12]. The achieved performance critically depends on the definition of the inversion model, particularly the parameterization of the vertical reflectivity profile. While accurate and generic parameterization requires a certain number of parameters to be described, the constraint of achieving a balanced inversion model dictates the number of parameters needed to parameterize the vertical reflectivity profile to be matched by the number of available measurements. In the absence of a sufficient number of measurements, only oversimplified model parameterizations become possible, or ones constrained by overly strict assumptions, resulting in severely compromised performance as the model loses its ability to adapt to the underlying scattering.

2.1.1 *Machine Learning vs Physical vs Hybrid Modeling*

Both ML and Deep Learning (DL) approaches have been in the last years applied to various inverse remote sensing data problems with noticeable success. Data-driven ML and DL approaches are able to recognize patterns and relationships in multi-parameter data spaces with high efficiency even when these are not apparent. They are particularly powerful when applied to parameter estimation problems where the underlying physical relationships are not established and/or lack a forward or inverse model description.

Following this trend, a number of ML and DL approaches have been proposed in recent years addressing the problem of forest height estimation from multi-parameter SAR data alone or com-

bined with other remote sensing data sets. The majority of them attempts to establish a direct relationship between measured SAR parameters as backscatter intensities or interferometric coherences and forest height using supervised or unsupervised learning implementations [13], [14], [15], [16], [17], [18], [19], [20], [21], [22], [23], [24], [25].

However, although the achieved performance of such approaches is often impressive, their generalization and interpretability are rather limited especially in underdetermined inverse problems addressed with limited or even without prior knowledge and domain expertise. At the same time pure data-driven approaches require large amount of reference data for a wide range of problem conditions that are often not available.

One way to overcome these disadvantages has been proposed in the context of Physics-Informed ML approaches that integrate ML and physical / mathematical models [26]. This allows to combine the expressiveness of data-based approaches with the interpretability and generalization of physical models. In this context, this study attempts to establish such a hybrid inversion framework, that combines ML and physical modeling components for the estimation of forest height from single baseline single-polarimetric TanDEM-X interferometric coherence. For this the vertical reflectivity profile is derived as a function of input features, including topographic and acquisition geometry descriptors, using a multilayer perceptron network. In a second step, the predicted vertical reflectivity profile is used to invert forest height taking advantage of the established physical relation connecting the vertical reflectivity profile to forest height.

The hybrid modeling approach is expected i) to utilize the capability of ML techniques in identifying non-obvious relationships or correlations, such as change in scattering behavior with terrain topography, ii) to take advantage of the well-established physical models to restrict the possible solution space down to physically meaningful solutions, making the training process more efficient and reducing the diversity of training data required (as for example the need for reference data at different terrain conditions).

The paper is structured as follows: Section II introduces the data used in this work, Section III provides the technical background required, Section IV presents the proposed hybrid model and de-

scribes its implementation, Section V discusses the results obtained when applying the proposed hybrid model to the TanDEM-X acquisitions, and finally Section VI draws the conclusions.

2.2 STUDY AREA AND EXPERIMENTAL DATA

This study uses data from three Gabonese tropical forest sites: Lopé, Mabounié, and Rabi. The Lopé site is within the Lopé National Park, consisting of Savannah and denser forest of varying species composition and density. The maximum tree height exceeds 50 m in many stands. The terrain is hilly, with many local slopes steeper than 20°. Mabounié is a former mining exploration site. Most of the test site is covered by mature primary forest stands (with tree heights between 40 and 50 m) and degraded forest (with tree heights around 20 m). The terrain is relatively flat with few gentle slopes. Finally, the Rabi test site consists of a diverse mix of upland and wet forest with a mean tree height of about 40 m, and features fairly flat topography.

A large set of TanDEM-X images acquired over the three sites is used. Table 2.1 summarizes the acquisitions and their geometry. The (2π) Height of Ambiguity (HoA) sign indicates the orbit direction: a positive sign indicates an ascending orbit, while a negative sign indicates a descending orbit.

Full waveform LiDAR data were collected during the AfriSAR 2016 campaign in February 2016 by National Aeronautics and Space Administration (NASA)'s airborne Land, Vegetation, and Ice Sensor (LVIS) Light Detection and Ranging (LiDAR) sensor. The LVIS footprints range from 18 to 22 m, and the waveforms were resampled to a regular 20 m x 20 m grid with corresponding RH98 and DTM models [27], [28]. The resampled RH98 heights are used as the reference heights $h_{\mathrm{Ref}} = RH98$.

2.3 METHODOLOGY

The measured interferometric coherence ($\tilde{\gamma}_{obs}$) between two interferometric images $s_1(\vec{w})$ and $s_2(\vec{w})$ acquired at a given polarization $\vec{w}$ expressed as follows [29], [30]:

Table 2.1: TanDEM-X Datasets, Sites, Scene ID's, Height of Ambiguity [m] (HoA), Nominal incidence angle [°]

No	Site	Scene ID	HoA	θ_0
1	Lopé	TDM1_SAR__COS_BIST_SM_S_SRA_20190610T173107_20190610T173115	52.45	46.18
2	Lopé	TDM1_SAR__COS_BIST_SM_S_SRA_20160125T173041_20160125T173048	-65.22	44.44
3	Lopé	TDM1_SAR__COS_BIST_SM_S_SRA_20111002T045625_20111002T045633	86.34	46.08
4	Lopé	TDM1_SAR__COS_BIST_SM_S_SRA_20121226T045626_20121226T045634	94.89	45.10
5	Lopé	TDM1_SAR__COS_BIST_SM_S_SRA_20121215T045627_20121215T045635	95.41	46.68
6	Mabounié	TDM1_SAR__COS_BIST_SM_S_SRA_20161017T050537_20161017T050545	-80.30	37.07
7	Mabounié	TDM1_SAR__COS_BIST_SM_S_SRA_20161017T050530_20161017T050538	-80.90	37.09
8	Mabounié	TDM1_SAR__COS_BIST_SM_S_SRA_20161028T050538_20161028T050546	-87.32	39.30
9	Mabounié	TDM1_SAR__COS_BIST_SM_S_SRA_20161108T050538_20161108T050546	-95.81	41.39
10	Rabi	TDM1_SAR__COS_BIST_SM_S_SRA_20161017T050558_20161017T050606	-78.51	37.04
11	Rabi	TDM1_SAR__COS_BIST_SM_S_SRA_20161028T050559_20161028T050607	-85.27	39.24
12	Rabi	TDM1_SAR__COS_BIST_SM_S_SRA_20161028T050552_20161028T050600	-85.95	39.27
13	Rabi	TDM1_SAR__COS_BIST_SM_S_SRA_20161108T050552_20161108T050600	-94.21	41.37

$$\tilde{\gamma}_{obs}\left(\kappa_z, \vec{w}\right) = \frac{\left\langle s_1\left(\vec{w}\right) s_2^*\left(\vec{w}\right)\right\rangle}{\sqrt{\left\langle s_1\left(\vec{w}\right) s_1^*\left(\vec{w}\right)\right\rangle \left\langle s_2\left(\vec{w}\right) s_2^*\left(\vec{w}\right)\right\rangle}} \tag{2.1}$$

The vertical wavenumber (in rad/m), κ_z, expresses the sensitivity of the interferometric phase to height changes [10], [31]:

$$\kappa_z = m\frac{2\pi}{\lambda}\frac{\Delta\theta}{\sin\left(\theta_0 + \alpha\right)} \tag{2.2}$$

where θ_0 is the radar look angle, $\Delta\theta$ is the look angle difference induced by the spatial baseline, λ is the wavelength, and α is the ground range terrain slope. The factor m depends on the interferometric acquisition mode: $m = 2$ for monostatic while $m = 1$ for bistatic acquisitions. An equivalent way to express the sensitivity of the interferometric phase-to-height changes is the Height of Ambiguity $HoA = 2\pi/\kappa_z$.

The measured interferometric coherence can be factorized as [32], [33], [34], [35]:

$$\tilde{\gamma}_{obs}\left(\kappa_z, \vec{w}\right) = \tilde{\gamma}_{Tmp}\left(\vec{w}\right)\tilde{\gamma}_{Rg}\left(\kappa_z\right)\tilde{\gamma}_{Sys}\left(\vec{w}\right)\tilde{\gamma}_{\mathrm{Vol}}\left(\kappa_z, \vec{w}\right) \tag{2.3}$$

where $\tilde{\gamma}_{Tmp}(\vec{w})$ accounts for the temporal decorrelation, $\tilde{\gamma}_{Rg}(\kappa_z)$ accounts for the range spectral decorrelation induced by the spatial baseline, $\tilde{\gamma}_{Sys}(\vec{w})$ comprises various system-induced decorrelations, including the decorrelation due to the additive noise component, and finally, $\tilde{\gamma}_{\text{Vol}}(\kappa_z, \vec{w})$ is the decorrelation induced by the vertical extent of the scatterer.

In the case of bistatic TanDEM-X acquisitions the factor m in Eq. (2.2) becomes 1 and the temporal decorrelation contribution $\tilde{\gamma}_{Tmp} = 1$. The system decorrelation contribution $\tilde{\gamma}_{Sys}$ and the range spectral decorrelation $\tilde{\gamma}_{Rg}$ can be accurately estimated and compensated making an accurate estimation of the volume decorrelation $\tilde{\gamma}_{\text{Vol}}$ contribution possible [36], [37]. The measured interferometric coherence and several decorrelation contributions depend on the polarization of the images used to construct the interferogram. However, since polarimetric diversity is not considered in the following, the polarization dependence is omitted.

2.3.1 *Vertical Reflectively Profile and Forest Height Inversion*

The volume decorrelation contribution $\tilde{\gamma}_{\text{Vol}}(\kappa_z)$ is related to the vertical reflectivity profile $f(z)$ of the forest and its top canopy height h_v as [30], [38], [39]:

$$\tilde{\gamma}_{\text{Vol}}(\kappa_z) = e^{i\kappa_z z_o} \frac{\int_0^{h_v} f(z)\, e^{i\kappa_z z} dz}{\int_0^{h_v} f(z)\, dz} \tag{2.4}$$

where z denotes the position along the vertical axis. The vertical reflectivity profile $f(z)$ represents the vertical distribution of scatterers and as such depends on the frequency, polarization as well as the acquisition geometry. The lower boundary of $f(z)$ is determined by the reference height z_0, which is related to the location of the underlying ground. The upper boundary of $f(z)$ is defined by $z_0 + h_v$.

In the case of TanDEM-X, only a single $\tilde{\gamma}_{\text{Vol}}(\kappa_z)$ measurement is available, at least for a very long-time interval, while the ground topography z_0, forest height h_v and the parameterization of the vertical reflectivity profile $f(z)$ have to be considered as unknowns.

2.3.2 *Modeling Vertical Reflectivity Profiles*

The vertical reflectivity profile can be expressed in terms of a polynomial series expansion. Originally the Legendre polynomials were used for this [30], [40], [41], [42]:

$$f(z, a_n) = \sum_{n=1}^{\infty} a_n P_n(z) \tag{2.5}$$

where $P_n(z)$ are the Legendre polynomials (see Figure 2.1) and a_n the associated Legendre coefficients that are obtained as:

$$a_n = \frac{2n+1}{2} \int_{-1}^{1} f(z) P_n(z) dz \tag{2.6}$$

The summation extends to infinity, although, in practice, it is truncated to a small number of terms. The proposed Legendre polynomials have proven to be a well-suited generic basis as they allow accurate reconstruction of $f(z, a_n)$ with a small number of polynomials for various forest conditions.

2.4 MODEL DEFINITION

The proposed hybrid model utilizes an ML algorithm to predict the underlying vertical reflectivity profile $f(z, a_n)$, expressed in terms of the Legendre series expansion (see Eq. (2.5)), as a function of features including interferometric volume coherence, acquisition geometry (expressed by the vertical wavenumber) and terrain slope. The predicted (or "learned") vertical reflectivity profile $f(z, a_n)$ is then used in the inversion of Eq. (2.4) to estimate the forest height. Figure 2.2 shows a conceptual representation of the architecture and functionality of the proposed hybrid model in the training and inference phase.

2.4.1 *Model Training*

In the training phase, the terrain-corrected vertical wavenumber (see Eq. (2.2)) and the reference forest height h_{Ref} are used in Eq. (2.4) to predict the absolute value of the volume decorrela-

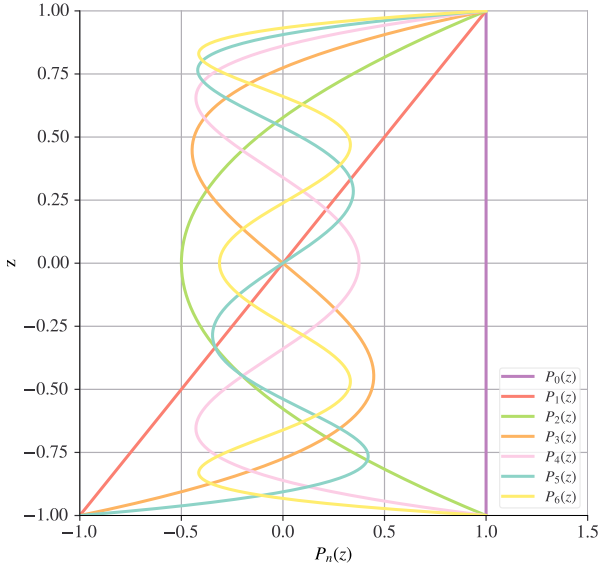

Figure 2.1: A graphical illustration showcasing the initial seven Legendre polynomials plotted as a function of x, highlighting their distinct properties and orthogonality within the given domain.

tion $|\tilde{\gamma}^{P}_{\mathrm{Vol}}(\kappa_z, h_{\mathrm{Ref}}, f(z, a_n))|$ for a given vertical reflectivity profile $f(z, a_n)$ expressed by a predefined number ($N = 3$ or $N = 7$) of Legendre polynomials using the associated coefficients a_n (see Eq. (2.6)). The obtained volume decorrelation prediction is then compared against the volume decorrelation $|\tilde{\gamma}_{\mathrm{Vol}}(\kappa_z)|$ as estimated from the TanDEM-X data.

The training process begins with an arbitrary initialization of the Legendre coefficients a_n. The coefficients are then iteratively updated to minimize the difference between the predicted and the actual volume decorrelation values. The coefficients are determined by a multilayer perceptron to establish the nonlinear relationship between them and the set of input features by minimizing the difference between the predicted and estimated volume decorrelation. The set of input features includes the terrain corrected vertical wavenumber κ_z, the volumetric coherence $|\tilde{\gamma}_{\mathrm{Vol}}(\kappa_z)|$, the

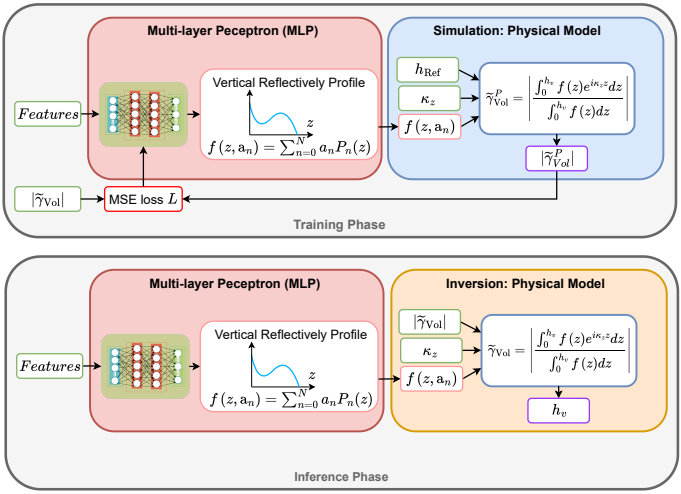

Figure 2.2: Conceptual architecture and functionality of the hybrid model in the training (top) and inference phase (bottom).

incidence angle to the ellipsoid corresponding to the angle between the Line-of-Sight and the normal to the local ellipsoid θ_0, the local incidence angle θ_{loc}, and the terrain slope in the range direction α. The optimization process employs a suitable loss function mean squared error (MSE) and the Adam optimization algorithm [43]:

$$\mathcal{L}\left(\tilde{\gamma}^P_{\mathrm{Vol}}, \tilde{\gamma}_{\mathrm{Vol}}\right) = \sum_{i=1}^{m} \left(\left|\tilde{\gamma}^P_{\mathrm{Vol}}(\kappa_z, h_{\mathrm{Ref}}, f(z, a_n))\right| - \left|\tilde{\gamma}_{\mathrm{Vol}}(\kappa_z)\right| \right)^2 \quad (2.7)$$

subject to:

$$f(z,\ a_n) = \sum_{n=1}^{N} a_n\ (\kappa_z, |\tilde{\gamma}_{\mathrm{Vol}}|, \theta, \theta_{\mathrm{loc}}, \alpha)\ \ P_n\ (z) \quad (2.8)$$

This way the model enhances its ability to link the features and the Legendre coefficients of the vertical reflectivity profile.

An important point is to constrain positive reflectivity profiles in order to ensure physically plausible vertical reflectivity functions. To enforce positive profiles a hyperbolic tangent activation

function is incorporated. Furthermore, to ensure the physical plausibility of the model predictions, a linear (regression) layer with a *MinMaxNorm* kernel constraint is also integrated to constrain the weights of the model within a certain range:

$$\sum_{n=1}^{N} a_n \left(\kappa_z, |\tilde{\gamma}_{\mathrm{Vol}}(\kappa_z)|, \theta, \theta_{\mathrm{loc}}, \alpha\right) P_n\left(z\right) \geq 0 \tag{2.9}$$

For $n = 1, 2, 3, \ldots, N$ and $0 \leq h_v \leq h_{\max}$, where $h_{\max}$ is set to 70. This constraint ensures that the predicted vertical reflectivity profiles are positive and fall within a reasonable range.

2.4.2 *Model Inversion*

Once the model is trained, it can be used to estimate forest height from the input features. In a first step, the input features are used to predict the vertical reflectivity profile $f(z, a_n)$, which is subsequently used to estimate the forest height from the $|\tilde{\gamma}_{\mathrm{Vol}}(\kappa_z)|$ measurements in terms of Eq. (2.4). This last step can be implemented in terms of a look-up table.

Note that, the interferometric volume coherences used for training and inversion are derived from the interferometric coherences estimated using a 7x7 window estimator as described in [10].

2.4.3 *Model Implementation*

Three different models have been developed, differing in the number and range of vertical wavenumbers (e.g., number of TanDEM-X acquisitions) used for training and in the number of Legendre polynomials used for the definition of the vertical reflectivity profiles. The three models are summarized in Table 2.2. The first model (A) was trained using a single TanDEM-X acquisition and used three Legendre polynomials ($N = 3$) to define the vertical reflectivity profiles. The second model (B) was trained using three TanDEM-X acquisitions (two ascending and one descending) with different vertical wavenumbers and three Legendre polynomials ($N = 3$) for the definition of the vertical reflectivity profiles. Finally, the third model (C) also used three TanDEM-X acquisitions for training (the same as for model B) but seven Legendre polynomials ($N = 7$)

for defining the vertical reflectivity profiles. For each of the three models, the available reference data were split such that 60% of the data was used for training and 40% for validation.

Table 2.2: Models and associated number of Legendre Coef. and TanDEM-X acquisition(s) and HoA used for training (as shown in Figure 2.2, top).

Model	Coef.	HoA (m)	ML Input Features	PM Inputs
A	3	-65.22 (No 2 in Table 2.1)	κ_z, $\lvert\tilde{\gamma}_{\mathrm{Vol}}(\kappa_z)\rvert$, θ, θ_{loc}, α	h_{Ref}, κ_z, $f(z, a_n)$
B	3	52.45 (No 1 in Table 2.1) -65.22 (No 2 in Table 2.1) 95.41 (No 5 in Table 2.1)	κ_z, $\lvert\tilde{\gamma}_{\mathrm{Vol}}(\kappa_z)\rvert$, θ, θ_{loc}, α	h_{Ref}, κ_z, $f(z, a_n)$
C	7	52.45 (No 1 in Table 2.1) -65.22 (No 2 in Table 2.1) 95.41 (No 5 in Table 2.1)	κ_z, $\lvert\tilde{\gamma}_{\mathrm{Vol}}(\kappa_z)\rvert$, θ, θ_{loc}, α	h_{Ref}, κ_z, $f(z, a_n)$

The data space available for training in the case of using one (as in model A) or three (as in models B and C) TanDEM-X acquisitions is shown in Figure 2.3. There, the estimated volume coherence $|\tilde{\gamma}_{\mathrm{Vol}}(\kappa_z)|$ for the one (on the left) and the three (on the right) TanDEM-X acquisitions used for training are plotted against the product $h_{\mathrm{Ref}}\,\kappa_z$, i.e., the product of the (terrain corrected) vertical wavenumber κ_z with the reference forest height h_{Ref} for each sample in the scene. The increased training space when using three TanDEM-X acquisitions is evident.

For training, acquisitions with (very) different vertical wavenumbers are ideal to provide maximum coherence contrast. And, of course, acquisitions with vertical wavenumbers similar to those targeted for inversion are likely to yield better inversion performance. In this study, an acquisition with moderately different vertical wavenumbers and one acquisition in opposite geometry (descending) were preferred to avoid overly optimistic inversion

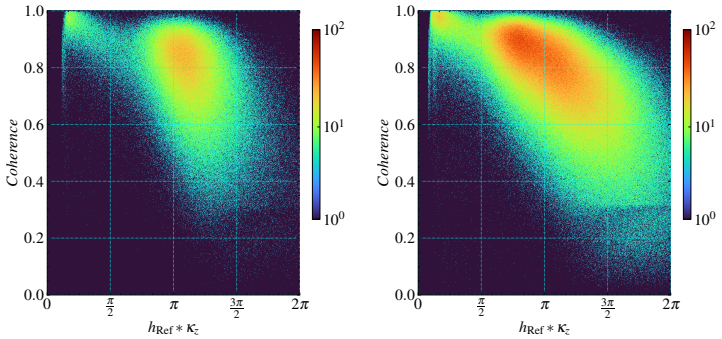

(a) Data space available for 1 HoA. **(b)** Data space available for 3 HoA.

Figure 2.3: Volume coherence $|\widetilde{\gamma}_{Vol}(\kappa_z)|$ vs. $h_{\mathrm{Ref}}\ \kappa_z$ for the data space available for training when one, the No 2 in Table 2.1, (top) or three, the No 1, 2 and 5 in Table 2.1, (bottom) TanDEM-X acquisitions are used. The colors represent the relative sample density, ranging from dark blue (low density) to dark red (high density).

performance, thereby highlighting both the strengths and remaining limitations of the proposed approach.

2.5 RESULTS AND DISCUSSION

The three established models are applied to the TanDEM-X dataset and validated against the available reference heights. The validation focuses on assessing the inversion performance by considering the number and range of vertical wavenumbers (e.g., TanDEM-X acquisitions) used in the training phase and the number of Legendre polynomials used for the definition of the reflectivity profiles. First, the performance obtained when training and inversion occur on the same site, but for different acquisitions, is discussed. For this case, the Lopé site is chosen. In a second step, the performance obtained when the Lopé model is applied to the other two sites, Mabounié and Rabi, for which it has not been trained, is evaluated.

The performance achieved over the Lopé site is summarized in the three Figures 2.4 to 2.6. Figure 2.4 shows the vertical reflectivity profiles "learned" by the three models, A (top), B (middle) and C (bottom), for different terrain slopes. In the absence of a direct

way to assess the correctness of the vertical reflectivity profiles "learned" by the models, their slope dependence is one of the few, if not the only, test that allows some conclusions about their physical credibility.

Indeed, the ability of the model to predict a stronger ground scattering contribution on positive slopes facing towards the radar than on negative slopes facing away is consistent with the physical anticipation and thus an indication for the credibility of the 'learned' vertical reflectivity profiles. The light shadow colors indicate the variance of the profiles within each slope interval in order to illustrate the significance of the terrain adaptation provided by the ML component. With increasing number of acquisitions used for training the terrain adaptation improves as indicated by the smaller profile variance of models B and C with respect to Model A. In addition, the improved vertical resolution as the number of polynomials increases from three to seven is evident when comparing the three models. From model A to C, there is a more detailed definition of the different layers of the vertical structure of the canopy.

Figure 2.5 shows the plots obtained by plotting the volume coherence $|\tilde{\gamma}_{\mathrm{Vol}}(\kappa_z)|$ against the product $h_v\ \kappa_z$ for each of the five TanDEM-X acquisitions and for each of the three models. From left to right, the plots corresponding to acquisitions 1 to 5 (as referred to in Table 2.1) are plotted. The forest height estimates in the top row are obtained from model A, in the middle from model B and in the bottom row by using model C. The framed plots indicate the acquisitions used for training. Similarly, Figure 2.6 shows the corresponding validation plots of the estimated forest height h_v for each of the five TanDEM-X acquisitions (1 to 5 from left to right, respectively) plotted against the reference forest height h_{Ref}. The plots are arranged by model, with model A in the top row, model B in the middle row, and model C in the bottom row.

To better understand the results, we present the following figures that illustrate the model's performance across different scenarios.

The performance is characterized by the using the mean absolute error (MAE):

$$\mathrm{MAE} = \frac{1}{n}\sum_{i=1}^{n}\left|h_{v_i} - h_{\mathrm{Ref}_i}\right| \tag{2.10}$$

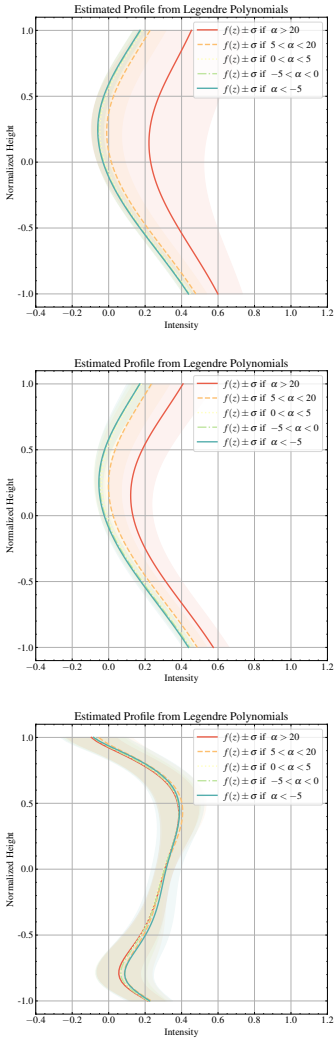

Figure 2.4: Set of vertical reflectivity profiles "learned" by the three models, A (top), B (middle), and C (bottom), for different terrain slopes. Positive slopes facing towards the radar are consistently estimated with a stronger ground scattering contribution than profiles on negative slopes (facing away). The light colors indicate the variance of the profiles within each slope interval.

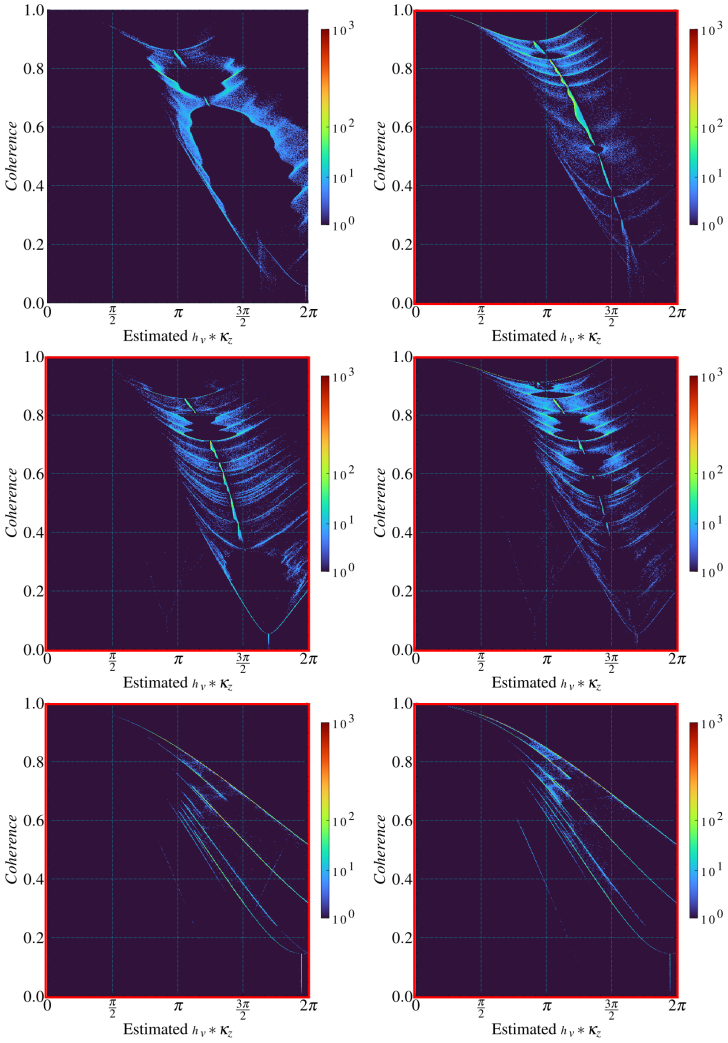

Figure 2.5: Volume coherence vs. $h_v\,\kappa_z$ product (continued 1/3).

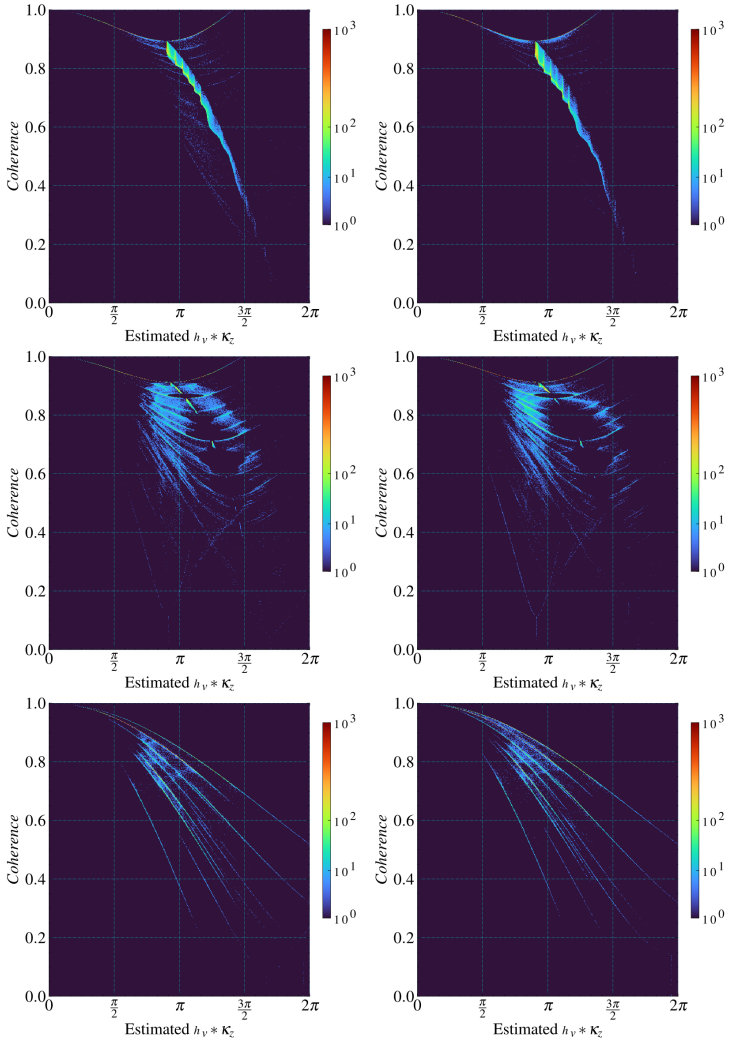

Figure 2.5: Volume coherence vs. $h_v \, \kappa_z$ product (continued 2/3).

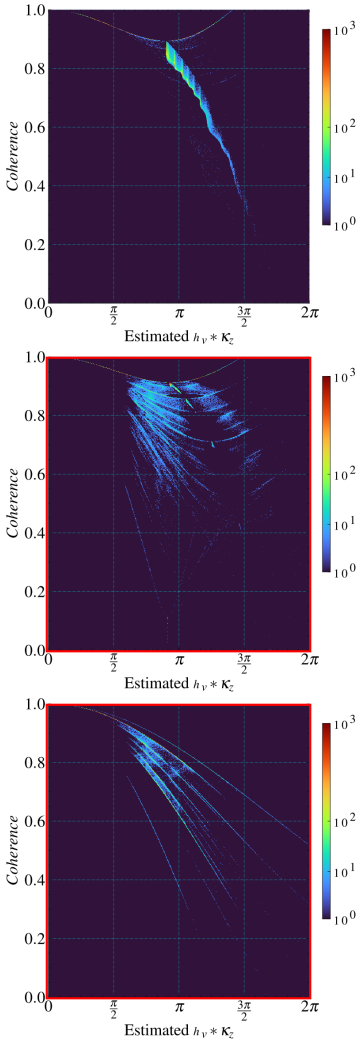

Figure 2.5: $|\widetilde{\gamma}_{\mathrm{Vol}}(\kappa_z)|$ vs. $h_v\,\kappa_z$ product. The plots are generated using the Lopé forest height estimates h_v obtained from the inversion of each of the five TanDEM-X acquisitions (from left to right, acquisitions 1–5 as in Table 2.1) using the three models (A, B and C from top to bottom). The framed plots indicate the acquisitions used for training. The colors represent the relative sample density, ranging from dark blue (low density) to dark red (high density).

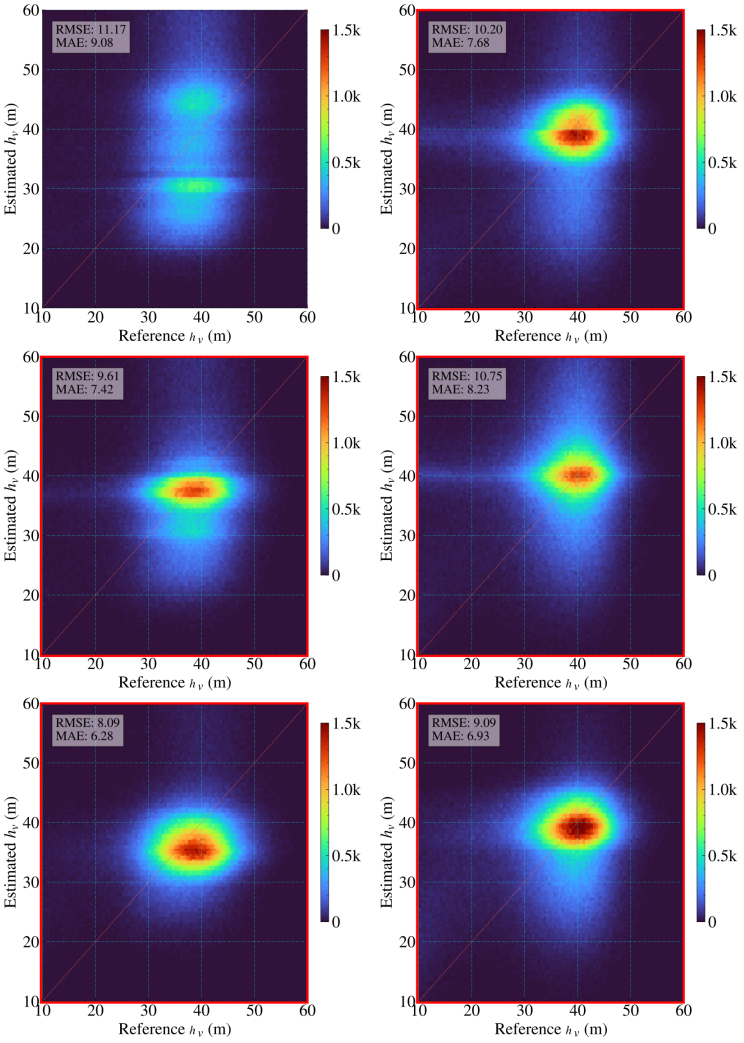

Figure 2.6: Estimated h_v vs. reference h_{Ref} forest height (continued 1/3).

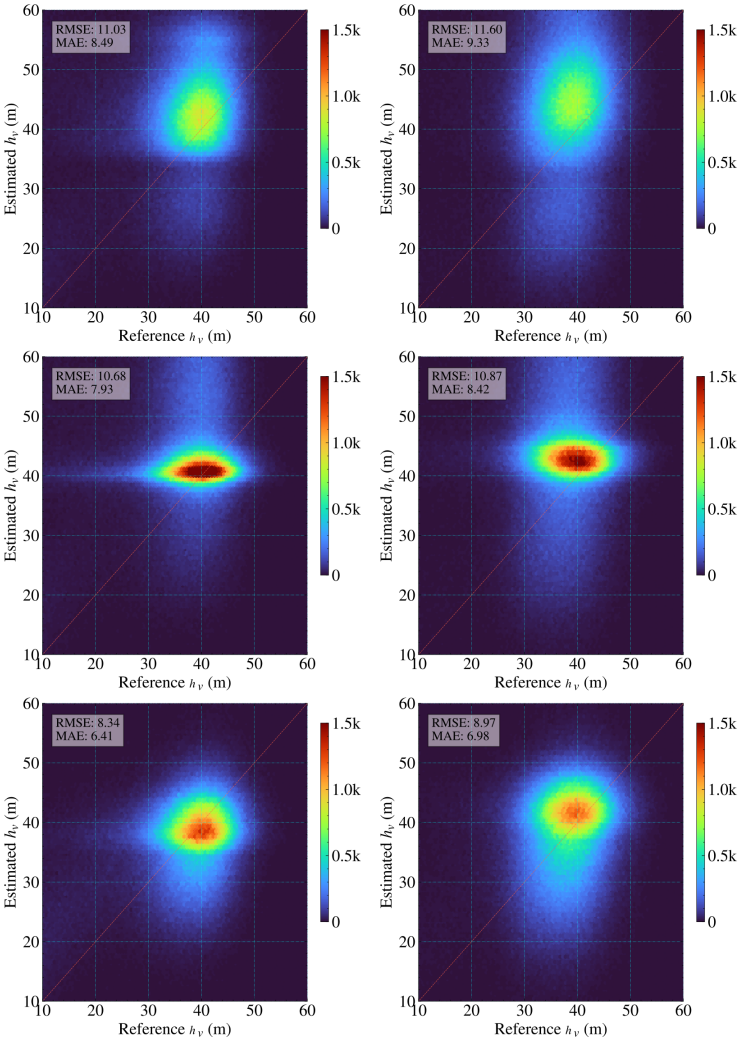

Figure 2.6: Estimated h_v vs. reference h_{Ref} forest height (continued 2/3).

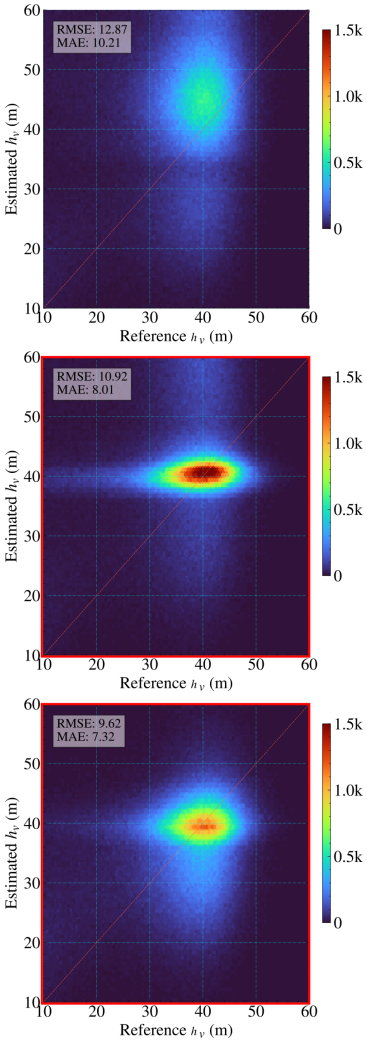

Figure 2.6: Estimated h_v vs. reference h_{Ref} forest height. The plots are generated using the Lopé forest height estimates h_v obtained from the inversion of each of the five TanDEM-X acquisitions (from left to right, acquisitions 1–5 according to their numbering in Table 2.1) using the three models (A, B and C from top to bottom). The framed plots indicate the acquisitions used for training. The colors represent the relative sample density, ranging from dark blue (low density) to dark red (high density).

and the root mean square error (RMSE):

$$\mathrm{RMSE} = \sqrt{\frac{1}{n}\sum_{i=1}^{n}\left(h_{v_i} - h_{\mathrm{Ref}_i}\right)^2} \tag{2.11}$$

In Figure 2.5, each plot visualizes the solution space provided by the set of "learned" vertical reflectivity profiles for the corresponding TanDEM-X acquisition. Note that the set of "learned" vertical reflectivity profiles is intrinsic to each of the three models, i.e., the same set of learned profiles is used for each acquisition. Each "learned" vertical reflectivity profile $f(z,\, a_n)$ draws a unique curve in the $|\tilde{\gamma}_{\mathrm{Vol}}(\kappa_z)|$ vs. $h_v\, \kappa_z$ plane according to Eq. (2.4). In this sense, an optimal model should provide a set of "learned" vertical reflectivity profiles that are able to cover the whole data space in a unique way, and this over a wide range of vertical wavenumbers.

As can be seen, this is not the case for model A. While for the acquisition used for training, the set of "learned" vertical reflectivity profiles provides an acceptable coverage of the data space (i.e., compare with Figure 2.3 left), this is not the case for all other acquisitions (e.g., vertical wavenumbers). Furthermore, for acquisition 1, the acquisition with the largest vertical wavenumber (e.g., smallest HoA), the solution space becomes ambiguous. This behavior directly reflects on the corresponding validation plots in Figure 2.5 (top row), where unbiased results are obtained only for the acquisition used for training. For the acquisitions 3, 4, and 5 with larger HoA, the forest heights are overestimated, whereas for acquisition 1 with the smallest HoA the ambiguous solution space becomes evident. The MAE range between 7.68 and 10.21 meters, while the RMSE fluctuates between 10.20 and 12.87 meters, as shown in Table 2.3. Overall, Model A has the highest mean errors among the three models, with an overall MAE of 8.89 meters and an overall RMSE of 11.33 meters, indicating its limited performance.

Model B performs better, as the "learned" vertical reflectivity profiles are able to cover almost the whole data space for all available acquisitions. There are only small data sub-spaces not covered by the solution space provided, as well as solution achieved at the ambiguous part of $h_v\, \kappa_z$ range, i.e., after reaching the first coherence minimum. These are indicators for a sub-optimum set of "learned" vertical reflectivity profiles. However, this is not reflected

Table 2.3: Performance comparison of different models across scenes based on RMSE and MAE metrics.

Scene No	Site	RMSE [m]	MAE [m]
		Model A	
Scene 1	Lope	11.17	9.08
Scene 2	Lope	10.20	7.68
Scene 3	Lope	11.03	8.49
Scene 4	Lope	11.60	9.33
Scene 5	Lope	12.87	10.21
Overall		11.33	8.89
		Model B	
Scene 1	Lope	9.61	7.42
Scene 2	Lope	10.75	8.23
Scene 3	Lope	10.68	7.93
Scene 4	Lope	10.87	8.42
Scene 5	Lope	10.92	8.01
Overall		10.58	8.02
		Model C	
Scene 1	Lope	8.09	6.28
Scene 2	Lope	9.09	6.93
Scene 3	Lope	8.34	6.41
Scene 4	Lope	8.97	6.98
Scene 5	Lope	9.62	7.32
Overall		8.84	6.79

on the performance plots (Figure 2.6 middle) where the MAE values range between 7.42 meters and 8.42 meters, and the RMSE values between 9.61 meters and 10.92 meters, manifesting the improved performance compared to model A, as shown in Table 2.3. Overall, Model B achieves a lower mean MAE of 8.02 meters and a mean RMSE of 10.58 meters, indicating a notable performance improvement over Model A.

Finally, model C performs best, as the "learned" vertical reflectivity profiles are able to cover almost the whole data space in a

consistent way across all available acquisitions. This is reflected also on its superior performance with lower MAE levels ranging from 6.28 to 7.32 meters and lower RMSE levels ranging from 8.09 to 9.62 meters, as summarized in Table 2.3. Notably, Model C achieves the lowest overall MAE and RMSE values among all models, with an overall MAE of 6.79 meters and an overall RMSE of 8.84 meters. Furthermore, the performance is very consistent across the entire range of vertical wavenumbers indicating the ability of the "learned" vertical reflectivity profiles to describe the underlying reflectivity.

In addition to the two cases using $N = 3$ (Model B) and $N = 7$ (Model C) Legendre coefficients to describe the vertical reflectivity profiles, models with varying N-values ranging from 3 to 9 were implemented and tested to assess their impact on inversion performance, consistently using the same three TanDEM-X acquisitions for training. The performance of models with $N = 4, 5$, and 6, as expected, lies between the $N = 3$ and $N = 7$ cases, gradually improving with increasing N. For models with higher N-values ($N = 8$ and 9), performance progressively deteriorates due to overfitting.

Table 2.4: Performance comparison of model C across sites based on RMSE and MAE metrics.

Scene No	Site	RMSE [m]	MAE [m]
	Model C		
Scene 6	Mabounié	10.02	7.90
Scene 7	Mabounié	9.84	7.80
Scene 8	Mabounié	10.98	8.58
Scene 9	Mabounié	11.10	8.73
Scene 10	Rabi	8.84	6.98
Scene 11	Rabi	8.70	6.81
Scene 12	Rabi	8.93	6.97
Scene 13	Rabi	11.34	8.95

After evaluating the performance obtained when inverting acquisitions of the same area where training was performed but acquired with different vertical wavenumbers than the one(s) used for train-

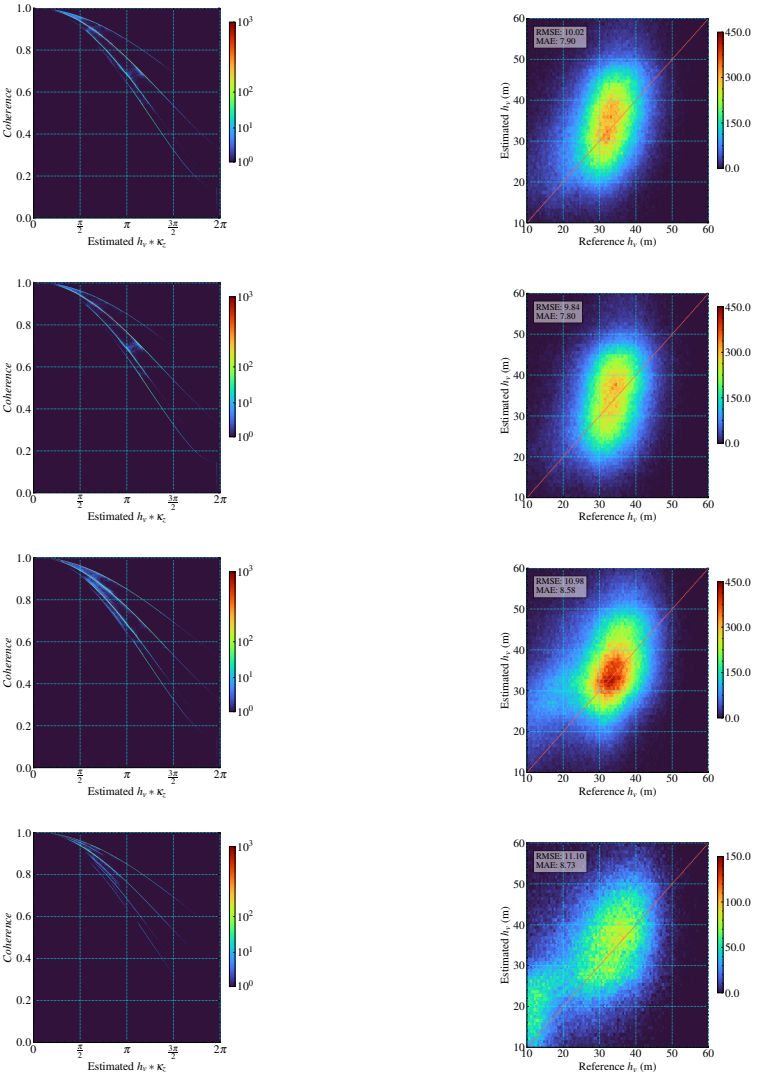

Figure 2.7: Volume coherence $|\widetilde{\gamma}_{\mathrm{Vol}}(\kappa_z)|$ vs. $h_v\,\kappa_z$ plots (left) and validation plots (right) for the four Mabounié scenes (from top to bottom: scenes 6–9, numbered as in Table 2.1). The colors represent the relative sample density, ranging from dark blue (low density) to dark red (high density).

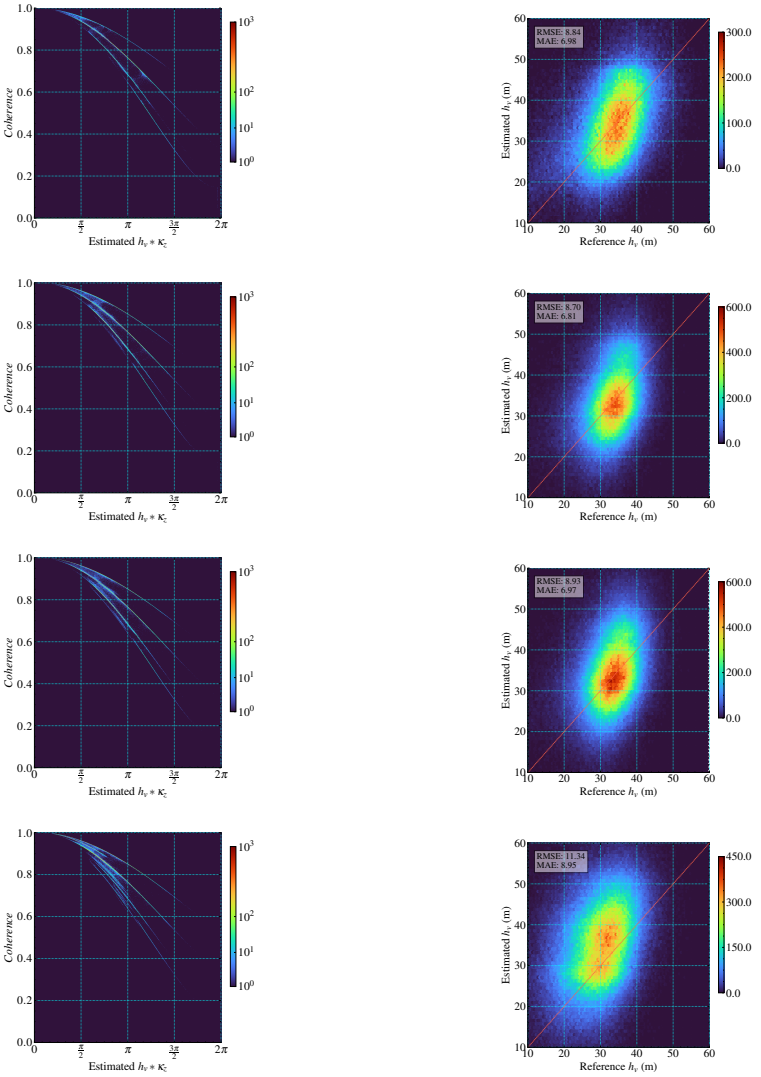

Figure 2.8: Volume coherence $|\widetilde{\gamma}_{\mathrm{Vol}}(\kappa_z)|$ vs. $h_v\,\kappa_z$ plots (left) and validation plots (right) for the four Rabi scenes (from top to bottom: scenes 10–13, numbered as in Table 2.1). The colors represent the relative sample density, ranging from dark blue (low density) to dark red (high density).

ing, it is time to validate the transferability of the model to sites other than the one where it was trained. For this, the best performing model C is applied and validated on different TanDEM-X acquisitions over the Mabounié and Rabi sites. Both sites are characterized by different forest types and forest height distributions and have different topographic characteristics than the Lopé site. The achieved results in form of the volume coherence $|\tilde{\gamma}^{E}_{Vol}(\kappa_z)|$ vs. h_v κ_z plots and the validation plots are shown for the four Mabounié acquisitions (acquisitions 6-9 according to their numbering in Table 2.1) in Figure 2.7 and for the four Rabi acquisitions (acquisitions 10-13 according to their numbering in Table 2.1) in Figure 2.8. The plots are generated using the forest height estimates h_v obtained from the inversion of each of the TanDEM-X acquisitions.

The achieved performance is for all acquisitions on both sites, as expected, inferior to the one achieved in Lopé. Looking on the $|\tilde{\gamma}_{Vol}(\kappa_z)|$ vs. h_v κ_z plots for both sites one sees that the vertical reflectivity profiles "learned" in Lopé are relevant enough to provide a consistent solution space for all Mabounié and Rabi acquisitions. However, comparing the Lopé $|\tilde{\gamma}_{Vol}\tilde{\gamma}^{(}_{Vol}\kappa_z)|$ vs. h_v κ_z plots (see Figure 2.5) it is also clear that only a subset of the "learned" reflectivity profiles are used for the inversion in Mabounié and Rabi. This is most likely because the reflectivity profiles "learned" in Lopé are not optimal to describe the underlying reflectivity in the other two sites due to the different forest structures there. The performance across the whole set of acquisitions (e.g., across the whole range of vertical wavenumbers) for both sites is consistent and widely unbiased with MAE values ranging between 7.80 and 8.73 meters and RMSE values between 9.84 and 11.10 meters in Mabounié and with MAE values ranging between 6.81 and 8.95 meters and RMSE values between 8.70 and 11.34 meters in Rabi, as summarized in Table 2.4.

2.6 CONCLUSION

In this study, a hybrid model combining machine learning with physical modeling was proposed for estimating forest height from single baseline, single polarimetric TanDEM-X interferometric coherence measurements. The integration of physical knowledge with domain expertise through a join architecture was attempted

to improve the performance of the physical model and the interpretability of the machine learning architecture, resulting in an overall improved performance.

The proposed model uses an ML algorithm to predict the underlying vertical reflectivity profile, expressed in terms of the Legendre series expansion, as a function of features such as interferometric volume coherence, vertical wavenumber and terrain slope. The predicted vertical reflectivity profile is then used in a physical relationship to estimate forest height.

Three different versions of such a hybrid model were implemented and applied to TanDEM-X acquisitions. The resulting forest heights were validated against the available reference heights. The emphasis was on assessing the inversion performance as a function of the number and the range of the vertical wavenumbers (e.g., TanDEM-X acquisitions) used in the training phase and the number of Legendre polynomials used to define the reflectivity profiles.

It appears that a certain vertical resolution of the vertical reflectivity profiles, expressed by the larger number of Legendre polynomials used to define them, is required to achieve better inversion performance. On the other hand, a set (e.g., more than one) of acquisitions with significantly different vertical wavenumbers is required to obtain vertical reflectivity profiles that are able to span a unique solution space covering the entire possible data space for a wide range of vertical wavenumbers. The best results in the study were obtained with three TanDEM-X acquisitions, but the important criterion is the difference in their vertical wavenumbers. With this in mind, two acquisitions may be sufficient for achieving acceptable performance. It is worth noting here that the combination of ascending and descending acquisitions in the training dataset appears to be possible.

The advantages of this approach are obvious. First, it allows forest height estimates to be obtained without the full observation space required for a model-based inversion. This is because the ML component seems to be able to establish a relationship between the shape of the vertical reflectivity profile and features such as interferometric volume coherence, the associated vertical wavenumber and the terrain topography. The advantages of the hybrid approach of first predicting a vertical reflectivity profile and then using it to

perform a classical inversion are twofold: it minimizes the number of acquisitions required in the training phase to the few needed to "learn" the vertical reflectivity profile. The relationship between the interferometric volume coherence and the forest height at different vertical wavenumbers does not have to be established separately. It is given by the known vertical reflectivity profile.

The performance of any height estimation algorithm that utilizes interferometric coherence is critically dependent on its capacity to capture the spatial variation of the underlying reflectivity profile. This capability is strongly influenced by the boundary conditions of the inversion problem, such as the available observation space, the quantity and type of ancillary data or prior knowledge, and, importantly, the characteristics of the site where performance is evaluated. Consequently, comparing forest height estimation algorithms that operate under different boundary conditions is challenging. The proposed approach enables forest height estimation from a single TanDEM-X acquisition but, in its most effective implementation, requires three TanDEM-X acquisitions and a set of reference forest height measurements for training to account for the spatial variation in the underlying reflectivity profile.

Of course, the dependence of the vertical reflectivity profile on the different forest conditions is not trivial to be determined by any ML component, as it requires data and knowledge that are commonly not available. This lack of adaptability to the different forest structure conditions is also the main reason for the relatively high RMSE values characterizing the inversion results. This ability to adapt to local forest conditions remains the main advantage of model-based approaches, which - if the required observation space is available - are able to do so independently of the availability of any training datasets.

A

SUPPLEMENTARY MATERIAL

This section provides additional material that complements the published version of Paper 1. It includes extended visualizations of the study site, additional input and reference data, as well as details on the MLP architecture and training hyperparameters used in this work. These were not part of the published article but are added here for completeness and reproducibility.

A.1 VISUALIZATION OF STUDY SITE AND DATA

Figure A.1 shows the geographical extent of the study area. Figure A.2 presents examples of the input features, including TanDEM-X coherence and topographic descriptors. Figure A.3 shows the reference data (LiDAR-derived forest height), representative predictions, and residual maps for Scene No. 4 in Table 2.1. Finally, Figure A.4 presents the mosaicked forest height estimates from the Hybrid AI–InSAR model and the associated error maps for Models A, B, and C.

These visualizations were excluded from the published paper but are included here to support the interpretation of results and to provide a more comprehensive overview.

A.2 MODEL ARCHITECTURE AND HYPERPARAMETERS

Table A.1 specifies the architecture of the multilayer perceptron (MLP) used in this study. Table A.2 reports the training hyperparameters to ensure reproducibility.

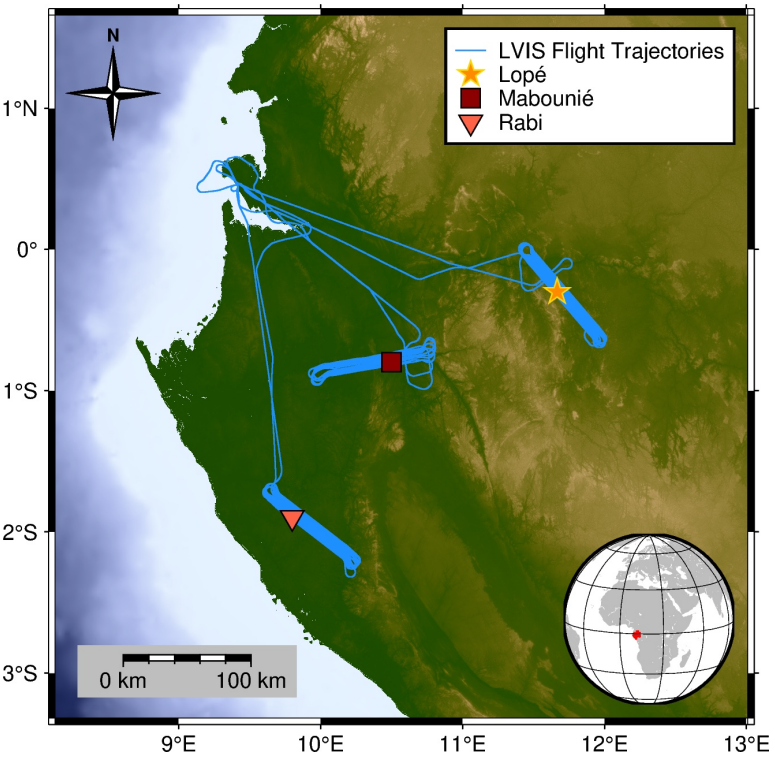

Figure A.1: Study area in Gabon with LVIS flight trajectories (blue) and the three reference sites: Lopé (star), Mabounié (square), and Rabi (triangle). Background shows shaded relief; inset indicates regional location in Central Africa.

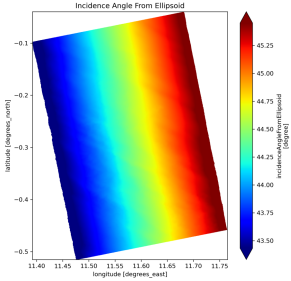

(a) Incidence angle from ellipsoid

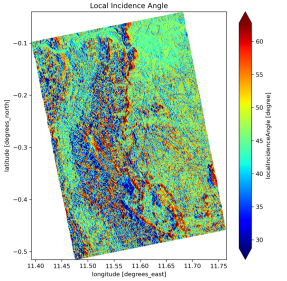

(b) Local incidence angle

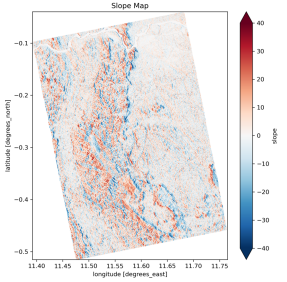

(c) Slope map

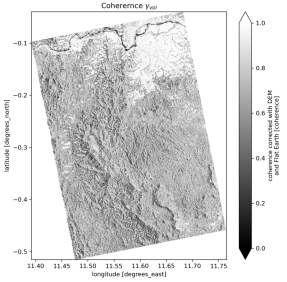

(d) Volume coherence γ_{vol}

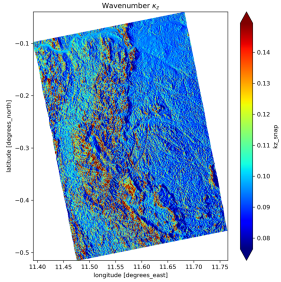

(e) Vertical wavenumber κ_z

Figure A.2: Examples of input features used in the study. The shown example corresponds to Scene No. 4 (site Lopé) in Table 2.1.

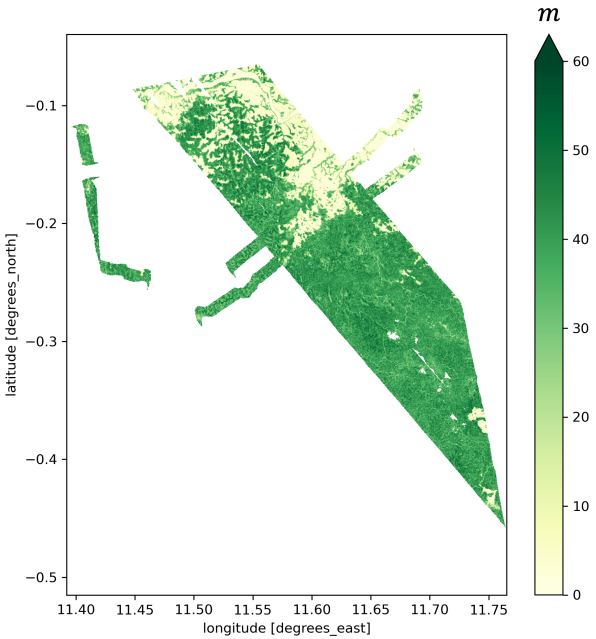

(a) LVIS RH_{98} reference

Figure A.3: Prediction vs. reference (continued 1/3).

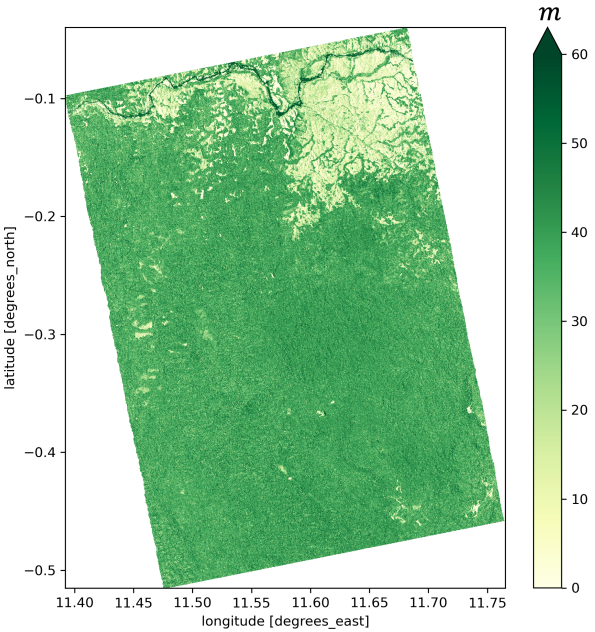

(b) Hybrid AI–InSAR forest height estimate (Model C)

Figure A.3: Prediction vs. reference (continued 2/3).

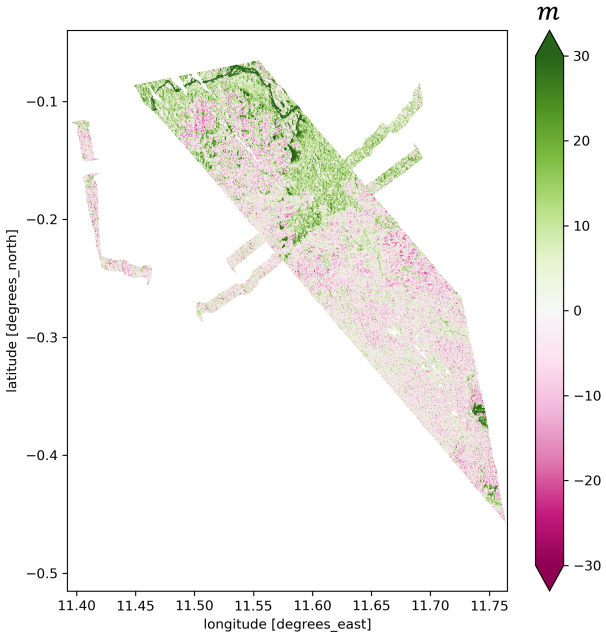

(c) Difference (Model C – LVIS RH_{98})

Figure A.3: Comparison between reference and predicted forest height maps: (a) LVIS RH_{98} reference heights, (b) predicted forest heights from the Hybrid AI–InSAR model (Model C), and (c) difference map (Model C – LVIS RH_{98}). Example corresponds to Scene No. 4 (site Lopé).

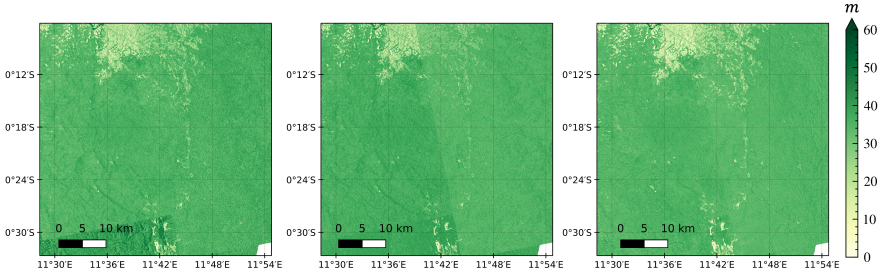

(a) Hybrid AI–InSAR forest height mosaics for Models A, B, and C

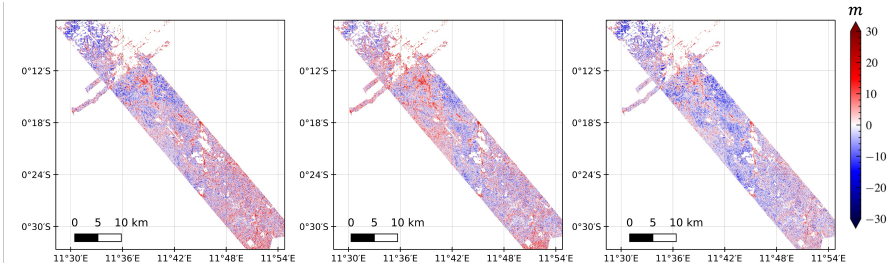

(b) Difference maps (Hybrid AI–InSAR – LVIS RH_{98}) for Models A, B, and C

Figure A.4: Mosaicked forest height estimates (top) from the Hybrid AI–InSAR model and the corresponding error maps (bottom) over Lopé, shown for Models A (left), B (center), and C (right). Errors are computed as the difference between model predictions and LVIS RH_{98} reference data.

Table A.1: Architecture of the MLP used in Paper 1.

Layer	Specification
Input	Number of input features (InSAR + geometry descriptors)
Hidden layer 1	128 neurons, Tanh activation
Hidden layer 2	64 neurons, Tanh activation
Hidden layer 3	32 neurons, Tanh activation
Output	Legendre coefficients / profile parameters

Table A.2: Training hyperparameters of the MLP (Paper 1).

Parameter	Value
Optimizer	Adam
Learning rate	1e-2
Batch size	256
Number of epochs	200
Early stopping	Patience of 20 epochs
Loss function	Mean squared error (MSE)

REFERENCES

[1] H. Pretzsch, "Forest Dynamics, Growth, and Yield," in *Forest Dynamics, Growth and Yield: From Measurement to Model*, H. Pretzsch, Ed., Berlin, Heidelberg: Springer, 2009, 1. DOI: 10.1007/978-3-540-88307-4_1 (cited on page 43).

[2] P. Köhler and A. Huth, "Towards ground-truthing of space-borne estimates of above-ground life biomass and leaf area index in tropical rain forests," *Biogeosciences*, vol. 7, no. 8, 2531, 2010. DOI: 10.5194/bg-7-2531-2010 (cited on page 43).

[3] M. Pause, C. Schweitzer, M. Rosenthal, V. Keuck, J. Bumberger, P. Dietrich, M. Heurich, A. Jung, and A. Lausch, "In Situ/Remote Sensing Integration to Assess Forest Health—A Review," *Remote Sensing*, vol. 8, no. 6, 471, 2016. DOI: 10.3390/rs8060471 (cited on page 43).

[4] B. S. Hardiman, G. Bohrer, C. M. Gough, C. S. Vogel, and P. S. Curtis, "The role of canopy structural complexity in wood net primary production of a maturing northern deciduous forest," *Ecology*, vol. 92, no. 9, 1818, 2011. DOI: 10/cn3zdc (cited on page 43).

[5] G. Berndes, B. Abt, A. Asikainen, A. Cowie, V. Dale, G. Egnell, M. Lindner, L. Marelli, D. Paré, K. Pingoud, and S. Yeh, "Forest biomass, carbon neutrality and climate change mitigation," European Forest Institute, From Science to Policy, 2016. DOI: 10.36333/fs03 (cited on page 43).

[6] J. Praks, F. Kugler, K. P. Papathanassiou, I. Hajnsek, and M. Hallikainen, "Height Estimation of Boreal Forest: Interferometric Model-Based Inversion at L- and X-Band Versus HUTSCAT Profiling Scatterometer," *IEEE Geoscience and Remote Sensing Letters*, vol. 4, no. 3, 466, 2007. DOI: 10.1109/LGRS.2007.898083 (cited on page 43).

[7] F. Garestier, P. C. Dubois-Fernandez, and I. Champion, "Forest Height Inversion Using High-Resolution P-Band Pol-InSAR Data," *IEEE Transactions on Geoscience and Remote Sensing*, vol. 46, no. 11, 3544, 2008. DOI: 10.1109/TGRS.2008.922032 (cited on page 43).

[8] F. Garestier, P. C. Dubois-Fernandez, and K. P. Papathanassiou, "Pine Forest Height Inversion Using Single-Pass X-Band PolInSAR Data," *IEEE Transactions on Geoscience and Remote Sensing*, vol. 46, no. 1, 59, 2008. DOI: 10.1109/TGRS.2007.907602 (cited on page 43).

[9] I. Hajnsek, F. Kugler, S.-K. Lee, and K. P. Papathanassiou, "Tropical-Forest-Parameter Estimation by Means of Pol-InSAR: The INDREX-II Campaign," *IEEE Transactions on Geoscience and Remote Sensing*, vol. 47, no. 2, 481, 2009. DOI: 10.1109/TGRS.2008.2009437 (cited on page 43).

[10] F. Kugler, Seung-Kuk Lee, I. Hajnsek, and K. P. Papathanassiou, "Forest Height Estimation by Means of Pol-InSAR Data Inversion: The Role of the Vertical Wavenumber," *IEEE Transactions on Geoscience and Remote Sensing*, vol. 53, no. 10, 5294, 2015. DOI: 10.1109/TGRS.2015.2420996 (cited on pages 43, 46, 51).

[11] R. Guliaev, V. Cazcarra-Bes, M. Pardini, and K. Papathanassiou, "Forest Height Estimation by Means of TanDEM-X InSAR and Waveform Lidar Data," *IEEE Journal of Selected Topics in Applied Earth Observations and Remote Sensing*, vol. 14, 3084, 2021. DOI: 10.1109/JSTARS.2021.3058837 (cited on page 43).

[12] C. Choi, V. Cazcarra-Bes, R. Guliaev, M. Pardini, K. P. Papathanassiou, W. Qi, J. Armston, and R. O. Dubayah, "Large-Scale Forest Height Mapping by Combining TanDEM-X and GEDI Data," *IEEE Journal of Selected Topics in Applied Earth Observations and Remote Sensing*, vol. 16, 2374, 2023. DOI: 10.1109/JSTARS.2023.3244866 (cited on page 43).

[13] Q. Zhang, L. Ge, S. Hensley, G. Isabel Metternicht, C. Liu, and R. Zhang, "PolGAN: A deep-learning-based unsupervised forest height estimation based on the synergy of PolInSAR and LiDAR data," *ISPRS Journal of Photogrammetry and Remote Sensing*, vol. 186, 123, 2022. DOI: 10.1016/j.isprsjprs.2022.02.008 (cited on page 44).

[14] Y. Zhang, X. Peng, Q. Xie, Y. Du, B. Zhang, X. Luo, S. Zhao, Z. Hu, and X. Li, "Forest height estimation combining single-polarization tomographic and PolSAR data," *International Journal of Applied Earth Observation and Geoinformation*, vol. 124, 103532, 2023. DOI: 10.1016/j.jag.2023.103532 (cited on page 44).

[15] W. Yang, S. Vitale, H. Aghababaei, G. Ferraioli, V. Pascazio, and G. Schirinzi, "A Deep Learning Solution for Height Estimation on a Forested Area Based on Pol-TomoSAR Data," *IEEE Transactions on Geoscience and Remote Sensing*, vol. 61, 1, 2023. DOI: 10.1109/TGRS.2023.3274395 (cited on page 44).

[16] L. Wang, J. Yang, L. Shi, P. Li, L. Zhao, and S. Deng, "Impact of Backscatter in Pol-InSAR Forest Height Retrieval Based on the Multimodel Random Forest Algorithm," *IEEE Geoscience and Remote Sensing Letters*, vol. 17, no. 2, 267, 2020. DOI: 10.1109/LGRS.2019.2919449 (cited on page 44).

[17] W. Yang, S. Vitale, H. Aghababaei, G. Ferraioli, V. Pascazio, and G. Schirinzi, "A Deep Learning Solution for Height Inversion on Forested Areas Using Single and Dual Polarimetric TomoSAR," *IEEE Geoscience and Remote Sensing Letters*, vol. 20, 1, 2023. DOI: 10.1109/LGRS.2023.3322782 (cited on page 44).

[18] C. Xing, H. Wang, Z. Zhang, J. Yin, and J. Yang, "A Review of Forest Height Inversion by PolInSAR: Theory, Advances, and Perspectives," *Remote Sensing*, vol. 15, no. 15, 3781, 2023. DOI: 10.3390/rs15153781 (cited on page 44).

[19] G. Brigot, M. Simard, E. Colin-Koeniguer, and A. Boulch, "Retrieval of Forest Vertical Structure from PolInSAR Data by Machine Learning Using LIDAR-Derived Features," *Remote Sensing*, vol. 11, no. 4, 381, 2019. DOI: 10.3390/rs11040381 (cited on page 44).

[20] J.-L. Bueso-Bello, D. Carcereri, M. Martone, C. González, P. Posovszky, and P. Rizzoli, "Deep Learning for Mapping Tropical Forests with TanDEM-X Bistatic InSAR Data," *Remote Sensing*, vol. 14, no. 16, 3981, 2022. DOI: 10.3390/rs14163981 (cited on page 44).

[21] D. Carcereri, P. Rizzoli, D. Ienco, and L. Bruzzone, "A Deep Learning Framework for the Estimation of Forest Height From Bistatic TanDEM-X Data," *IEEE Journal of Selected Topics in Applied Earth Observations and Remote Sensing*, vol. 16, 8334, 2023. DOI: 10.1109/JSTARS.2023.3310209 (cited on page 44).

[22] X. Wang and H. Wang, "Forest Height Mapping Using Complex-Valued Convolutional Neural Network," *IEEE Access*, vol. 7, 126334, 2019. DOI: 10.1109/ACCESS.2019.2938896 (cited on page 44).

[23] H. Luo, C. Yue, F. Xie, B. Zhu, and S. Chen, "A Method for Forest Canopy Height Inversion Based on Machine Learning and Feature Mining Using UAVSAR," *Remote Sensing*, vol. 14, no. 22, 5849, 2022. DOI: 10.3390/rs14225849 (cited on page 44).

[24] H. Luo, C. Yue, H. Yuan, N. Wang, and S. Chen, "A Method for Forest Canopy Height Inversion Based on UAVSAR and Fourier–Legendre Polynomial—Performance in Different Forest Types," *Drones*, vol. 7, no. 3, 152, 2023. DOI: 10.3390/drones7030152 (cited on page 44).

[25] X. Sun, B. Wang, M. Xiang, L. Zhou, S. Wang, and S. Jiang, "Machine-Learning Inversion of Forest Vertical Structure Based on 2-D-SGVBVoG Model for P-Band Pol-InSAR," *IEEE Transactions on Geoscience and Remote Sensing*, vol. 60, 1, 2022. DOI: 10.1109/TGRS.2021.3091541 (cited on page 44).

[26] G. E. Karniadakis, I. G. Kevrekidis, L. Lu, P. Perdikaris, S. Wang, and L. Yang, "Physics-informed machine learning," *Nature Reviews Physics*, vol. 3, no. 6, 422, 2021. DOI: 10.1038/s42254-021-00314-5 (cited on page 44).

[27] J. Armston, H. Tang, S. Hancock, S. Marselis, L. Duncanson, J. Kellner, M. Hofton, J. B. Blair, T. Fatoyinbo, and R. O. Dubayah, *AfriSAR: Gridded Forest Biomass and Canopy Metrics Derived from LVIS, Gabon, 2016*, 2020 (cited on page 45).

[28] T. Fatoyinbo, J. Armston, M. Simard, S. Saatchi, M. Denbina, M. Lavalle, M. Hofton, H. Tang, S. Marselis, N. Pinto, S. Hancock, B. Hawkins, L. Duncanson, B. Blair, C. Hansen, Y. Lou, R. Dubayah, S. Hensley, C. Silva, J. R. Poulsen, N. Labrière, N. Barbier, K. Jeffery, D. Kenfack, M. Herve, P. Bissiengou,

A. Alonso, G. Moussavou, L. T. White, S. Lewis, and K. Hibbard, "The NASA AfriSAR campaign: Airborne SAR and lidar measurements of tropical forest structure and biomass in support of current and future space missions," *Remote Sensing of Environment*, vol. 264, 112533, 2021. DOI: 10/gk7vts (cited on page 45).

[29] P. Rosen, S. Hensley, I. Joughin, F. Li, S. Madsen, E. Rodriguez, and R. Goldstein, "Synthetic aperture radar interferometry," *Proceedings of the IEEE*, vol. 88, no. 3, 333, 2000. DOI: 10.1109/5.838084 (cited on page 45).

[30] S. Cloude, *Polarisation: Applications in Remote Sensing*. Oxford University Press, 2009. DOI: 10.1093/acprof:oso/9780199569731.001.0001 (cited on pages 45, 47, 48).

[31] M. Denbina, M. Simard, and B. Hawkins, "Forest Height Estimation Using Multibaseline PolInSAR and Sparse Lidar Data Fusion," *IEEE Journal of Selected Topics in Applied Earth Observations and Remote Sensing*, vol. 11, no. 10, 3415, 2018. DOI: 10.1109/JSTARS.2018.2841388 (cited on page 46).

[32] J. Askne, P. Dammert, L. Ulander, and G. Smith, "C-band repeat-pass interferometric SAR observations of the forest," *IEEE Transactions on Geoscience and Remote Sensing*, vol. 35, no. 1, 25, 1997. DOI: 10.1109/36.551931 (cited on page 46).

[33] H. Zebker and J. Villasenor, "Decorrelation in interferometric radar echoes," *IEEE Transactions on Geoscience and Remote Sensing*, vol. 30, no. 5, 950, 1992. DOI: 10.1109/36.175330 (cited on page 46).

[34] J. O. Hagberg, L. M. Ulander, and J. Askne, "Repeat-pass SAR interferometry over forested terrain," *IEEE Transactions on Geoscience and Remote Sensing*, vol. 33, no. 2, 331, 1995. DOI: 10.1109/TGRS.1995.8746014 (cited on page 46).

[35] R. Bamler and P. Hartl, "Synthetic aperture radar interferometry," *Inverse Problems*, vol. 14, no. 4, R1, 1998. DOI: 10.1088/0266-5611/14/4/001 (cited on page 46).

[36] F. Kugler, D. Schulze, I. Hajnsek, H. Pretzsch, and K. P. Papathanassiou, "TanDEM-X Pol-InSAR Performance for Forest Height Estimation," *IEEE Transactions on Geoscience and Remote Sensing*, vol. 52, no. 10, 6404, 2014. DOI: 10.1109/TGRS.2013.2296533 (cited on page 47).

[37] M. Martone, B. Bräutigam, P. Rizzoli, C. Gonzalez, M. Bachmann, and G. Krieger, "Coherence evaluation of TanDEM-X interferometric data," *ISPRS Journal of Photogrammetry and Remote Sensing*, Innovative Applications of SAR Interferometry from modern Satellite Sensors, vol. 73, 21, 2012. DOI: 10.1016/j.isprsjprs.2012.06.006 (cited on page 47).

[38] R. N. Treuhaft and P. R. Siqueira, "Vertical structure of vegetated land surfaces from interferometric and polarimetric radar," *Radio Science*, vol. 35, no. 1, 141, 2000. DOI: 10.1029/1999RS900108 (cited on page 47).

[39] A. Roueff, A. Arnaubec, P. C. Dubois-Fernandez, and P. Refregier, "Cramer–Rao Lower Bound Analysis of Vegetation Height Estimation With Random Volume Over Ground Model and Polarimetric SAR Interferometry," *IEEE Geoscience and Remote Sensing Letters*, vol. 8, no. 6, 1115, 2011. DOI: 10.1109/LGRS.2011.2157891 (cited on page 47).

[40] S. R. Cloude, "Polarization coherence tomography," *Radio Science*, vol. 41, no. 4, 2006. DOI: 10.1029/2005RS003436 (cited on page 48).

[41] S. R. Cloude, "Dual-Baseline Coherence Tomography," *IEEE Geoscience and Remote Sensing Letters*, vol. 4, no. 1, 127, 2007. DOI: 10.1109/LGRS.2006.885893 (cited on page 48).

[42] M. Brolly, M. Simard, H. Tang, R. O. Dubayah, and J. P. Fisk, "A Lidar-Radar Framework to Assess the Impact of Vertical Forest Structure on Interferometric Coherence," *IEEE Journal of Selected Topics in Applied Earth Observations and Remote Sensing*, vol. 9, no. 12, 5830, 2016. DOI: 10.1109/JSTARS.2016.2527360 (cited on page 48).

[43] F. Chollet, *Deep Learning with Python*, Second. Manning, 2021 (cited on page 50).

3

HYBRID MACHINE LEARNING MODEL FOR FOREST HEIGHT ESTIMATION FROM TANDEM-X AND LANDSAT DATA

Islam Mansour[1,2], Konstantinos Papathanassiou[1], Ronny Hänsch[1], and Irena Hajnsek[1,2]

1 Microwaves and Radar Institute, German Aerospace Center DLR, Germany
2 Institute of Environmental Engineering, ETH Zurich, Switzerland

Article submitted for publication in *IEEE Geoscience and Remote Sensing Letters*

Key findings:

- Integrated Landsat spectral data as input to the hybrid model to improve forest height predictions.
- Achieved 13.5% reduction in RMSE and 16.6% reduction in MAE compared to previous models
- Enhanced performance over complex terrain and varying forest structures.

Author's contributions:

- Processed the dataset from TanDEM-X acquisitions.
- Developed the novel hybrid modeling methodology.
- Performed data analysis and validation.

Co-author's contributions:

- K. Papathanassiou: Provided guidance and expertise on the physical model development and underlying radar remote sensing principles and the idea of using Landsat multi-spectral bands.
- R. Hänsch: Provided guidance and expertise on the machine learning component development and its optimization.
- I. Hajnsek: Provided supervision and guidance on overall research direction.
- All co-authors collectively contributed to the method development, result discussion, and manuscript revision.

This chapter is a pre-print of the above-listed manuscript, differing from the submitted version only in terms of layout, formatting, and citation style.

Abstract

The integration of machine learning (ML) with physical models (PM) has emerged as a promising approach for retrieving geophysical parameters from remote sensing data. Such hybrid approaches have the potential to overcome key limitations of ML such as scarceness of training data and interpretability, and to improve the performance of traditional PM, especially in cases where they are under-determined. Recently, such a hybrid model has been proposed for forest height estimation using single-baseline, single-polarization TanDEM-X interferometric coherence measurements. To ensure maximum support of the PM structure on the ML component, the (input) features used for training and inversion are all related to the parameterization of the PM. However, this limits the feature space and, thus, the potential of the ML component to explore multi-parameter data spaces by establishing non-apparent relationships and patterns. This study investigates the extension of the input space by including multispectral Landsat data, which per se cannot be physically related to other features or forest height through a physical model. The extent to which this approach can improve performance by compensating for some of the deficiencies of the original hybrid model is analyzed and discussed. The developed model is applied and validated on several TanDEM-X acquisitions over tropical sites with different acquisition geometries. Its performance is assessed against reference data derived from airborne LiDAR measurements.

Keywords

InSAR, forest height estimation, interferometry, synthetic aperture radar, TanDEM-X, ESA Biomass, Landsat, multimodal, remote sensing, forest height, forest structure, temporal decorrelation, topographic effects, machine learning, hybrid modeling, physical modeling.

3.1 INTRODUCTION

Polarimetric SAR Interferometry, i.e., interferometric measurements with polarimetric and spatial baseline diversity, is an established remote sensing technique for obtaining continuous forest height estimates of significant accuracy at large spatial scales [1], [2], [3]. The inversion approaches are usually model-based, exploring the physical relationship connecting interferometric measurements to the 3D distribution of scatterers within forests. The achieved performance critically depends on the parameterization of the inversion problems. Accurate and generic parameterization requires an adequate observation space to achieve a balanced inversion problem. Simplified or constrained model parameterizations without sufficient observation space result in compromised inversion performances.

Machine learning (ML) inversion approaches have become increasingly popular in recent years as an alternative to parameter estimation from RS data, exploring the potential of ML to identify patterns and correlations in a complex, multidimensional space, even when explicit (physical) relationships are not available. ML allows combining different data types into a single framework, including SAR-derived interferometric coherence and optical or LiDAR remote sensing data for forest height estimation [4], [5], [6]. However, despite their unquestioned potential, current ML models for forest height estimation often suffer from limited interpretability and generalization.

One way to overcome these limitations is hybrid modeling approaches that integrate ML and physical models [7]. They combine the power and effectiveness of data-based approaches with physical models' plausibility, interpretability, and generalizability. In this context, a recently published study established a hybrid inversion framework combining ML and physical modeling components to estimate forest height from single-baseline, single-polarimetric TanDEM-X interferometric coherence [7].

In the proposed model, the vertical reflectivity profile is represented using a Legendre series expansion, with its coefficients predicted as a function of input features via a MLP. These input features include interferometric volume coherence, terrain-corrected vertical wavenumber, incidence angle, and terrain slope in the

range direction. The resulting vertical reflectivity profile is then used within a physical model to estimate forest height.

It should be noted that while this study adopts a relatively simple MLP architecture, the hybrid framework is not restricted to this choice. Other deep learning models — such as convolutional neural networks (CNNs) or transformer-based architectures with attention mechanisms—could also be considered to capture additional spatial dependencies and complex feature interactions. An MLP was chosen for its interpretability, efficiency, and suitability for multimodal integration, but future research may explore more advanced architectures.

The advantages of this approach are twofold. First, it enables forest height estimation—even in the absence of the full observation space required for a traditional model-based inversion—by allowing the MLP to infer the shape of the reflectivity profile from limited input features. Second, it reduces the number of required acquisitions by leveraging physical constraints to generalize across vertical wavenumbers, even when trained on a limited subset.

The critical point of the approach is the ability of the ML component to determine, with the available input features, the vertical reflectivity profile for different forest and terrain (e.g., slope) conditions. The set of input features used for training and inversion in [7] consists exclusively of radar and geometry parameters to support the PM structure on the ML component. While this is important, this set of input features does not provide any information about the underlying forest type. This limits the ability of the ML model to adapt the vertical reflectivity profile to the different forest structure types, and is the main reason for the relatively high RMSE values that characterize the achieved inversion performance.

This study attempts to address this limitation and aims to improve the prediction of the vertical reflectivity profile by extending the feature space to include multispectral Landsat data that provide information on forest type stratification/canopy closure that cannot be linked per se to the other input features or to PM parameters due to the lack of established physical relationships.

3.2 METHODOLOGY

The measured interferometric coherence $\tilde{\gamma}_{obs}(\kappa_z)$ can be expressed as [8], [9], [10], [11]:

$$\tilde{\gamma}_{obs}(\kappa_z) = \tilde{\gamma}_{Tmp}\tilde{\gamma}_{Rg}\tilde{\gamma}_{Sys}\tilde{\gamma}_{\mathrm{Vol}}(\kappa_z) \tag{3.1}$$

where $\tilde{\gamma}_{\mathrm{Vol}}(\kappa_z)$ accounts for volume decorrelation related to the forest canopy, while $\tilde{\gamma}_{Tmp}$, $\tilde{\gamma}_{Rg}$, $\tilde{\gamma}_{Sys}$ represent temporal, range, and system decorrelations, respectively [12]. The volume decorrelation is defined as [13], [14]:

$$\tilde{\gamma}_{\mathrm{Vol}}(\kappa_z) = e^{i\kappa_z z_o}\frac{\int_0^{h_v} f(z)\, e^{i\kappa_z z} dz}{\int_0^{h_v} f(z)\, dz} \tag{3.2}$$

where the vertical reflectivity profile $f(z)$ represents the vertical distribution of scattering elements and h_v is the forest height. The vertical wavenumber (in rad/m), κ_z, expresses the sensitivity of the interferometric phase to height changes [15]:

$$\kappa_z = m\frac{2\pi}{\lambda}\frac{\Delta\theta}{\sin(\theta_0 + \alpha)} \tag{3.3}$$

where θ_0 is the radar look angle, $\Delta\theta$ the look angle difference induced by the spatial baseline, λ the wavelength, and α the ground range terrain slope. When $f(z)$ is known, Eq. 3.2 is reduced to a balanced and unique inversion problem, allowing the forest height estimation.

In order to obtain an estimate for the vertical reflectivity profile, $f(z)$ is first expressed in terms of a polynomial series expansion using the Legendre polynomials $P_n(z)$ as [16], [17]:

$$f(z, \mathrm{a}_n) = \sum_{n=1}^{N} \mathrm{a}_n P_n(z) \tag{3.4}$$

where a_n are the associated coefficients, and N is the number of terms in the expansion truncated to a relatively small number. After this, an ML algorithm is used to predict the underlying vertical

reflectivity profile $f(z, a_n)$ expressed in terms of the Legendre series expansion (see eq. (3.4)) as a function of a set of input features. The predicted vertical reflectivity profile $f(z, a_n)$ is then used in eq. (3.2) to estimate forest height. Figure 3.1 shows a conceptual representation of the architecture and functionality of the proposed hybrid model in training and inference.

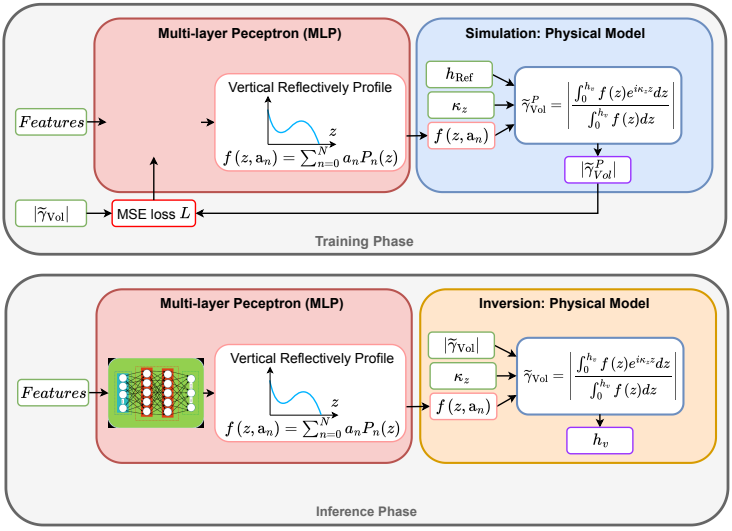

Figure 3.1: Conceptual architecture and functionality of the hybrid model in the training (top) and inference phase (bottom).

The model with the best performance in [7] uses seven Legendre polynomials ($N = 7$) to define the vertical reflectivity profiles and three TanDEM-X acquisitions (two ascending and one descending) for training. The input features include the interferometric volume coherence $\tilde{\gamma}_{\mathrm{Vol}}(\kappa_z)$, the terrain corrected vertical wavenumber κ_z, the incidence angle θ_0 , and the terrain slope in the range direction α. This configuration is referred to as *Model-C*. To improve its performance, the input feature space are extended by incorporating four Landsat spectral bands: Band 4 (Red, 0.630–0.680 μm), Band 5 (Near-Infrared [NIR], 0.845–0.885 μm), and Bands 6 and 7 corresponding to Short-Wave Infrared 1 (SWIR1, 1.560–1.660 μm) and Short-Wave Infrared 2 (SWIR2, 2.100–2.300 μm), respectively. This extended configuration is referred to as *Model-D*.

Table 3.1: Models and associated number of Legendre Coef. and TanDEM-X acquisition(s) and HoA used for training (as shown in Figure 3.1, top).

Model	Coef.	HoA (m)	ML Input Features	PM Inputs
C	7	52.45 (No 1 in Table 3.2) -65.22 (No 2 in Table 3.2) 95.41 (No 5 in Table 3.2)	κ_z, $\lvert\widetilde{\gamma}_{\mathrm{Vol}}(\kappa_z)\rvert$, θ, θ_{loc}, α	h_{Ref}, κ_z, $f(z, \mathrm{a}_n)$
D	7	52.45 (No 1 in Table 3.2) -65.22 (No 2 in Table 3.2) 95.41 (No 5 in Table 3.2)	κ_z, $\lvert\widetilde{\gamma}_{\mathrm{Vol}}(\kappa_z)\rvert$, θ, θ_{loc}, α, Red, NIR, $SWIR1$, $SWIR2$	h_{Ref}, κ_z, $f(z, \mathrm{a}_n)$

Table 3.2: TanDEM-X Datasets, Sites, Scene ID's, Height of Ambiguity [m] (HoA), Nominal incidence angle [°]. The HoA sign indicates the orbit direction: positive for ascending, negative for descending orbit.

No	Site	Scene ID	HoA	θ_0
1	Lopé	TDM1_SAR__COS_BIST_SM_S_SRA_20190610T173107_20190610T173115	52.45	46.18
2	Lopé	TDM1_SAR__COS_BIST_SM_S_SRA_20160125T173041_20160125T173048	-65.22	44.44
3	Lopé	TDM1_SAR__COS_BIST_SM_S_SRA_20111002T045625_20111002T045633	86.34	46.08
4	Lopé	TDM1_SAR__COS_BIST_SM_S_SRA_20121226T045626_20121226T045634	94.89	45.10
5	Lopé	TDM1_SAR__COS_BIST_SM_S_SRA_20121215T045627_20121215T045635	95.41	46.68

To ensure consistency and comparability with *Model-C*, the same basic setup is retained for *Model-D*, including preprocessing steps, dataset split ratios, and optimization settings, as described in [7]. Moreover, the same training strategy used for *Model-C* is applied to *Model-D*. The models, their input features, and configurations are summarized in Table 3.1. The only difference lies in including the four Landsat spectral bands in the input feature space.

3.3 STUDY AREA AND DATASET

This study focuses on the Lopé site within the homonymous National Park in Gabon. The area comprises savannah and subtropical forest stands with diverse species composition and density. Tree heights exceed 50 m in many locations. The terrain is hilly, with local slopes steeper than 20°.

The set of TanDEM-X images used is summarized in Table 3.2. From the TanDEM-X CoSSC products, and following standard preprocessing steps, the volume decorrelation $|\tilde{\gamma}_{\mathrm{Vol}}(\kappa_z)|$, the terrain corrected vertical wavenumber κ_z, and the local incidence angle θ_0 are derived. Terrain correction is performed using the 30 m Copernicus DEM [18].

Four Landsat spectral bands (Red, NIR, SWIR1, and SWIR2) from Hansen's cloud-free product [19] are included as additional input features.

Reference forest height data are derived from full-waveform LiDAR collected by NASA's LVIS sensor during the AfriSAR 2016 campaign [20]. The RH98 metric, representing the 98th percentile height, is used as the reference forest height ($h_{\mathrm{Ref}} = RH98$). All datasets are resampled and georeferenced to a standard spatial resolution of 20 m × 20 m.

3.4 IMPLEMENTATION AND RESULTS

Both models are trained using the same three TanDEM-X acquisitions—two ascending and one descending—corresponding to scenes 1, 2, and 5 in Table 3.2, each characterized by a different vertical wavenumber. The available training data space is illustrated in the left panel of Figure 3.2, where the observed volume coherence magnitudes $|\tilde{\gamma}_{\mathrm{Vol}}(\kappa_z)|$ from the three acquisitions are plotted

against the product $h_{\text{Ref}} \cdot \kappa_z$, with h_{Ref} representing the reference forest height and κ_z the terrain-corrected vertical wavenumber.

During training, an initial vertical reflectivity profile $f(z, \mathrm{a}_n)$, represented via its Legendre coefficients a_n, is used in conjunction with h_{Ref} and κ_z in Eq. 3.2 to predict the volume decorrelation $|\tilde{\gamma}^{P}_{\text{Vol}}(\kappa_z)|$. This predicted value is then compared to the observed volume coherence $|\tilde{\gamma}_{\text{Vol}}(\kappa_z)|$, and the coefficients a_n are iteratively updated to minimize the difference. The coefficients are estimated by a MLP that learns the mapping between the input features and the reflectivity profile.

Once trained, the model predicts forest height in two steps. First, the input features are used to infer the vertical reflectivity profile $f(z, \mathrm{a}_n)$. Then, this profile is employed in Eq. 3.2 to estimate forest height from the observed $|\tilde{\gamma}_{\text{Vol}}(\kappa_z)|$.

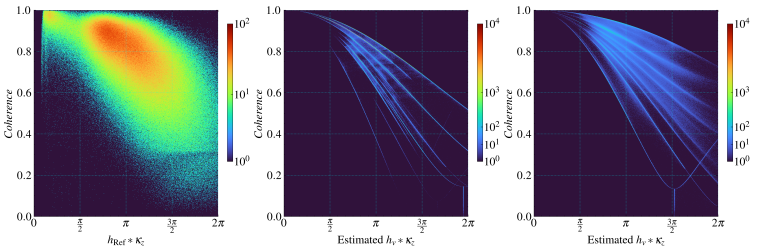

Figure 3.2: $|\tilde{\gamma}_{\text{Vol}}(\kappa_z)|$ vs. $\kappa_z \cdot h_{\text{Ref}}$ or $\kappa_z \cdot h_v$ product. (Left) The volume coherence $|\tilde{\gamma}_{\text{Vol}}(\kappa_z)|$ is plotted against $h_{\text{Ref}} \cdot \kappa_z$ for the entire data space available during training. (Center, Right) The volume coherence $|\tilde{\gamma}_{\text{Vol}}(\kappa_z)|$ are shown against $h_v \cdot \kappa_z$ retrieved from all five TanDEM-X acquisitions using *Model-C* (center) and *Model-D* (right). The colors indicate the relative number of samples and go from dark blue (low) to dark red (high).

The resulting solution spaces from the "learned" vertical reflectivity profiles for both models are shown in the middle and right panels of Figure 3.2. In these plots, $|\tilde{\gamma}_{\text{Vol}}(\kappa_z)||$ is shown against the product $h_v \cdot \kappa_z$, where h_v denotes the inverted forest height. Each profile $f(z, \mathrm{a}_n)$ defines a unique curve in the $|\tilde{\gamma}_{\text{Vol}}(\kappa_z)|$ versus $\kappa_z \cdot h_{\text{Ref}}$ plane according to Eq. 3.2.

A comparison with the training data space (left panel) reveals that *Model-D* provides a broader and more effective coverage of the data space, particularly in regions with high κ_z h_{Ref} values and strong volume coherence. This indicates *Model-D*'s improved

capacity to handle diverse canopy structures and a wider range of vertical wavenumbers.

3.4.1 *Overall Performance*

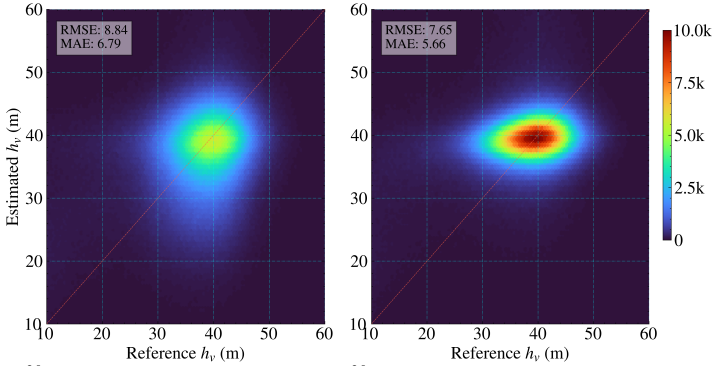

Figure 3.3: Estimated h_v vs. Reference h_v forest height (left model C and right model D). The plot is generated using the Lopé forest height estimates h_v obtained from the inversion of each of all five TanDEM-X acquisitions. The colors indicate the relative number of samples and go from dark blue (low) to dark red (high).

Figure 3.3 presents the validation plots, where the estimated forest heights h_v from all five TanDEM-X acquisitions are plotted against the reference heights h_{Ref}. Results are shown for *Model-C* (left) and *Model-D* (right). Performance is quantified using the mean absolute error (MAE) and root mean square error (RMSE). *Model-D* demonstrates clear improvements over *Model-C*. The slight underestimation observed in *Model-C* is largely corrected in *Model-D*, attributed to its enhanced ability to generate reflectivity profiles that better span the subspace of high $\kappa_z \cdot h_{\text{Ref}}$ and strong volume coherence $|\tilde{\gamma}_{\text{Vol}}(\kappa_z)|$.

The RMSE decreased from **8.84 m** in *Model-C* to **7.65 m** in *Model-D*, and the MAE improved from **6.79 m** to **5.66 m**. Table 3.3 summarizes the performance metrics across individual scenes, showing that *Model-D* consistently outperforms *Model-C*. These improvements correspond to a **13.5% reduction in RMSE** and a **16.6% reduction in MAE**.

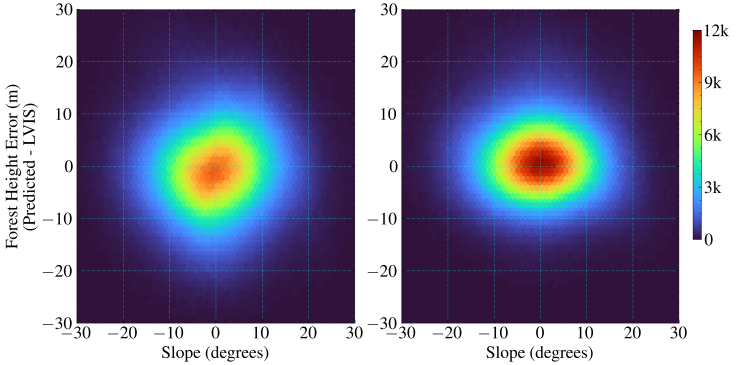

Figure 3.4: Forest Height Error vs. slope (left model C and right model D). The plots are generated using the Lopé forest height estimates h_v obtained from the inversion of each of all five TanDEM-X acquisitions. The colors indicate the relative number of samples and go from dark blue (low) to dark red (high).

3.4.2 *Performance on Terrain Slopes*

The influence of terrain slope on model performance is analyzed next. Figure 3.4 shows the residual errors (differences between estimated and reference heights) for both models across the range of terrain slopes. *Model-C* tends to underestimate forest height at negative range slopes—those facing away from the radar—while *Model-D* shows minimal sensitivity to slope variation.

Both models exhibit increased error variability on steeper slopes, particularly beyond $\pm 20°$, yet *Model-D* maintains lower residuals throughout. Integrating Landsat spectral bands in *Model-D* provides complementary information that helps resolve ambiguities arising from terrain slope and acquisition geometry. For mild slopes between $-10°$ and $+10°$, *Model-D* achieves near-zero bias and symmetrical residuals.

Table 3.3: RMSE and MAE Results for Models C and D Across Different Scenes.

Scene No	Model C		Model D	
	RMSE [m]	MAE [m]	RMSE [m]	MAE [m]
1	8.09	6.28	7.26	5.42
2	9.09	6.93	9.09	5.71
3	8.34	6.41	7.52	5.51
4	8.97	6.98	6.94	5.25
5	9.62	7.32	8.93	6.55
Overall	8.84	6.79	7.65	5.66

These results highlight the strength of the hybrid framework: the machine learning component effectively learns a mapping between the spectral features and the vertical reflectivity profile, compensating for underestimation in negatively sloped terrain. As a result, *Model-D* exhibits enhanced generalization capabilities across complex topographic conditions.

3.5 CONCLUSIONS

This study presents an extension of an established hybrid model for forest height estimation using single-baseline, single-polarization TanDEM-X interferometric coherence measurements. To enhance the model's adaptability to varying forest structures and terrain conditions (e.g., slopes), the input feature space is expanded by incorporating four Landsat spectral bands. The integration of Landsat spectral information significantly improved overall performance, reducing the RMSE and MAE by 13.5% and 16.6%, respectively. Furthermore, it enhances performance over complex terrain by mitigating ambiguities related to terrain slopes, acquisition geometries, and forest structural variation. The bias is largely compensated for gentle range slopes between $-15°$ and $+15°$.

The incorporation of multimodal data is critical in overcoming the limitations of single-source approaches. The machine learning component enables the effective use of Landsat features by learning

relationships that cannot be explicitly modeled by the physical component due to the absence of established physical relationships.

3.6 ACKNOWLEDGMENT

The authors would like to thank NASA Goddard Space Flight Center and the University of Maryland, College Park for providing canopy metrics derived from the Land, Vegetation, and Ice Sensor (LVIS). The authors would also like to thank the German Aerospace Center (DLR) and the Leibniz Supercomputing Centre (LRZ) for the computational and data resources provided by their joint High Performance Data Analysis (HPDA) project "terrabyte". This work was funded by the DeepSAR research project of the Helmholtz Association of German Research Centers (HGF).

B

SUPPLEMENTARY MATERIAL

This section provides additional material that complements the published version of the paper. It includes extended visualizations of the study sites, input features, reference data, predictions, and residuals, as well as detailed specifications of the MLP architecture and training hyperparameters.

B.1 VISUALIZATION OF STUDY SITES AND DATA

Figure B.1 shows the four Landsat spectral bands used as additional input features for Model D. The maps correspond to Scene No. 4 from Table 3.2 over Lopé. These bands, which include red, near-infrared, and shortwave infrared wavelengths, provide complementary spectral information that supports the Hybrid AI–InSAR model in capturing forest structural variation.

Figure B.2 summarizes the learned Legendre coefficients using false-color RGB composites: the top panel shows Model C and the bottom panel shows Model D. Each panel displays five RGB triplets $(R : a_k, G : a_{k+1}, B : a_{k+2})$ across the scene to visualize spatial structure of the seven coefficients. Figure B.3 presents the mosaicked forest-height predictions and corresponding residuals with respect to LVIS reference data: the top row shows the predicted forest height mosaic (left: Model C, right: Model D), and the bottom row shows the residual error maps (prediction – LVIS RH_{98}) for the same models.

B.2 MODEL ARCHITECTURE AND HYPERPARAMETERS

For reference, the architecture of Model C corresponds to the setup described in Table A.1 from Paper 1. In contrast, the architecture of Model D is detailed below in Table B.1. Its training hyperparameters, shown in Table B.2, are identical to those used in Paper 1.

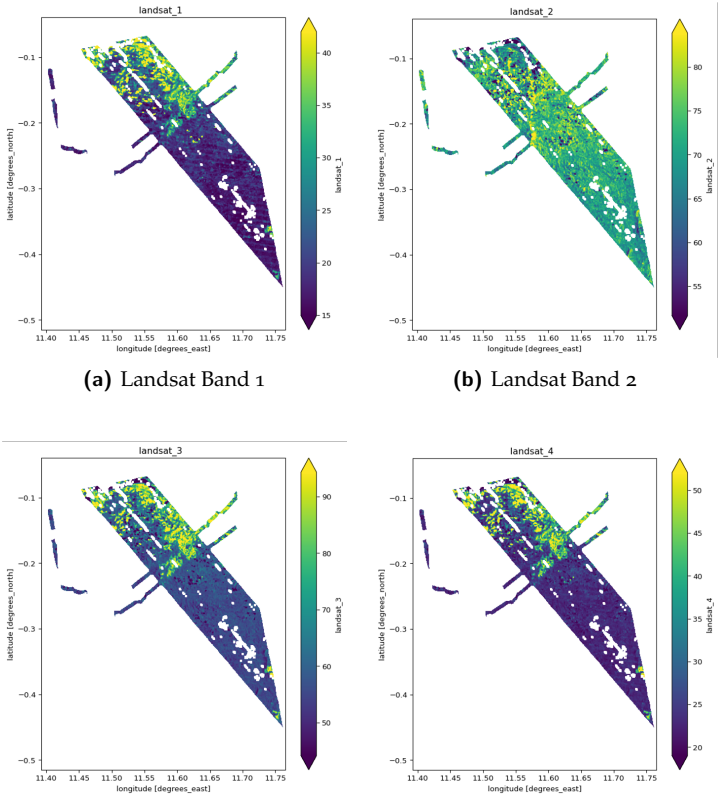

(a) Landsat Band 1 **(b)** Landsat Band 2

(c) Landsat Band 3 **(d)** Landsat Band 4

Figure B.1: Landsat spectral bands used as additional input features for Model D. The maps correspond to Scene No. 4 from Table 3.2 over Lopé.

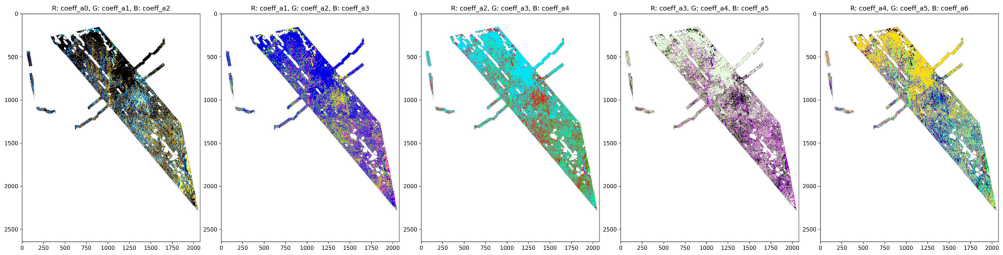

(a) Model C: false-color RGB of Legendre coefficients

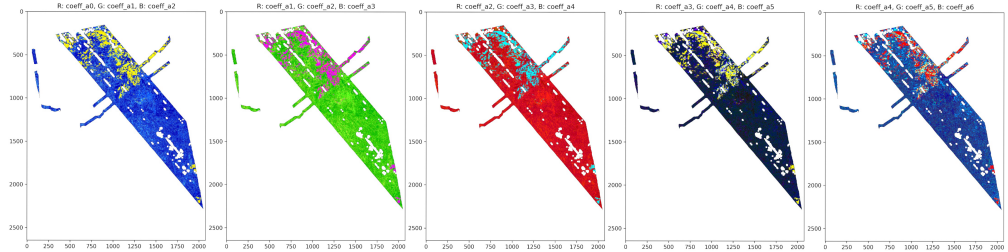

(b) Model D: false-color RGB of Legendre coefficients

Figure B.2: False-color RGB visualizations of the seven Legendre coefficients for Scene No. 4 from Table 3.2 over Lopé. Top: Model C. Bottom: Model D. Each panel shows five RGB triplets that map $(R : a_k, G : a_{k+1}, B : a_{k+2})$ to highlight spatial patterns by coefficient order.

Table B.1: Architecture of the MLP used in Paper 2.

Layer	Specification
Input	Number of input features (InSAR + geometry descriptors + Landsat spectral bands)
Hidden layer 1	128 neurons, Tanh activation
Hidden layer 2	64 neurons, Tanh activation
Hidden layer 3	32 neurons, Tanh activation
Output	Legendre coefficients / profile parameters

Table B.2: Training hyperparameters of the MLP (Paper 2).

Parameter	Value
Optimizer	Adam
Learning rate	1e-2
Batch size	256
Number of epochs	200
Early stopping	Patience of 20 epochs
Loss function	Mean squared error (MSE)

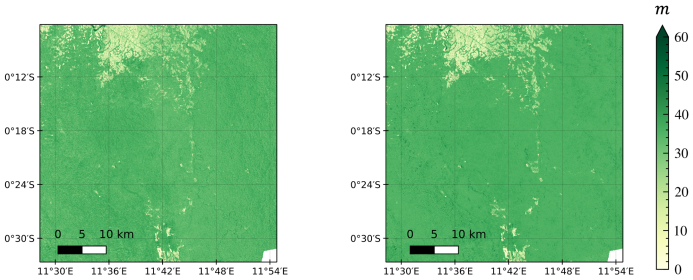

(a) Predicted forest height mosaics: left = Model C, right = Model D

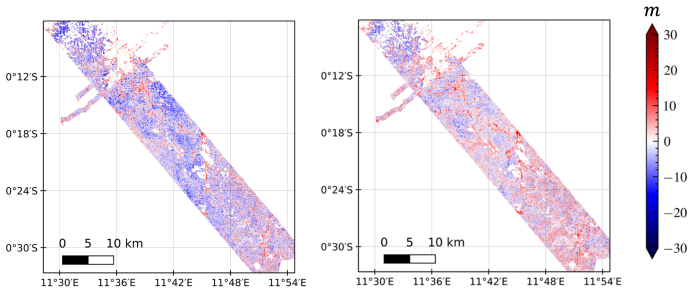

(b) Residual error maps (prediction – LVIS RH_{98}): left = Model C, right = Model D

Figure B.3: Top: mosaicked forest-height predictions from the Hybrid AI–InSAR model for Model C (left) and Model D (right). Bottom: residual error maps computed as (prediction – LVIS RH_{98}) for the same models.

REFERENCES

[1] C. Choi, V. Cazcarra-Bes, R. Guliaev, M. Pardini, K. P. Papathanassiou, W. Qi, J. Armston, and R. O. Dubayah, "Large-Scale Forest Height Mapping by Combining TanDEM-X and GEDI Data," *IEEE Journal of Selected Topics in Applied Earth Observations and Remote Sensing*, vol. 16, 2374, 2023. DOI: 10.1109/JSTARS.2023.3244866 (cited on page 87).

[2] R. Guliaev, V. Cazcarra-Bes, M. Pardini, and K. Papathanassiou, "Forest Height Estimation by Means of TanDEM-X InSAR and Waveform Lidar Data," *IEEE Journal of Selected Topics in Applied Earth Observations and Remote Sensing*, vol. 14, 3084, 2021. DOI: 10.1109/JSTARS.2021.3058837 (cited on page 87).

[3] F. Kugler, D. Schulze, I. Hajnsek, H. Pretzsch, and K. P. Papathanassiou, "TanDEM-X Pol-InSAR Performance for Forest Height Estimation," *IEEE Transactions on Geoscience and Remote Sensing*, vol. 52, no. 10, 6404, 2014. DOI: 10.1109/TGRS.2013.2296533 (cited on page 87).

[4] D. Carcereri, P. Rizzoli, D. Ienco, and L. Bruzzone, "A Deep Learning Framework for the Estimation of Forest Height From Bistatic TanDEM-X Data," *IEEE Journal of Selected Topics in Applied Earth Observations and Remote Sensing*, vol. 16, 8334, 2023. DOI: 10.1109/JSTARS.2023.3310209 (cited on page 87).

[5] M. Denbina, M. Simard, and B. Hawkins, "Forest Height Estimation Using Multibaseline PolInSAR and Sparse Lidar Data Fusion," *IEEE Journal of Selected Topics in Applied Earth Observations and Remote Sensing*, vol. 11, no. 10, 3415, 2018. DOI: 10.1109/JSTARS.2018.2841388 (cited on page 87).

[6] P. B. May, R. O. Dubayah, J. M. Bruening, and G. C. Gaines, "Connecting spaceborne lidar with NFI networks: A method for improved estimation of forest structure and biomass," *International Journal of Applied Earth Observation and Geoinformation*, vol. 129, 103797, 2024. DOI: 10.1016/j.jag.2024.103797 (cited on page 87).

[7] I. Mansour, K. Papathanassiou, R. Hänsch, and I. Hajnsek, "Hybrid Machine Learning Forest Height Estimation From TanDEM-X InSAR," *IEEE Transactions on Geoscience and Remote Sensing*, vol. 63, 1, 2025. DOI: 10.1109/TGRS.2024.3520387 (cited on pages 87, 88, 90, 92).

[8] J. Askne, P. Dammert, L. Ulander, and G. Smith, "C-band repeat-pass interferometric SAR observations of the forest," *IEEE Transactions on Geoscience and Remote Sensing*, vol. 35, no. 1, 25, 1997. DOI: 10.1109/36.551931 (cited on page 89).

[9] H. Zebker and J. Villasenor, "Decorrelation in interferometric radar echoes," *IEEE Transactions on Geoscience and Remote Sensing*, vol. 30, no. 5, 950, 1992. DOI: 10.1109/36.175330 (cited on page 89).

[10] J. O. Hagberg, L. M. Ulander, and J. Askne, "Repeat-pass SAR interferometry over forested terrain," *IEEE Transactions on Geoscience and Remote Sensing*, vol. 33, no. 2, 331, 1995. DOI: 10.1109/TGRS.1995.8746014 (cited on page 89).

[11] R. Bamler and P. Hartl, "Synthetic aperture radar interferometry," *Inverse Problems*, vol. 14, no. 4, R1, 1998. DOI: 10.1088/0266-5611/14/4/001 (cited on page 89).

[12] M. Martone, B. Bräutigam, P. Rizzoli, C. Gonzalez, M. Bachmann, and G. Krieger, "Coherence evaluation of TanDEM-X interferometric data," *ISPRS Journal of Photogrammetry and Remote Sensing*, Innovative Applications of SAR Interferometry from modern Satellite Sensors, vol. 73, 21, 2012. DOI: 10.1016/j.isprsjprs.2012.06.006 (cited on page 89).

[13] A. Roueff, A. Arnaubec, P. C. Dubois-Fernandez, and P. Refregier, "Cramer–Rao Lower Bound Analysis of Vegetation Height Estimation With Random Volume Over Ground Model and Polarimetric SAR Interferometry," *IEEE Geoscience and Remote Sensing Letters*, vol. 8, no. 6, 1115, 2011. DOI: 10.1109/LGRS.2011.2157891 (cited on page 89).

[14] R. N. Treuhaft and P. R. Siqueira, "Vertical structure of vegetated land surfaces from interferometric and polarimetric radar," *Radio Science*, vol. 35, no. 1, 141, 2000. DOI: 10.1029/1999RS900108 (cited on page 89).

[15] F. Kugler, Seung-Kuk Lee, I. Hajnsek, and K. P. Papathanassiou, "Forest Height Estimation by Means of Pol-InSAR Data Inversion: The Role of the Vertical Wavenumber," *IEEE Transactions on Geoscience and Remote Sensing*, vol. 53, no. 10, 5294, 2015. DOI: 10.1109/TGRS.2015.2420996 (cited on page 89).

[16] S. R. Cloude, "Polarization coherence tomography," *Radio Science*, vol. 41, no. 4, 2006. DOI: 10.1029/2005RS003436 (cited on page 89).

[17] S. R. Cloude, "Dual-Baseline Coherence Tomography," *IEEE Geoscience and Remote Sensing Letters*, vol. 4, no. 1, 127, 2007. DOI: 10.1109/LGRS.2006.885893 (cited on page 89).

[18] European Space Agency and Airbus, *Copernicus DEM*, European Space Agency, 2022. DOI: 10.5270/ESA-c5d3d65 (cited on page 92).

[19] M. C. Hansen, P. V. Potapov, R. Moore, M. Hancher, S. A. Turubanova, A. Tyukavina, D. Thau, S. V. Stehman, S. J. Goetz, T. R. Loveland, A. Kommareddy, A. Egorov, L. Chini, C. O. Justice, and J. R. G. Townshend, "High-Resolution Global Maps of 21st-Century Forest Cover Change," *Science*, vol. 342, no. 6160, 850, 2013. DOI: 10.1126/science.1244693 (cited on page 92).

[20] J. Armston, H. Tang, S. Hancock, S. Marselis, L. Duncanson, J. Kellner, M. Hofton, J. B. Blair, T. Fatoyinbo, and R. O. Dubayah, *AfriSAR: Gridded Forest Biomass and Canopy Metrics Derived from LVIS, Gabon, 2016*, 2020 (cited on page 92).

4

HYBRID AI–PHYSICAL MODELING FOR PENETRATION BIAS CORRECTION IN X-BAND INSAR DEMS: A GREENLAND CASE STUDY

Islam Mansour[1,2], Georg Fischer[1], Ronny Hänsch[1], and Irena Hajnsek[1,2]

1 Microwaves and Radar Institute, German Aerospace Center DLR, Germany

2 Institute of Environmental Engineering, ETH Zurich, Switzerland

Article published in *2025 IEEE/CVF Conference on Computer Vision and Pattern Recognition Workshops (CVPRW)*
Citation: I. Mansour et al., "Hybrid AI-physical modeling for penetration bias correction in X-band InSAR DEMs: A Greenland case study," 2175, Jun. 2025. DOI: 10.1109/CVPRW67362.2025.00205

Key findings:

- Developed a novel hybrid framework combining physical models with machine learning for correcting InSAR DEM penetration bias.
- Evaluated model performance across three distinct training scenarios with different Height of Ambiguity (HoA) ranges.
- Demonstrated that hybrid approach, especially Exponential model, outperforms pure ML when key HoA ranges are missing from training data.

Author's contributions:

- Developed the novel hybrid modeling methodology.
- Post-processed the data for volume decorrelation analysis.
- Integrated and processed the ATM LiDAR reference data.

Co-author's contributions:

- G. Fischer: Contributed pre-processed TanDEM-X data, offered guidance on physical model development, and proposed the evaluation of the hybrid approach using different training scenarios.
- R. Hänsch: Provided guidance and expertise on machine learning component development and its optimization.
- I. Hajnsek: Provided supervision and guidance on overall research direction.
- All co-authors collectively contributed to the method development, result discussion, and manuscript revision.

This chapter is a pre-print of the above-listed manuscript, differing from the submitted version only in terms of layout, formatting, and citation style.

Abstract

Digital elevation models derived from Interferometric Synthetic Aperture Radar (InSAR) data over glacial and snow-covered regions often exhibit systematic elevation errors, commonly termed "penetration bias." We leverage existing physics-based models and propose an integrated correction framework that combines parametric physical modeling with machine learning. We evaluate the approach across three distinct training scenarios — each defined by a different set of acquisition parameters — to assess overall performance and the model's ability to generalize. Our experiments on Greenland's ice sheet using TanDEM-X data show that the proposed hybrid model corrections significantly reduce the mean and standard deviation of DEM errors compared to a purely physical modeling baseline. The hybrid framework also achieves significantly improved generalization than a pure ML approach when trained on data with limited diversity in acquisition parameters. [1]

1 The source code is available at https://github.com/IslamAlam/pydeepsar

4.1 INTRODUCTION

Interferometric Synthetic Aperture Radar (InSAR) has enabled the generation of high-resolution Digital Elevation Models (DEMs) over large areas, such as the global Copernicus DEM derived from TanDEM-X [1]. These DEMs are crucial for many applications, including cryospheric studies, where they enable monitoring of glacier mass balance and ice sheet dynamics [2].

One of the main challenges in generating InSAR DEMs is the penetration of the radar signal into dry snow and ice. This causes the measured elevation to lie several meters below the actual surface, leading to the so-called penetration bias [3], [4], [5], [6]. For example, a recent study by Fan et al. [6] compared DEMs derived from ICESat-2 (a laser altimeter sensor) and TanDEM-X (an X-band radar sensor) data over Greenland and found that the elevation bias varies significantly with terrain elevation. In their analysis, for elevations above 2000 m the median difference (MED) between the DEMs is approximately -3.76 m (with an RMSE of 4.51 m), whereas for elevations below 2000 m the MED is around -2.32 m (with an RMSE of 7.00 m), yielding an overall MED of -2.75 m and RMSE of 6.58 m. This pronounced bias — primarily due to X-band signal penetration into the ice — illustrates both the inherent challenge of penetration bias and the influence of topography, thereby motivating the need for advanced correction techniques.

There is potential to estimate the penetration bias directly from the InSAR data, because the signal penetration depends on the snow and ice properties, which, in turn, influence the backscatter and coherence measured by the InSAR system. The key relationship is between the vertical scattering profile, which describes how the backscattered signals are distributed within the snow and ice, and the interferometric coherence, which measures the correlation between the InSAR acquisition pair. Typically, a shallow vertical scattering profile leads to high coherence, whereas deep penetration causes low coherence. This relationship depends on the InSAR acquisition geometry that determines the interferometric height sensitivity, which is described by the Height of Ambiguity (HoA) parameter.

Physical models, such as the Uniform Volume (UV) model (which assumes a uniform signal extinction in snow and ice, i.e., an

exponential vertical profile), are used to estimate the penetration depth under idealized conditions [7], [8], [9]. One key advantage of these physics-based methods is that they do not require any additional training or reference data, unlike data-driven approaches that depend on high-quality reference data. However, these models can over- or underestimate the bias when real scattering scenarios deviate from their simplifications. In contrast, purely data-driven approaches, such as machine learning (ML) models, can capture local variations more accurately and flexibly but may lack the robustness and interpretability of physics-based methods [2], [10].

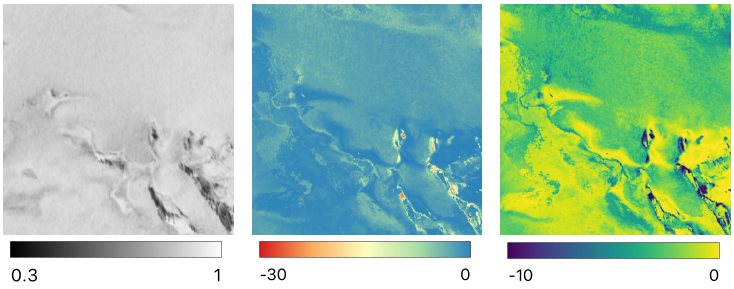

Figure 4.1: Qualitative example from a representative region. *Left*: Interferometric coherence (range: 0.3–1). *Center*: One-way penetration depth (d_{pen}, in meters) predicted by the MLP component of our hybrid framework, which then feeds into the Exponential profile. *Right*: Final penetration bias (p_{bias}, in meters). This hybrid approach leverages InSAR features (e.g., coherence) to predict d_{pen}, which is subsequently used to estimate p_{bias} for correcting DEM elevations over ice and snow.

Building upon our initial hybrid framework [11], we present an expanded analysis that synergistically combines physical models with ML approaches. While our previous work focused solely on the Exponential profile, here we systematically evaluate two parametric physical models (Exponential and Weibull profiles) to comprehensively understand their capabilities and limitations in modeling vertical scattering profiles. We train a Multi-Layer Perceptron (MLP) to predict the parameters of these physical models from the data, as illustrated in Figure 4.1. To rigorously assess generalization capabilities, we introduce three distinct HoA scenarios: (1) training with all available HoA scenes, (2) an *Interpolation scenario* where we exclude mid-range HoA values to test interpolation capa-

bilities, and (3) an *Extrapolation scenario* where we exclude higher HoA values to evaluate extrapolation performance. This systematic evaluation provides crucial insights into model robustness and generalization capabilities across variable acquisition geometries as expected for large scale InSAR applications.

4.2 RELATED WORK

4.2.1 *Physical Modeling Approaches*

Accurate electromagnetic modeling of the vertical scattering profile in snow and ice is a critical prerequisite for correcting the penetration bias in InSAR-derived DEMs. The interaction of microwaves with natural snow cover is complex because the snow comprises heterogeneous mixtures of ice grains and air that also depend on environmental conditions such as temperature and metamorphism processes. Early studies provide insights into the dielectric properties and scattering mechanisms in natural snow [12].

The Uniform Volume (UV) is introduced as a simplified model for the scattering medium [7]. It treats the snow and ice volume as an infinitely deep, homogeneous medium with a constant signal extinction coefficient, leading to an exponential vertical scattering profile. Under these assumptions, the penetration bias can be estimated directly from the InSAR data using the UV model [8], [13]. Another more flexible solution is based on the Weibull profile [9] capturing changes in signal extinction due to increasing grain size and density with depth [12]. It is able to compensate for the underestimation of the UV model, but it is also prone to overestimating the surface location [9].

4.2.2 *Data-Driven Approaches*

Purely data-driven methods bypass explicit physical modeling by learning the mapping between observable SAR features (e.g., interferometric coherence and backscatter intensity) and the target variable (e.g., the penetration bias, snow-facies) directly from training data.

A key study proposes a pixel-based regression approach for estimating X-band InSAR elevation bias over Greenland [2]. Their

method achieves a coefficient of determination (R^2) of 0.68 and an RMSE of 0.68 m. While computationally efficient, this approach is limited by its linearity and lack of explicit physical constraints.

Other recent work explores deep learning-based methods, for example, using a deep unsupervised learning approach for the classification of snow facies [10], [14]. In this case, the snow facies are segmented and used for the penetration bias estimation.

Although these methods can capture complex empirical relationships, they generally require extensive, high-quality training datasets — often derived from sources such as CryoSat-2 or ICESat-2 — that are very limited. Furthermore, purely data-driven approaches often struggle to generalize to conditions outside the training domain. The absence of explicit physical constraints also limits their interpretability.

4.2.3 *Hybrid Approaches*

Hybrid inversion methods combine model-based and data-driven approaches to leverage their advantages [15]. This fusion, called hybrid modeling, combines physical model interpretability and rigor with ML's flexibility and adaptiveness. Physics-informed ML embeds physical constraints into learning algorithms, ensuring models fit data and adhere to physical laws [16]. This approach has proven effective in complex applications like fluid dynamics and climate modeling [17], [18], [19]. It holds a potential for inverting geo- and biophysical parameters from SAR data, overcoming limitations of purely physical or data-driven methods.

Recent work on the parameterization of the vertical scattering profile for forest height estimation has demonstrated that hybrid approaches can significantly improve the estimation of geophysical parameters [20]. However, despite its potential, specific work on physics-informed machine learning for InSAR parameter retrieval is lacking in current literature. Our work builds on these ideas by embedding the Exponential and Weibull profiles into a hybrid architecture. We compare the performance of these hybrid models with pure ML models for different HoA training scenarios, showing that incorporating physical constraints leads to improved accuracy, stability, and robustness — mainly when high-quality training data are limited.

4.3 METHODOLOGY

4.3.1 *Problem Formulation*

Let h_{InSAR} be the InSAR-derived elevation and h_{ref} the reference "true" elevation at a given location. We define the penetration bias as

$$p_{\text{bias}} = h_{\text{InSAR}} - h_{\text{ref}}, \tag{4.1}$$

which must be estimated and removed to improve DEM accuracy in glaciated regions.

4.3.2 *Physical Models (Exponential, Weibull)*

The estimation of penetration bias is grounded in physical models that link the InSAR observation space to the vertical scattering profile in snow and ice — governed by geophysical parameters such as density, structure, and grain size.

In single-polarization InSAR, the primary observable is the complex coherence, $\tilde{\gamma}$, which represents the cross-correlation between two acquisitions, s_1 and s_2 and is defined as [21], [22], [23]:

$$\tilde{\gamma}(\kappa_z) = \frac{\langle s_1 \, s_2^* \rangle}{\sqrt{\langle s_1 \, s_1^* \rangle \, \langle s_2 \, s_2^* \rangle}}, \tag{4.2}$$

where κ_z is the vertical wavenumber, $\langle \cdot \rangle$ denotes an ensemble (or spatial) average, and * indicates the complex conjugate. The observed coherence is factorized into several decorrelation terms, and can be expressed as [24], [25], [26], [27]:

$$\tilde{\gamma}(\kappa_z) = \gamma_{Tmp} \, \gamma_{Rg} \, \gamma_{Sys} \, \tilde{\gamma}_{\text{Vol}}(\kappa_z), \tag{4.3}$$

where γ_{Tmp} accounts for temporal decorrelation, γ_{Rg} represents range spectral decorrelation, γ_{Sys} captures system-related decorrelation, and $\tilde{\gamma}_{\text{Vol}}(\kappa_z)$ corresponds to the volume decorrelation due to subsurface scattering. For TanDEM-X single-baseline InSAR, temporal decorrelation does not occur ($\gamma_{Tmp} = 1$) and the other decorrelation factors are known [28], [29], [30].

To estimate the penetration bias p_{bias}, we focus on the volume decorrelation $\tilde{\gamma}_{\text{Vol}}(\kappa_z)$, which is directly linked to the vertical scattering profile $f(z)$ describing how backscattered power varies with depth z. For a semi-infinite volume ($z \leq 0$), the volume decorrelation is given by [13]:

$$\tilde{\gamma}_{\text{Vol}}(\kappa_z) \;=\; e^{j\,\kappa_z\,z_0}\,\frac{\int_{-\infty}^{0} f(z)\;\exp(j\,\kappa_z\,z)\,dz}{\int_{-\infty}^{0} f(z)\,dz}, \tag{4.4}$$

where z_0 is the true surface height. The phase of $\tilde{\gamma}_{\text{Vol}}(\kappa_z)$, denoted as $\phi_{\text{Vol}} = \arg\big(\tilde{\gamma}_{\text{Vol}}(\kappa_z)\big)$, corresponds to the interferometric phase center, located in the subsurface. The penetration bias p_{bias} is then calculated as

$$p_{\text{bias}} \;=\; \frac{\phi_{\text{Vol}}}{\kappa_z}, \tag{4.5}$$

assuming $z_0 = 0$ for simplicity. In practice, a known offset may be incorporated if z_0 differs from a reference DEM.

The detailed definitions of the vertical wavenumber κ_z and the HoA — which quantifies the interferometric phase-to-height sensitivity — are provided in the Supplementary Material (see Section C.1, Eqs. S1 and S2). Briefly, these parameters relate the observed phase to height and are used to compute the elevation from the phase center.

The physical models assume a specific form for the vertical scattering profile $f(z)$. The UV model leads to an *Exponential profile*, which is described as [7]:

$$f_{\text{exp}}(z) \;=\; \sigma_v^0\,\exp\Big(\frac{2z}{d_{\text{pen}}}\Big), \tag{4.6}$$

where d_{pen} is the one-way penetration depth and σ_v^0 is a nominal scattering coefficient. Figure 4.2 shows how the resulting penetration bias varies with different d_{pen} values.

Under uniform-volume assumptions, one can derive a closed-form solution for $\tilde{\gamma}_{\text{Vol}}(\kappa_z)$, making it possible to estimate the pen-

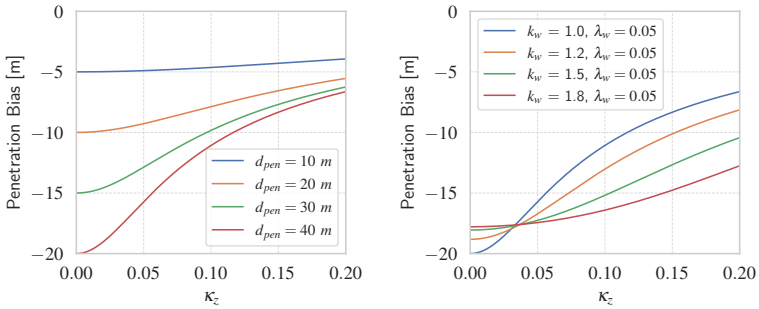

(a) Exponential Profile **(b)** Weibull Profile

Figure 4.2: Penetration bias simulations for two scattering profiles, assuming a semi-infinite volume.
(**a**) Exponential Profile with varying penetration depth d_{pen}.
(**b**) Weibull Profile for different shape parameters k_w and fixed scale $\lambda_w = 0.05$. In both, the curves illustrate the penetration bias variation as a function of vertical wavenumber κ_z.

etration bias p_{bias} independently of d_{pen}. In this case, the volume decorrelation phase is given by [8]:

$$\phi_{\text{Vol}} \;=\; \tan^{-1}\Big(\sqrt{\frac{1}{|\gamma_{\text{Vol}}|^2} - 1}\Big). \tag{4.7}$$

We leverage this solution for computing p_{bias} in our direct *physical-model* estimation and use Eq. (4.4) with Eq. (4.6) in the hybrid approach.

In contrast, the *Weibull profile* is given by [9]:

$$f_{\text{wb}}(z) \;=\; \lambda_w\, k_w\, (\lambda_w\, z)^{\,k_w - 1}\, \exp\Big(-(\lambda_w\, z)^{\,k_w}\Big), \tag{4.8}$$

where λ_w (scale) and k_w (shape) allow for a more flexible representation of scattering behavior. Figure 4.2 shows how different k_w values affect the penetration bias. However, estimating its two parameters, λ_w and k_w, can be challenging. To ensure physically plausible solutions, we constrain λ_w to $[0.01, 0.6]$ and k_w to $[0.8, 1.5]$. These parameter ranges provide vertical scattering profiles and associated penetration depths matching empirical data [9], [31].

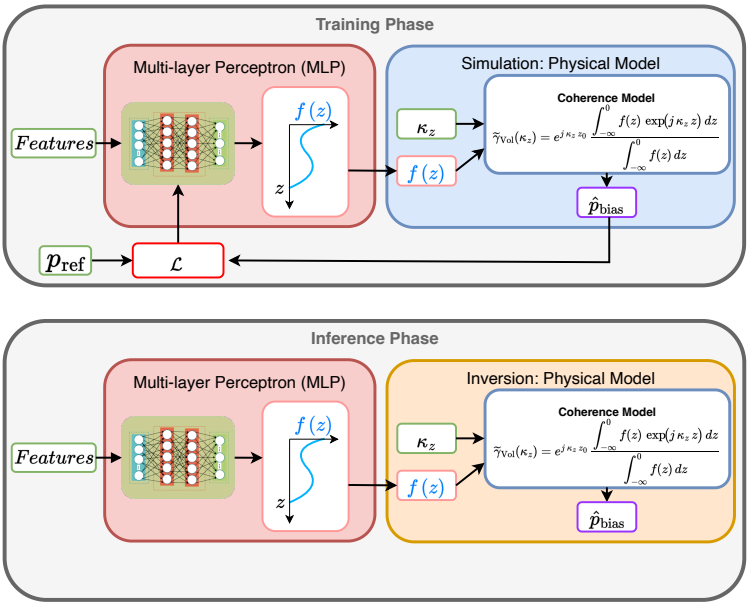

Figure 4.3: Overview of our hybrid modeling pipeline. An MLP predicts scattering profile parameters that feed into the physical model for computing the estimated bias $\hat{p}_{\text{bias}}$. We use MSE loss against a reference bias (e.g., LiDAR).

These models can be integrated into Eq. 4.4 to compute the volume decorrelation $\tilde{\gamma}_{\text{Vol}}(\kappa_z)$ and subsequently estimate the penetration bias p_{bias}.

4.3.3 *Hybrid AI–Physical Model*

Our proposed hybrid framework (illustrated in Figure 4.3) synergistically combines physical modeling with machine learning to estimate p_{bias} (Eq. 4.1). Rather than relying solely on a fixed vertical scattering profile $f(z)$ derived from idealized assumptions, we allow the model to learn the parameters that define $f(z)$ from data. In practice, we train a MLP to predict the scattering profile parameters (e.g., $\hat{d}_{\text{pen}}$ for the Exponential profile or $(\hat{\lambda}_w, \hat{k}_w)$

for the Weibull profile) from input features such as volumetric decorrelation, incidence angle, vertical wavenumber, interferometric phase, and backscatter. Given the low spatial variability in these homogeneous glaciated regions — and since even simple linear regression can estimate penetration bias with moderate accuracy — a straightforward MLP suffices, removing the need for more complex deep learning architectures [2]. This approach enables us to derive a unique solution that satisfies the physical constraints while adapting to real-world variability. The predicted parameters are then used in the volume decorrelation (Eq. (4.4)) to compute the estimated penetration bias $\hat{p}_{\text{bias}}$. We train the hybrid model by minimizing the mean-squared-error (MSE) loss:

$$\mathcal{L}_{\text{MSE}} = \frac{1}{N} \sum_{n=1}^{N} \left(\hat{p}_{\text{bias},n} - p_{\text{ref},n} \right)^2, \tag{4.9}$$

where $p_{\text{ref},n}$ denotes the reference bias for the nth sample and $\hat{p}_{\text{bias},n}$ represents the estimated penetration bias computed as in Eq. 4.5.

4.4 EXPERIMENTS

4.4.1 *Dataset*

4.4.1.1 *TanDEM-X InSAR Data*

This study utilizes single-baseline InSAR imagery from the TanDEM-X mission to generate InSAR DEMs over Greenland. A total of **18** TanDEM-X CoSSC acquisitions are selected, covering a transect from the ice sheet summit to the East Coast, ensuring temporal and spatial alignment with NASA IceBridge data. Figure 4.4 provides an overview of the TanDEM-X scene footprints (in blue) and the corresponding NASA IceBridge ATM flight tracks (in red), acquired between January and May 2017 during the winter season.

Post-processing steps include the derivation of InSAR elevation, coherence, backscatter, incidence angle, and vertical wavenumber. A mosaic overview of these acquisitions is shown in Figure 4.5.

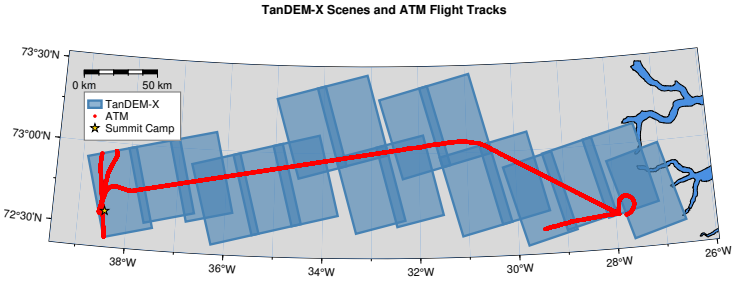

Figure 4.4: Overview of TanDEM-X scenes (blue) and ATM flight tracks (red) over the study area in Greenland. The Summit Camp location is marked with a yellow star.

4.4.1.2 *NASA IceBridge ATM LiDAR Data*

For training and validation of the penetration bias correction model, we use the high-resolution surface elevation data from NASA's IceBridge Airborne Topographic Mapper (ATM) [32]. The ATM LiDAR dataset provides precise elevation measurements with a vertical uncertainty of less than 1 m over flat ice surfaces. To ensure consistency with the InSAR-derived DEMs, the original 1 m-resolution ATM dataset is resampled to the same grid as the InSAR products.

Leveraging these reference measurements, we also examine how the observed penetration bias varies with surface elevation. As shown in Figure 4.6, higher elevations exhibit greater bias, as expected [2], [6], due to more dry snow with less melt-refreeze features in the subsurface allowing deeper X-band signal penetration.

4.4.2 *HoA-Based Training Scenarios*

To investigate how each method (hybrid or pure ML) generalizes to different HoA conditions, we define three training scenarios that include or exclude specific HoA ranges. We remove the scenes whose HoA values fall in the specified range (see Figure 4.5 (d) for an overview of the HoA distribution). The *All* scenario uses every scene, *Interpolation* excludes HoA in $[50, 60]$ m, and *Extrapolation* excludes HoA above 70 m.

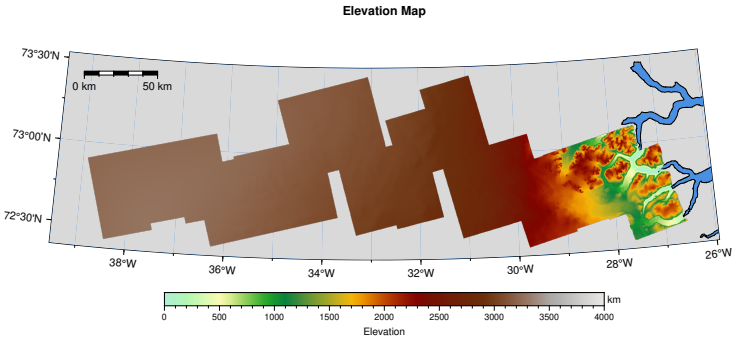

(a) Elevation (DEM) from TanDEM-X

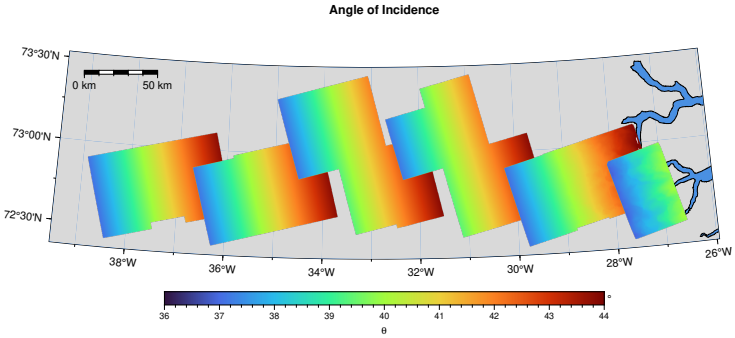

(b) Incidence Angle

Figure 4.5: Dataset overview (continued 1/2).

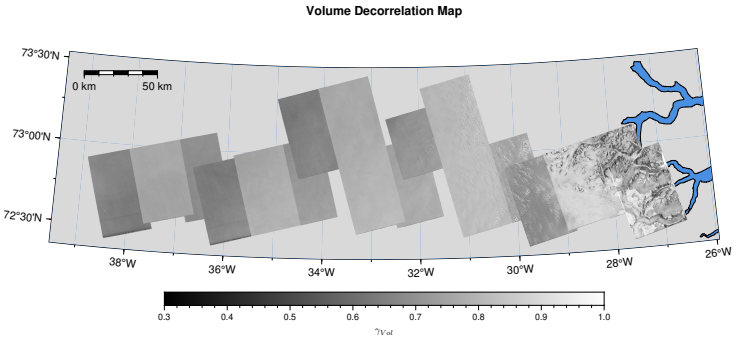

(c) Volume Decorrelation

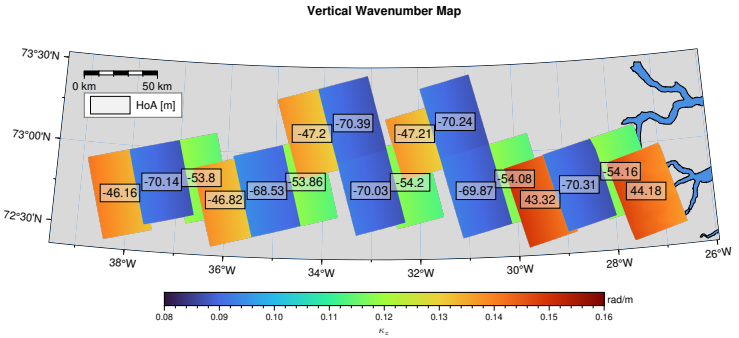

(d) Vertical Wavenumber and HoA

Figure 4.5: Overview of the mosaicked dataset used in our study. Each panel shows a different attribute for the 2017 TanDEM-X acquisitions over Greenland.

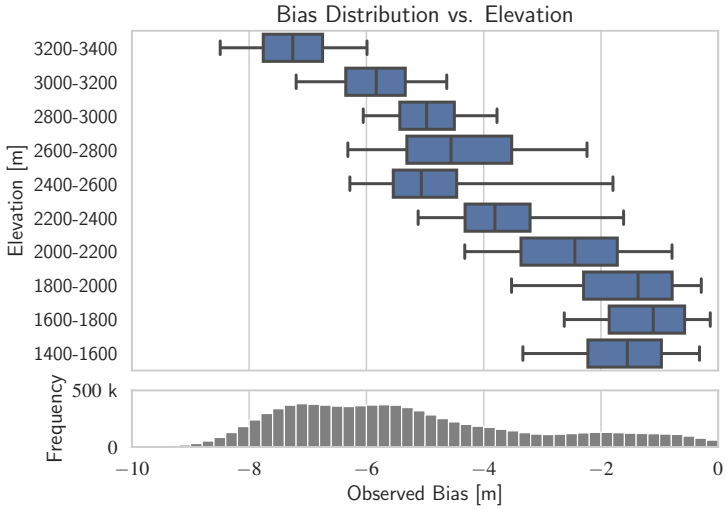

Figure 4.6: Bias distribution across elevation bins, computed using ATM LiDAR as reference. The penetration bias increases at higher elevations due to smaller scattering losses from less melt-refreeze features in the subsurface.

We split the remaining data into training (60%) and testing (40%) sets, ensuring a broad distribution of ice sheet conditions. This approach reveals how well each model handles cases requiring interpolation (HoA gaps within the trained range) or extrapolation (HoA values beyond the trained range). In subsequent sections, we compare each scenario's performance to assess model robustness and generalization. For a more detailed view of the specific scenes included or excluded in each scenario, see Figure C.3 in the Supplementary Material.

4.4.3 *Metrics*

We evaluate the prediction accuracy using the mean error (ME), mean absolute error (MAE), mean absolute percentage error (MAPE), root mean square error (RMSE), and the coefficient of determination (R^2). These metrics quantify the estimator's bias, overall error magnitude, relative percentage error, and goodness of

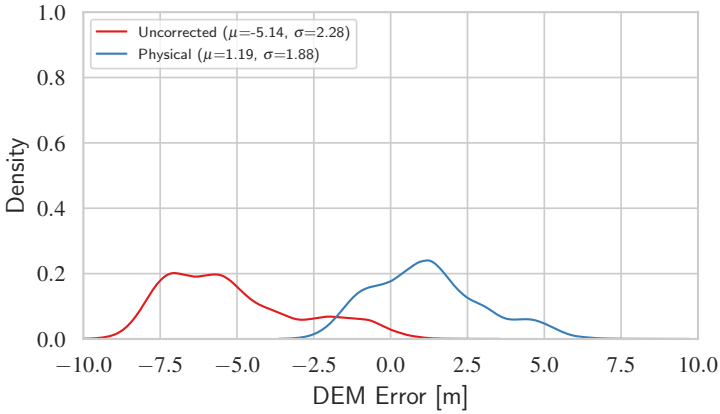

Figure 4.7: Error distributions for the uncorrected DEM (red) versus the physically corrected DEM (blue) using the UV direct solution of Eq. 4.7.

fit, respectively. In addition, we characterize the error distribution of the DEMs by computing the mean error (μ) and the standard deviation (σ). For the mathematical formulations of these metrics, please refer to the Supplementary Material (Section C.2).

4.4.4 *Pure ML Approach (MLP)*

As an alternative to our hybrid framework, we implement a purely data-driven MLP model as a benchmark. This model directly regresses $\hat{p}_{\text{bias}}$ from the input features, without incorporating explicit physical modeling of scattering physics. We train the MLP by minimizing the same MSE loss defined in Eq. 4.9, where $\hat{p}_{\text{bias}}$ denotes the bias predicted by the MLP.

4.4.5 *Results*

We present the quantitative findings for the different experiments for all the TanDEM-X scenes. The overall performance metrics (ME, MAE, MAPE, RMSE, and R^2) are shown in Table 4.1. It also shows the error distribution statistics (mean μ and standard deviation σ) for the uncorrected TanDEM-X DEM, the TanDEM-X

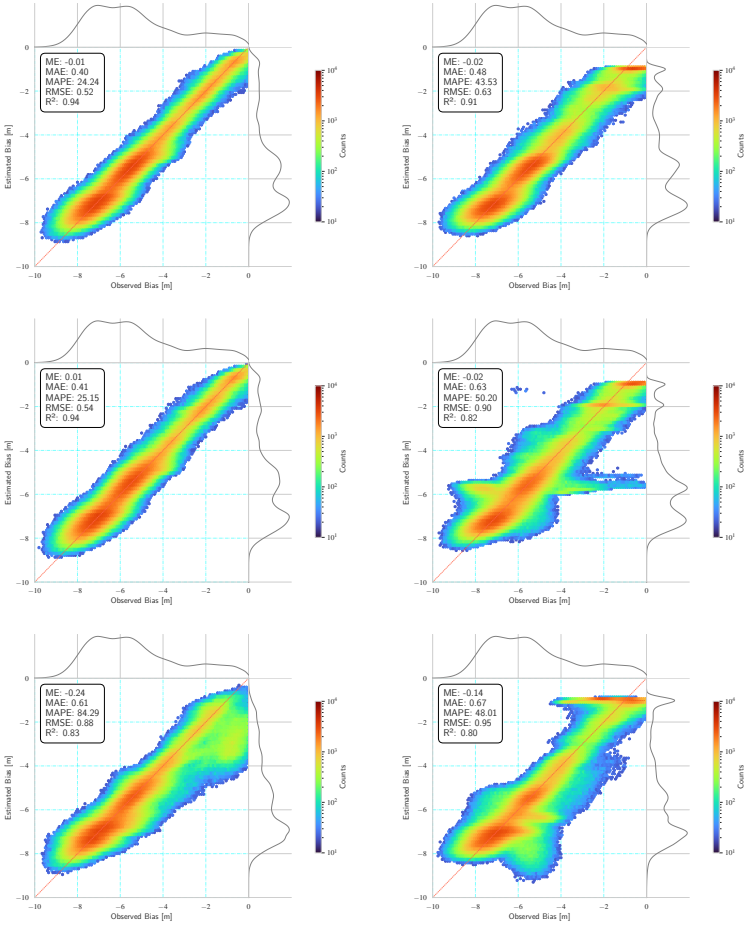

Figure 4.8: Comparison of model estimations (continued 1/2).

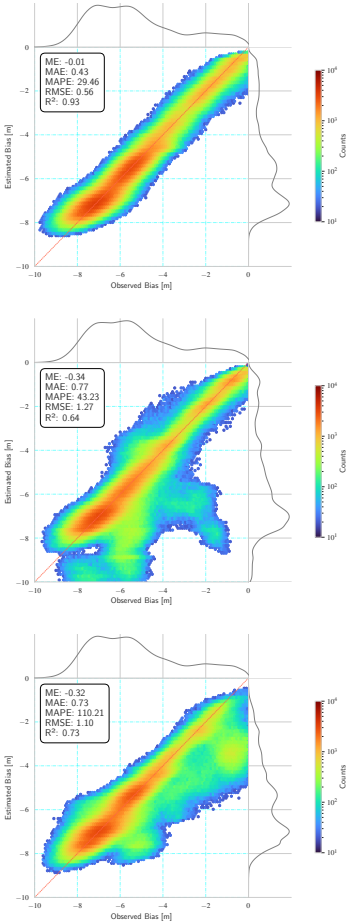

Figure 4.8: Comparison of model estimations under different training and evaluation conditions. Columns correspond to modeling approaches: Exponential, Weibull, and MLP. Each column stacks three scenarios (top→bottom): *All*, *Interpolation* (excluding HoA 50–60), and *Extrapolation* (excluding HoA > 70). Comparison with the UV model is shown in Figure C.1 of the Supplementary Material.

DEM corrected by applying the UV model's estimated bias, and the three Hybrid/ML methods, respectively. Results are reported for three different HoA training scenarios: *All*, *Interpolation*, and *Extrapolation*.

The uncorrected DEM exhibits a large negative bias (e.g., $\mu \approx -5.14$) with a wide error spread ($\sigma \approx 2.28$). The UV correction reduces the bias partially (with $\mu \approx 1.19$), see Figure 4.7, but shows high RMSE (2.07 m) and very low R^2 (0.06) as indicated by the 2D histogram in Figure C.1 in the Supplementary Material . This indicates that the penetration bias inverted with a UV model only from the volumetric coherence Eq. 4.7, is insufficient to capture the actual scattering behavior.

On the other side, the hybrid methods (*Exponential* and *Weibull*) significantly improve the performance. Especially, the Exponential hybrid model achieves the lowest RMSE (as low as 0.52 m) and highest R^2 (0.94) in the *All* scenario. Both the hybrid and the MLP approaches produce comparable results when training on the full HoA range.

Figure 4.9 shows the performance of the *Exponential*, *Weibull*, and *MLP* models under three training scenarios. When the entire HoA range is used (*All*), all methods yield tight error distributions centered near zero. Excluding HoA values between 50 and 60 m during training (*Interpolation*) increases errors; here, the Exponential model retains low errors and high R^2 compared to the more variable *MLP* and *Weibull* models. Excluding HoA above 70 m during training (*Extrapolation*) leads to a more pronounced performance drop, especially for the *MLP*, while the *Exponential* model remains robust and the *Weibull* model shows moderate degradation.

Figure 4.8 illustrates 2D histograms of estimated versus observed penetration bias for the *Exponential*, *Weibull*, and *MLP* models under three HoA training scenarios. In the *All* scenario (top row), all methods cluster tightly around the diagonal line, indicating minimal residual bias. When excluding HoA values between 50 and 60 m during training (*Interpolation*, middle row), the *Exponential* model retains a narrow spread and high correlation with the true bias, whereas the *Weibull* and *MLP* plots exhibit more dispersion. Under the *Extrapolation* scenario (bottom row), which excludes HoA values above 70 m during training, the *MLP* displays

a broader scatter, while the *Exponential* model remains comparatively well aligned with the diagonal and the *Weibull* model shows moderate degradation. Overall, these histograms confirm that the *Exponential* model is the most robust to unseen HoA conditions, followed by the *Weibull* and *MLP* approaches. For a spatial visualization of the predicted penetration bias maps, see Figure C.4 in the Supplementary Material.

Figure 4.10 depicts the error distributions for the six models that were trained excluding specific HoA ranges, and then evaluated on unseen HoA scenes. The *Exponential* model consistently exhibits narrower error distributions and lower mean errors, confirming its robust generalization even when key HoA values are missing. The *Weibull* model maintains a near-zero mean under the *Interpolation scenario* but shows a broader spread, and its mean shifts moderately under the *Extrapolation scenario* — though it still avoids large outliers. In contrast, the *MLP* model displays the largest mean shift and widest spread, indicating a higher sensitivity to out-of-distribution HoA conditions. Overall, these results confirm that physically constrained models (particularly the *Exponential* model, followed by the *Weibull* model) are better suited to handling unseen HoA scenarios. See Figure C.5 in the Supplementary Material for the corresponding 2D histograms.

4.5 DISCUSSION

Our findings indicate that the hybrid approach, particularly the *Exponential model*, stands out as the most effective method for correcting DEM penetration bias. Even though the *Exponential model* is relatively simple — requiring only one parameter — it consistently delivers low RMSE and MAE values along with high R^2 scores across all training scenarios. Our experiments show that the model maintains pronounced robustness under both the *Interpolation scenario* and the *Extrapolation scenario* when evaluated on unseen HoA conditions. This consistent performance is further demonstrated in Figure C.6 of the supplemental material, where the *Exponential model* (left column) shows stable error distributions across different elevation bins for all scenarios. A small weakness of the *Exponential model* in the *Extrapolation scenario* are unseen HoA at low elevations. The wider error distributions of the *Weibull*

Table 4.1: Overall performance metrics for the uncorrected DEM and for the DEM corrected by the Physical (Uniform Volume) model and the three Hybrid/ML models (*Exponential*, *Weibull*, *MLP*). Results are shown under the three HoA scenarios for training (*All*, *Interpolation*, *Extrapolation*), using all 18 TanDEM-X scenes. Columns 3–7 show standard error metrics, while the last two columns (μ and σ) correspond to the DEM error distribution.

Approach	Scenario	ME	MAE	MAPE	RMSE	R^2	μ	σ
Uncorrected	–	–	–	–	–	–	-5.14	2.28
Physical (UV)	–	-1.11	1.64	208.75	2.07	0.06	1.19	1.88
Exponential	***All***	-0.01	0.40	24.24	0.52	0.94	0.03	0.67
Exponential	***Interpolation***	0.01	0.41	25.15	0.54	0.94	0.01	0.69
Exponential	***Extrapolation***	-0.24	0.61	84.29	0.88	0.83	0.28	0.97
Weibull	***All***	-0.02	0.48	43.53	0.63	0.91	0.05	0.77
Weibull	***Interpolation***	-0.02	0.63	50.20	0.90	0.82	0.05	1.02
Weibull	***Extrapolation***	-0.14	0.67	48.01	0.95	0.80	0.16	1.04
MLP	***All***	-0.01	0.43	29.46	0.56	0.93	0.03	0.70
MLP	***Interpolation***	-0.34	0.77	43.23	1.27	0.64	0.47	1.40
MLP	***Extrapolation***	-0.32	0.73	110.21	1.10	0.73	0.37	1.19

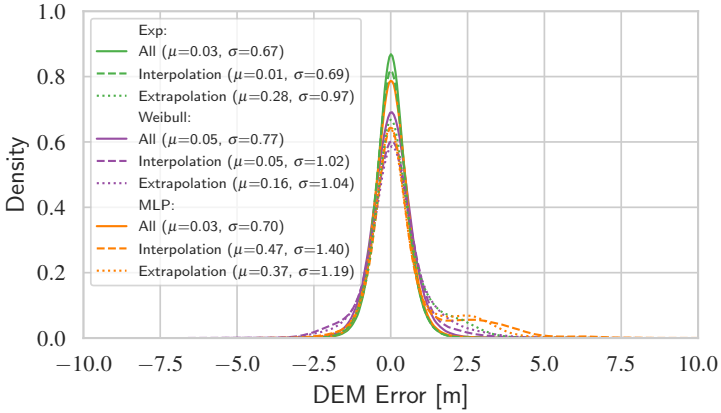

Figure 4.9: DEM error distributions for the nine modeling approaches (*Exponential*, *Weibull*, and *MLP* under three HoA scenarios) evaluated across all 18 TanDEM-X acquisitions. The mean μ and standard deviation σ are shown in the legend.

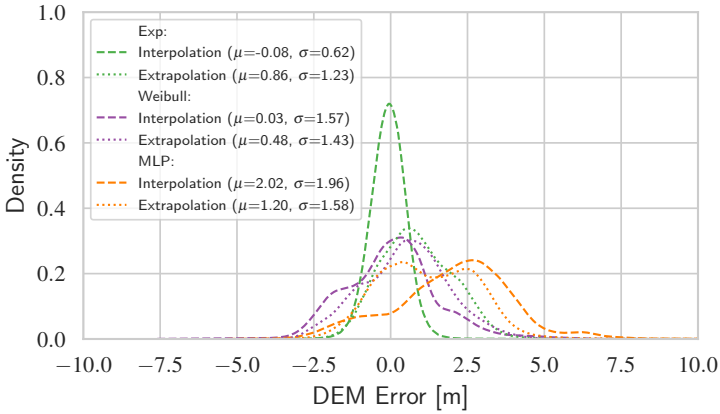

Figure 4.10: DEM error distributions for the six models that exclude certain HoA ranges during training (*Interpolation* and *Extrapolation*), evaluated on the unseen HoA scenes. The three models trained on all HoA values are omitted here. This isolates how well each method handles out-of-range HoA conditions, with mean μ and standard deviation σ shown in the legend.

model are evident across all elevations, whereas the errors of the *MLP model* are at elevation bins dominated by unseen HoAs. In contrast, the elevation-dependent error of the pure physical UV model in Figure C.2 matches the theoretical expectation that the underlying uniform volume assumption fits best at the highest elevations, whereas the subsurface structure becomes increasingly more heterogeneous towards lower elevations, which results in larger model errors.

When the full range of HoA values is available during training, both hybrid and pure ML methods perform comparably. This suggests that penetration bias estimation with ML achieves high accuracy when using balanced training data, independent of the actual ML method, which is in line with the literature [2], [10]. However, excluding key HoA ranges reveals the advantage of incorporating physical constraints. The *Exponential model* leverages its physically informed vertical scattering profile to regularize parameter estimation, which helps prevent overfitting and ensures stable performance even with limited training data. In contrast, the *Weibull model*, which requires estimating two parameters, exhibits

more significant variability due to its inherent ill-posedness; its additional parameter (k_w) appears to correlate with HoA, which theoretically it should not, leading to moderate performance degradation under the *Extrapolation scenario*. The *MLP model* shows the largest increase in error variance when tested on unseen HoA conditions, indicating a higher sensitivity to out-of-distribution data.

4.6 CONCLUSION

This study introduces a hybrid framework that combines physical modeling with data-driven techniques to correct the DEM penetration bias in TanDEM-X InSAR data over Greenland. Our experiments show that hybrid and pure ML methods perform adequately when the full range of HoA values is available. However, the hybrid approach outperforms pure ML when key HoA ranges are missing during training. In particular, the *Exponential model* — with its simple one-parameter design — consistently achieves the lowest error metrics and highest stability, even under challenging *Interpolation* and *Extrapolation* scenarios.

The advantages of our hybrid approach are threefold: (1) the *Exponential model* consistently produces the lowest errors and highest stability across all HoA training scenarios, (2) incorporating physical constraints reduces the need for a highly diverse training dataset while enhancing generalization to unseen acquisition geometries, and (3) embedding the physically informed vertical scattering profile improves accuracy and interpretability, making it a robust solution for DEM bias correction.

Our findings demonstrate that embedding physical constraints into the learning process enhances performance and helps overcome challenges such as incomplete HoA coverage (i.e., limited diversity in acquisition geometry), a common issue in operational scenarios. Moreover, our hybrid framework is uniquely suited for integrating multi-modal and multi-sensor data into the physical model — a task that is typically challenging with traditional methods. This flexibility facilitates adaptation to other satellite missions (e.g., European Space Agency (ESA)'s Sentinels and Harmony) operating at different wavelengths and imaging conditions, improving performance even when high-quality reference data are scarce.

C

SUPPLEMENTARY MATERIAL

C.1 DEFINITIONS OF VERTICAL WAVENUMBER AND HOA

In our analysis of InSAR data, two key parameters describe how heights (i.e., depths) are calculated from the observed or modelled interferometric phase: the vertical wavenumber κ_z and the Height of Ambiguity (HoA). Physically, κ_z depends on the dielectric properties of snow and ice and has to account for the refraction and change in wave propagation speed in the medium, which leads to a vertical wavenumber in the (snow and ice) volume $\kappa_{z_{\text{Vol}}}$. However, TanDEM-X DEMs are produced under the *free-space* assumption, so the penetration bias correction must also adopt the *free-space* vertical wavenumber κ_z as [13]

$$\kappa_z = \frac{4\pi}{\lambda} \frac{\Delta\theta_i}{\sin\theta_i}, \tag{S1}$$

where λ denotes the radar wavelength, θ_i is the incidence angle, and $\Delta\theta_i$ is the baseline-induced angular shift.

The Height of Ambiguity (HoA), which quantifies the phase-to-height sensitivity by representing the elevation difference corresponding to a full 2π interferometric phase cycle, is defined as

$$\text{HoA} = \frac{2\pi}{\kappa_z}. \tag{S2}$$

C.2 METRIC DEFINITIONS

We evaluate model performance using standard metrics that assess bias, error magnitude, and goodness-of-fit. The following equations define these metrics:

$$\mathrm{ME} = \frac{1}{n}\sum_{i=1}^{n}(\hat{y}_i - y_i), \tag{S3}$$

$$\mathrm{MAE} = \frac{1}{n}\sum_{i=1}^{n}|\hat{y}_i - y_i|, \tag{S4}$$

$$\mathrm{MAPE} = \frac{100}{n}\sum_{i=1}^{n}\left|\frac{\hat{y}_i - y_i}{y_i}\right|, \tag{S5}$$

$$\mathrm{RMSE} = \sqrt{\frac{1}{n}\sum_{i=1}^{n}(\hat{y}_i - y_i)^2}, \tag{S6}$$

$$R^2 = 1 - \frac{\sum_{i=1}^{n}(\hat{y}_i - y_i)^2}{\sum_{i=1}^{n}(y_i - \bar{y})^2}, \tag{S7}$$

$$\mu = \frac{1}{n}\sum_{i=1}^{n} e_i, \tag{S8}$$

$$\sigma = \sqrt{\frac{1}{n}\sum_{i=1}^{n}(e_i - \mu)^2}, \tag{S9}$$

where $\hat{y}_i$ represents the predicted values, y_i denotes the corresponding reference values, and $\bar{y}$ is the mean of the reference values. Additionally, $e_i = \hat{h}_{\mathrm{InSAR}} - h_{\mathrm{ref}}$ denotes the DEM error before or after applying bias correction. The mean error μ provides insight into systematic bias, while the standard deviation σ captures the variability of the DEM error.

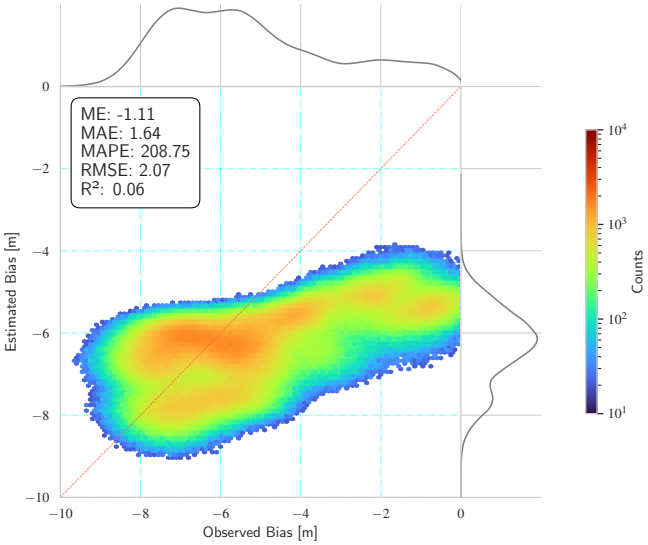

Figure C.1: 2D histograms of estimated versus observed penetration bias for the Physical (UV) model

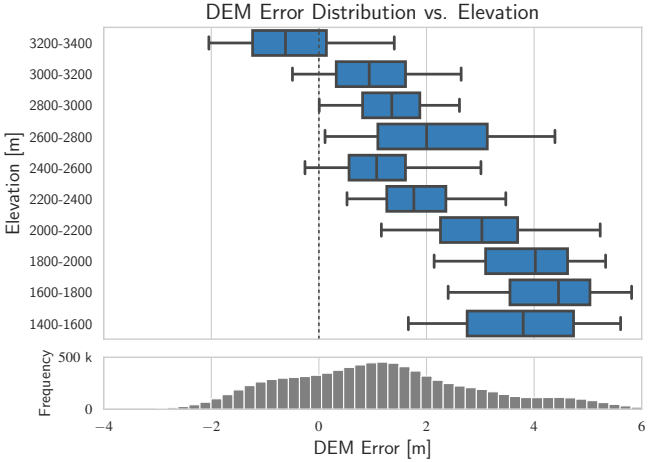

Figure C.2: Corrected DEM "using physical (UV) model" error distribution across elevation bins, computed using ATM LiDAR as reference.

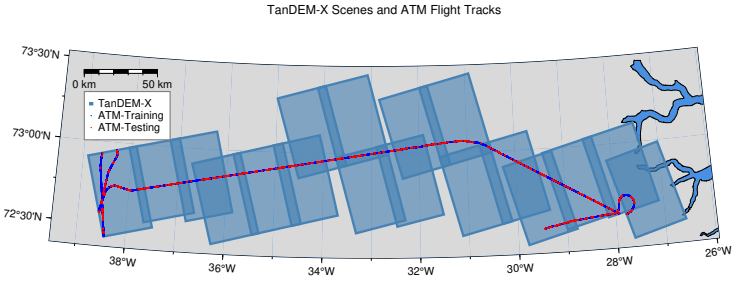

(a) All scenario

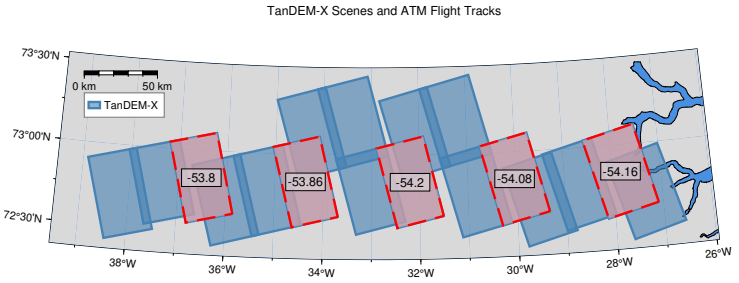

(b) Interpolation scenario

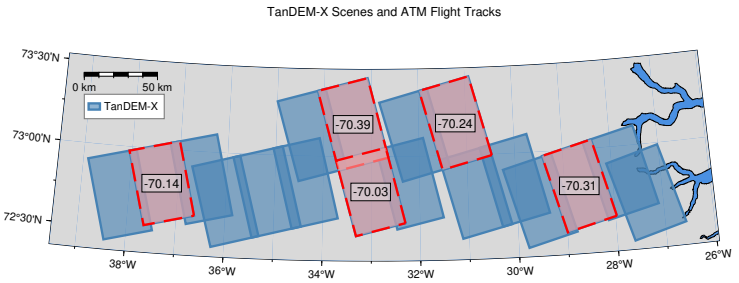

(c) Extrapolation scenario

Figure C.3: Overview of the TanDEM-X scenes (blue) and ATM flight tracks (red/blue) used for each training scenario. The ATM flight lines are split into training (blue) and testing (red) segments, ensuring coverage of different surface conditions for model evaluation. Scenes outlined in red are excluded from training under the specified HoA range. (a) *All*: uses every scene, (b) *Interpolation*: excludes HoA in $[50, 60]$ m, (c) *Extrapolation*: excludes HoA above 70 m.

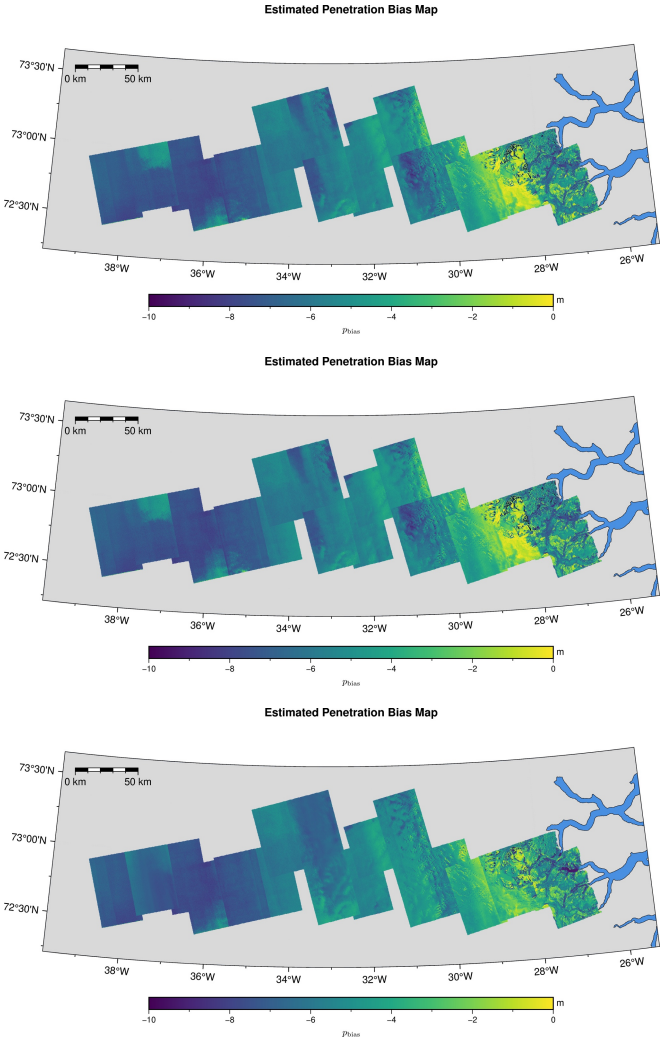

Figure C.4: Estimated penetration bias maps (continued 1/3).

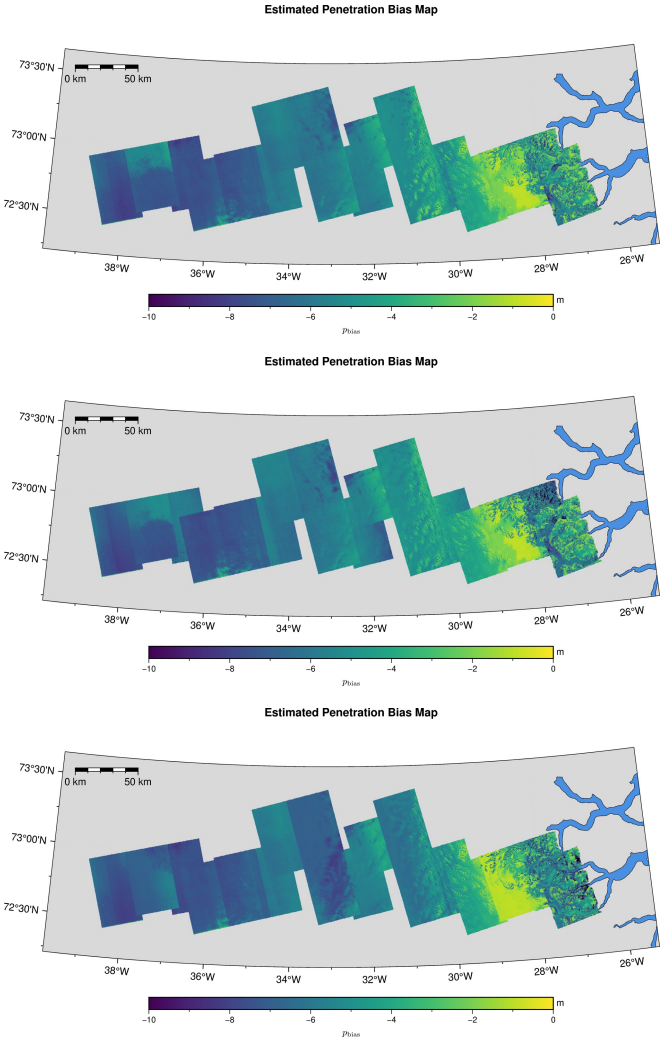

Figure C.4: Estimated penetration bias maps (continued 2/3).

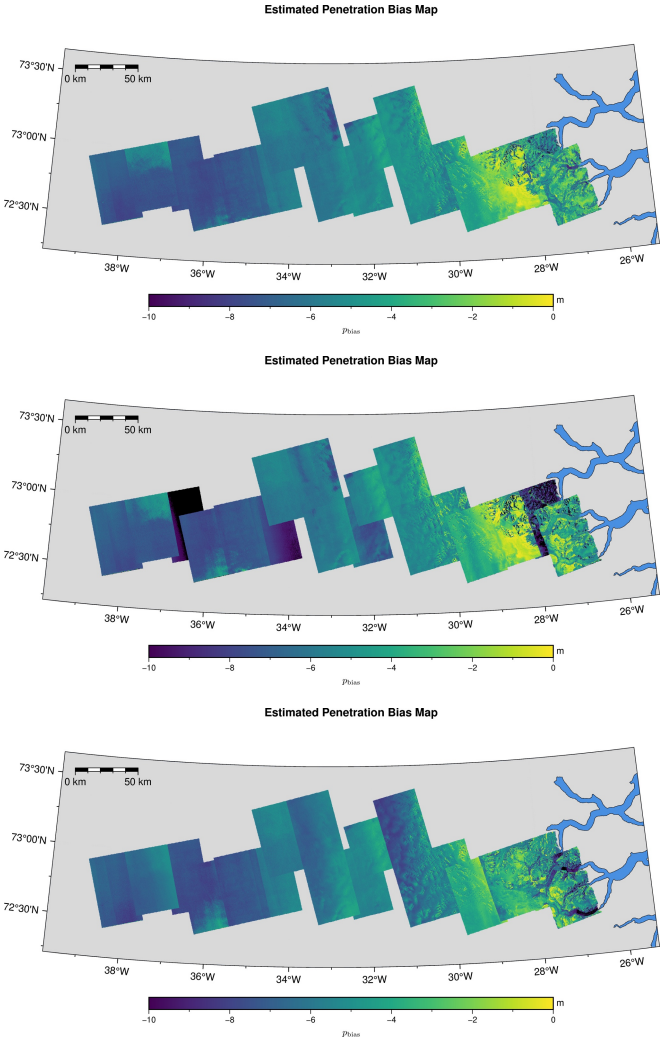

Figure C.4: Estimated penetration bias maps for the study region under three HoA training scenarios (rows) and three modeling approaches (columns). **Rows** (top → bottom): *All*, *Interpolation*, and *Extrapolation* scenarios. **Columns** (left → right): *Exponential*, *Weibull*, and *MLP* models. Each panel shows the spatial distribution of the predicted bias (in meters), with bluish colors indicating deeper penetration bias.

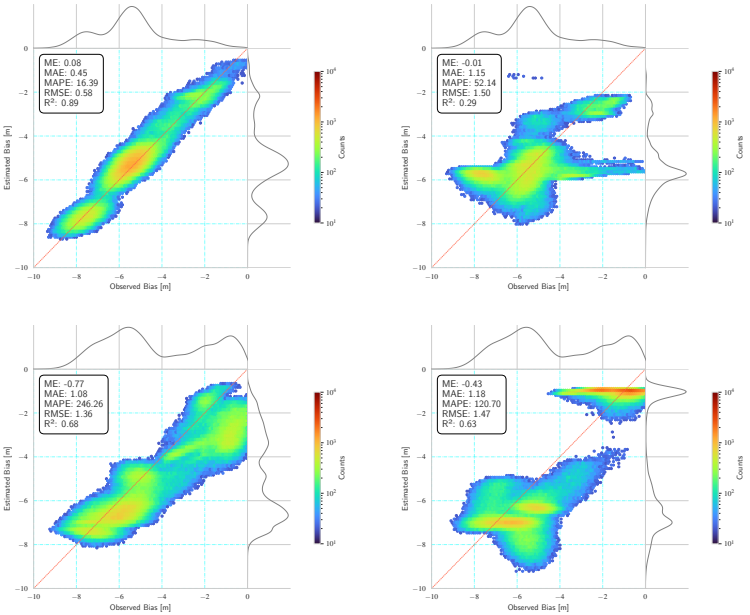

Figure C.5: Comparison of model estimations (continued 1/2).

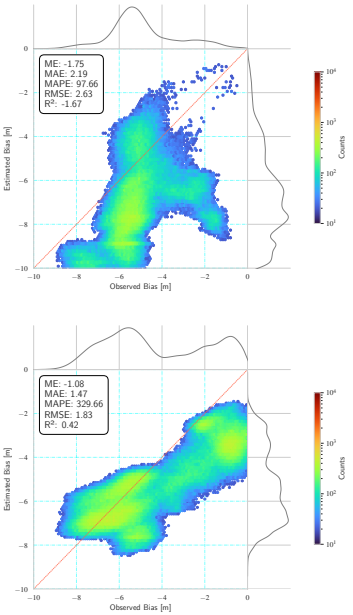

Figure C.5: Comparison of model estimations under different evaluation conditions, showing only results over the excluded (unseen) HoA scenes during training. **Columns:** (Left) Hybrid Exponential, (Middle) Hybrid Weibull, (Right) MLP model. **Rows:** (Top) *Interpolation* (excluding HoA 50–60); (Bottom) *Extrapolation* (excluding HoA > 70).

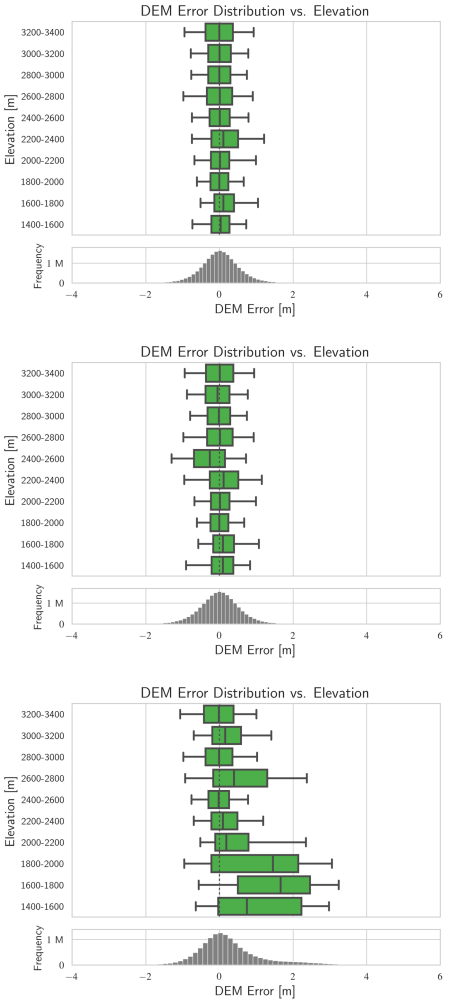

Figure C.6: Errors of corrected DEMs (continued 1/3).

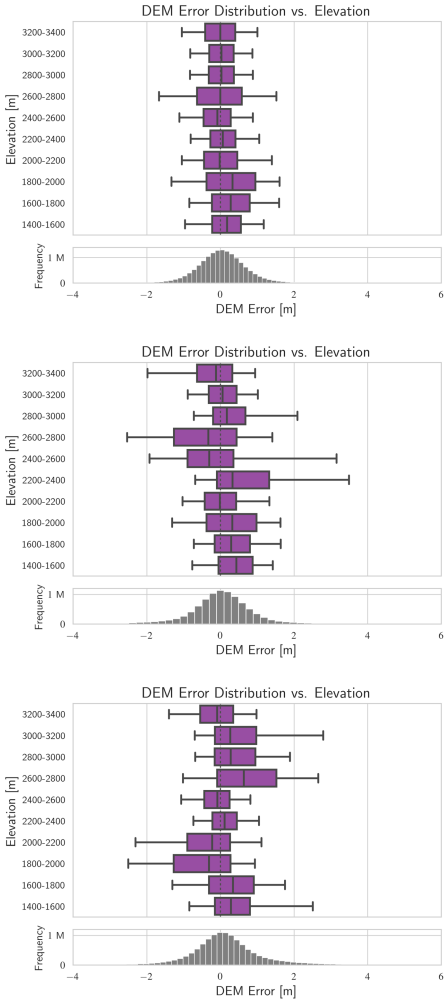

Figure C.6: Errors of corrected DEMs (continued 2/3).

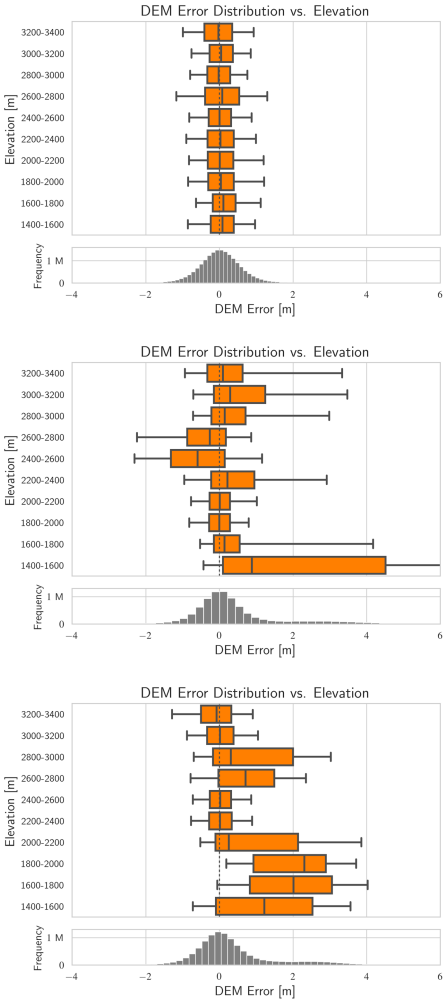

Figure C.6: Errors of the corrected DEMs, obtained by compensating the original InSAR DEMs with the estimated penetration bias using different models and training scenarios. Shown are error distributions across elevation bins, computed using ATM LiDAR as reference under three HoA training scenarios (rows) and three modeling approaches (columns). **Rows** (top → bottom): *All*, *Interpolation*, and *Extrapolation* scenarios. **Columns** (left → right): *Exponential*, *Weibull*, and *MLP* models.

REFERENCES

[1] European Space Agency and Airbus, *Copernicus DEM*, 2022 (cited on page 109).

[2] S. Abdullahi, B. Wessel, M. Huber, A. Wendleder, A. Roth, and C. Kuenzer, "Estimating Penetration-Related X-Band InSAR Elevation Bias: A Study over the Greenland Ice Sheet," *Remote Sensing*, vol. 11, no. 24, 2903, 2019. DOI: 10.3390/rs11242903 (cited on pages 109–111, 117, 118, 128).

[3] J. Dall, S. N. Madsen, K. Keller, and R. Forsberg, "Topography and penetration of the Greenland Ice Sheet measured with Airborne SAR Interferometry," *Geophysical Research Letters*, vol. 28, no. 9, 1703, 2001. DOI: 10.1029/2000GL011787 (cited on page 109).

[4] E. Rignot, K. Echelmeyer, and W. Krabill, "Penetration depth of interferometric synthetic-aperture radar signals in snow and ice," *Geophysical Research Letters*, vol. 28, no. 18, 3501, 2001. DOI: 10.1029/2000GL012484 (cited on page 109).

[5] B. Wessel, A. Bertram, A. Gruber, S. Bemm, and S. Dech, "A NEW HIGH-RESOLUTION ELEVATION MODEL OF GREENLAND DERIVED FROM TANDEM-X," *ISPRS Annals of the Photogrammetry, Remote Sensing and Spatial Information Sciences*, vol. III-7, 9, 2016. DOI: 10.5194/isprs-annals-III-7-9-2016 (cited on page 109).

[6] Y. Fan, C.-Q. Ke, and X. Shen, "A new Greenland digital elevation model derived from ICESat-2 during 2018–2019," *Earth System Science Data*, vol. 14, no. 2, 781, 2022. DOI: 10.5194/essd-14-781-2022 (cited on pages 109, 118).

[7] E. Weber Hoen and H. Zebker, "Penetration depths inferred from interferometric volume decorrelation observed over the Greenland Ice Sheet," *IEEE Transactions on Geoscience and Remote Sensing*, vol. 38, no. 6, 2571, 2000. DOI: 10.1109/36.885204 (cited on pages 110, 111, 114).

[8] J. Dall, "InSAR Elevation Bias Caused by Penetration Into Uniform Volumes," *IEEE Transactions on Geoscience and Remote Sensing*, vol. 45, no. 7, 2319, 2007. DOI: 10.1109/TGRS.2007.896613 (cited on pages 110, 111, 115).

[9] G. Fischer, K. P. Papathanassiou, and I. Hajnsek, "Modeling and Compensation of the Penetration Bias in InSAR DEMs of Ice Sheets at Different Frequencies," *IEEE Journal of Selected Topics in Applied Earth Observations and Remote Sensing*, vol. 13, 2698, 2020. DOI: 10.1109/JSTARS.2020.2992530 (cited on pages 110, 111, 115).

[10] A. B. Campos, M. Braun, and P. Rizzoli, "On the Potential of Bistatic Insar Features for Monitoring Ice Sheets Properties and Estimating Surface Elevation Bias," in *IGARSS 2024 - 2024 IEEE International Geoscience and Remote Sensing Symposium*, Athens, Greece: IEEE, 2024, 143. DOI: 10.1109/IGARSS53475.2024.10640443 (cited on pages 110, 112, 128).

[11] I. Mansour, G. Fischer, R. Hänsch, I. Hajnsek, and K. Papathanassiou, "Correction of The Penetration Bias for InSAR DEM Via Synergetic AI-Physical Modeling: A Greenland Case Study," in *IGARSS 2024 - 2024 IEEE International Geoscience and Remote Sensing Symposium*, 2024, 138. DOI: 10.1109/IGARSS53475.2024.10642748 (cited on page 110).

[12] C. Mätzler, "Applications of the interaction of microwaves with the natural snow cover," *Remote Sensing Reviews*, vol. 2, no. 2, 259, 1987. DOI: 10.1080/02757258709532086 (cited on page 111).

[13] J. J. Sharma, I. Hajnsek, K. P. Papathanassiou, and A. Moreira, "Estimation of Glacier Ice Extinction Using Long-Wavelength Airborne Pol-InSAR," *IEEE Transactions on Geoscience and Remote Sensing*, vol. 51, no. 6, 3715, 2013. DOI: 10.1109/TGRS.2012.2220855 (cited on pages 111, 114, 131).

[14] A. Becker Campos, P. Rizzoli, J. L. Bueso-Bello, and M. Braun, "An Unsupervised Deep Learning Approach for Monitoring the Snow Facies of the Greenland Ice Sheet with InSAR TanDEM-X Data," in *EUSAR 2024; 15th European Conference on Synthetic Aperture Radar*, 2024, 175 (cited on page 112).

[15] S. Kurz, H. De Gersem, A. Galetzka, A. Klaedtke, M. Liebsch, D. Loukrezis, S. Russenschuck, and M. Schmidt, "Hybrid modeling: towards the next level of scientific computing in engineering," *Journal of Mathematics in Industry*, vol. 12, no. 1, 8, 2022. DOI: 10.1186/s13362-022-00123-0 (cited on page 112).

[16] G. E. Karniadakis, I. G. Kevrekidis, L. Lu, P. Perdikaris, S. Wang, and L. Yang, "Physics-informed machine learning," *Nature Reviews Physics*, vol. 3, no. 6, 422, 2021. DOI: 10.1038/s42254-021-00314-5 (cited on page 112).

[17] V. M. Krasnopolsky and M. S. Fox-Rabinovitz, "Complex hybrid models combining deterministic and machine learning components for numerical climate modeling and weather prediction," *Neural Networks*, vol. 19, no. 2, 122, 2006. DOI: 10.1016/j.neunet.2006.01.002 (cited on page 112).

[18] G. Weisz. "Hybrid Modeling - Combining Physics and Machine Learning to Understand Multiphase Transient Flow," Turbulent Flux, Accessed: Apr. 25, 2023. [Online]. Available: https://turbulentflux.com/combining-physics-and-machine-learning-to-understand-multiphase-transient-flow/ (cited on page 112).

[19] P. B. Gibson, W. E. Chapman, A. Altinok, L. Delle Monache, M. J. DeFlorio, and D. E. Waliser, "Training machine learning models on climate model output yields skillful interpretable seasonal precipitation forecasts," *Communications Earth & Environment*, vol. 2, no. 1, 1, 2021. DOI: 10.1038/s43247-021-00225-4 (cited on page 112).

[20] I. Mansour, K. Papathanassiou, R. Hänsch, and I. Hajnsek, "Hybrid Machine Learning Forest Height Estimation From TanDEM-X InSAR," *IEEE Transactions on Geoscience and Remote Sensing*, vol. 63, 1, 2025. DOI: 10.1109/TGRS.2024.3520387 (cited on page 112).

[21] S. Cloude and K. Papathanassiou, "Polarimetric SAR interferometry," *IEEE Transactions on Geoscience and Remote Sensing*, vol. 36, no. 5, 1551, 1998. DOI: 10.1109/36.718859 (cited on page 113).

[22] P. Rosen, S. Hensley, I. Joughin, F. Li, S. Madsen, E. Rodriguez, and R. Goldstein, "Synthetic aperture radar interferometry," *Proceedings of the IEEE*, vol. 88, no. 3, 333, 2000. DOI: 10.1109/5.838084 (cited on page 113).

[23] S. Cloude, *Polarisation: Applications in Remote Sensing*. Oxford University Press, 2009. DOI: 10.1093/acprof:oso/9780199569731.001.0001 (cited on page 113).

[24] J. Askne, P. Dammert, L. Ulander, and G. Smith, "C-band repeat-pass interferometric SAR observations of the forest," *IEEE Transactions on Geoscience and Remote Sensing*, vol. 35, no. 1, 25, 1997. DOI: 10.1109/36.551931 (cited on page 113).

[25] H. Zebker and J. Villasenor, "Decorrelation in interferometric radar echoes," *IEEE Transactions on Geoscience and Remote Sensing*, vol. 30, no. 5, 950, 1992. DOI: 10.1109/36.175330 (cited on page 113).

[26] J. O. Hagberg, L. M. Ulander, and J. Askne, "Repeat-pass SAR interferometry over forested terrain," *IEEE Transactions on Geoscience and Remote Sensing*, vol. 33, no. 2, 331, 1995. DOI: 10.1109/TGRS.1995.8746014 (cited on page 113).

[27] R. Bamler and P. Hartl, "Synthetic aperture radar interferometry," *Inverse Problems*, vol. 14, no. 4, R1, 1998. DOI: 10.1088/0266-5611/14/4/001 (cited on page 113).

[28] G. Krieger, A. Moreira, H. Fiedler, I. Hajnsek, M. Werner, M. Younis, and M. Zink, "TanDEM-X: A Satellite Formation for High-Resolution SAR Interferometry," *IEEE Transactions on Geoscience and Remote Sensing*, vol. 45, no. 11, 3317, 2007. DOI: 10.1109/TGRS.2007.900693 (cited on page 113).

[29] F. Gatelli, A. Monti Guamieri, F. Parizzi, P. Pasquali, C. Prati, and F. Rocca, "The wavenumber shift in SAR interferometry," *IEEE Transactions on Geoscience and Remote Sensing*, vol. 32, no. 4, 855, 1994. DOI: 10.1109/36.298013 (cited on page 113).

[30] M. Martone, B. Bräutigam, and G. Krieger, "Quantization Effects in TanDEM-X Data," *IEEE Transactions on Geoscience and Remote Sensing*, vol. 53, no. 2, 583, 2015. DOI: 10.1109/TGRS.2014.2325976 (cited on page 113).

[31] G. Fischer, M. Jäger, K. P. Papathanassiou, and I. Hajnsek, "Modeling the Vertical Backscattering Distribution in the Percolation Zone of the Greenland Ice Sheet With SAR Tomography," *IEEE Journal of Selected Topics in Applied Earth Observations and Remote Sensing*, vol. 12, no. 11, 4389, 2019. DOI: 10.1109/JSTARS.2019.2951026 (cited on page 115).

[32] O. Alexandrov, S. McMichael, and R. Beyer, *IceBridge DMS L3 Ames Stereo Pipeline Photogrammetric DEM, Version 1*, 2018. DOI: 10.5067/HYV1T0G7LVHE (cited on page 118).

Part III

Conclusions

5

CONCLUSIONS AND OUTLOOK

This thesis introduces novel hybrid AI-physical modeling frameworks to enhance parameter retrieval from InSAR data and comprises three closely related studies—focused on the physical modeling aspects—on the estimation of forest height and the snow/ice penetration bias. This thesis demonstrates that physical models combined with machine learning greatly enhance the accuracy, interpretability, and generalizability of InSAR parameter retrieval.

This chapter summarizes the main findings of the three studies presented in this thesis. The research questions presented in Section 1.4 are addressed in each study. Following the summary of each study, potential directions for future research are discussed.

5.1 HYBRID ML FOREST HEIGHT ESTIMATION FROM TANDEM-X INSAR

Our investigation demonstrates that the integration of ML with physical models requires careful consideration of the underlying physical relationships. The MLP architecture was specifically designed to predict physically meaningful vertical reflectivity profiles while maintaining the established relationship between these profiles and forest height estimates. This approach preserves the interpretability of the physical model while leveraging ML's ability to handle complex, non-linear relationships in the input feature space, thus addressing the limitations of both physical models and machine learning. *Model-C*, trained over the Lopé site with three TanDEM-X acquisitions (corresponding to three different baselines) and using seven Legendre polynomials, demonstrated the best performance with consistent RMSE values between 8.70 m and 11.34 m across different test sites, showing strong generalization capabilities while maintaining physical consistency in the vertical reflectivity profile predictions.

5.1.1 *Addressing the Research Questions*

1. How can machine learning be effectively integrated with physical models to improve forest height estimation from single-baseline InSAR data?

The study demonstrated that machine learning can be effectively integrated with physical models through a hybrid framework that maintains both adaptability and physical consistency. The MLP was trained to predict Legendre polynomial coefficients from InSAR features while maintaining the established relationship between these profiles and forest height. This approach successfully bridged the gap between data-driven flexibility and physical model constraints, achieving an overall RMSE over Lopé of 8.84 m for *Model-C*. The integration proved particularly effective in handling complex forest structures, where traditional physical models often struggled to account for the underlying challenging topography.

2. What improvements in accuracy and generalization can be achieved through hybrid modeling compared to traditional approaches?

The hybrid framework demonstrated substantial improvements in both accuracy and generalization capabilities. Using only three baselines for training from Lopé, where mean forest heights differ significantly from those at the test sites, the model successfully generalized to both Mabounié and Rabi. Despite the height distribution mismatch in the training data, the framework maintained robust accuracy when validated against LiDAR reference data, with *Model-C* achieving MAE values ranging from 7.80 to 8.73 m and RMSE values between 9.84 and 11.10 m in Mabounié, and with MAE values ranging from 6.81 to 8.95 m and RMSE values between 8.70 and 11.34 m in Rabi. This demonstrates the model's ability to extrapolate beyond its training height distribution while maintaining stable performance across different incidence angles and baselines (HoA ranging from 52 m to 95 m).

3. How does the framework perform across different forest types and terrain conditions?

Testing across multiple tropical sites reveals consistent performance across varying forest conditions and topographic situations. The framework demonstrates particular strength in handling both positive and negative slopes, as it derives the profile as a function

of the slope and other features. Traditional methods often fail due to simplified assumptions that do not account for the underlying topography in the vertical structure for limited observation spaces. While performance remains robust across most conditions, some limitations emerge in extreme topographic situations from the ascending and descending orbits, providing important insights for future improvements.

5.2 HYBRID FOREST HEIGHT ESTIMATION FROM TANDEM-X AND LANDSAT DATA

This study extended the hybrid framework by incorporating multi-spectral Landsat data with TanDEM-X interferometric coherence to enhance forest height estimation. Traditional single-modality approaches often struggle to capture subtle variations in forest structure that affect height estimation. The integration addresses key limitations in single-sensor approaches, particularly in cases where either optical or radar data alone provide insufficient information for accurate forest height estimation. By combining complementary information sources, we demonstrate significant improvements in estimation accuracy while maintaining the interpretability of physical models.

The enhanced framework leverages both the structural information contained in Landsat spectral bands (Red, NIR, SWIR1, SWIR2) alongside InSAR features. Following the same training strategy as *Model-C*, *Model-D* extends the input feature space by incorporating these Landsat spectral bands. Results demonstrated significant improvements in forest height estimation accuracy, with a 13.5% reduction in RMSE and 16.6% reduction in MAE compared to the InSAR-only approach. The study also explored how multi-modal integration improved performance across challenging terrains and acquisition geometries. Validation results demonstrate marked improvements in accuracy and robustness compared to single-sensor approaches.

5.2.1 *Addressing the Research Questions*

1. How can optical multi-spectral data be effectively integrated into the hybrid modeling framework while maintaining physical consistency?

The integration strategy focuses on preserving the physical relationships inherent in both radar and optical measurements. Rather than treating optical data as auxiliary information, we developed a unified framework that explicitly accounts for the complementary nature of both data sources by using the Landsat spectral bands (used for deriving the tree cover loss maps) to inform the prediction of vertical reflectivity profiles through the MLP, while maintaining the role of the physical model in forest height estimation. This joint learning approach allows the framework to leverage the sensitivity of optical data to canopy structure and density while preserving the physical relationship between vertical reflectivity profiles and interferometric coherence.

2. What improvements in forest height estimation accuracy can be achieved through multi-modal data fusion?

Quantitative validation demonstrates meaningful, significant improvements in estimation accuracy through multi-modal data fusion. The integration of Landsat data leads to reduced estimation errors across various forest conditions and acquisition scenarios. While the numerical improvements in RMSE (from 8.84 m to 7.65 m) and MAE (from 6.79 m to 5.66 m) might appear modest, their significance extends beyond these metrics. The key advancement lies in the framework's enhanced capability to adapt to diverse forest conditions and complex terrain. From a mathematical perspective, *Model-C*'s solution space, defined solely by InSAR features, represents a subset of the larger solution space accessible to *Model-D*. By augmenting the input feature space with Landsat data, *Model-D* effectively spans a higher-dimensional solution space that fully encompasses the solutions of *Model-C* while enabling additional degrees of freedom in predicting vertical reflectivity profiles. This expanded solution space is evident in the 2-D histogram for the coherence vs. $\kappa_z \cdot h_v$ regions for the different cases, where the additional dimensionality allows for more nuanced profile estimation. Thus, it translates to robust performance across varying terrain conditions, as demonstrated by the symmetric error distributions across both positive and negative slopes.

3. How does the multi-modal framework perform under different acquisition geometries and terrain conditions?

The multi-modal framework shows enhanced robustness across varying acquisition geometries and terrain conditions. While In-

SAR measurements are inherently sensitive to topography due to their side-looking geometry, optical data, with its near-nadir viewing geometry and limited ground penetration in dense canopies, provide complementary structural information. This complementarity helps maintain consistent performance, as evidenced by near-zero bias for slopes between -10° and +10°. The framework leverages both data sources to achieve stable predictions across varying terrain conditions without reducing the inherent topographic sensitivity of the InSAR measurements themselves.

5.3 HYBRID AI–PHYSICAL MODELING FOR X-BAND INSAR DEMS: GREENLAND

This study adapts the developed hybrid modeling framework to address the penetration bias in X-band InSAR DEMs over ice sheets, with a specific application to Greenland. The work combines parametric physical modeling with machine learning to correct systematic elevation errors caused by radar penetration into snow and ice. The proposed framework combines parametric vertical scattering profiles (Exponential and Weibull) with an MLP that predicts profile parameters from InSAR features, enabling more accurate penetration bias correction while maintaining physical interpretability.

Validation using three distinct training scenarios, each defined by the inclusion or exclusion of different acquisition geometries, demonstrates the framework's ability to generalize across varying conditions. Testing over Greenland's ice sheet using TanDEM-X data shows significant reductions in both both mean and standard deviation of DEM errors compared to conventional correction methods (pure physical modeling and pure ML approaches). The framework maintains robust performance even when trained on data with limited diversity in acquisition parameters.

5.3.1 *Addressing the Research Questions*

1. How can hybrid modeling effectively address penetration bias in X-band InSAR DEMs over ice sheets?

Our approach combines parametric physical modeling with ML-driven parameter estimation, enabling a more accurate estimation

of penetration bias while maintaining physical consistency. This is achieved by training an MLP to predict the parameters of the physical model, which describes the vertical scattering structure in the subsurface of the ice sheet and thus allows for the estimation of the penetration bias based on physical principles. The ML components of the framework can effectively learn and correct deviations from the idealized physical model assumptions across different elevation ranges. While a pure physical model applies the same assumptions uniformly, our hybrid approach adapts these assumptions from the InSAR features to compensate for varying conditions of snow, firn, and ice at different elevations. This adaptive capability results in significant reductions in systematic elevation errors (as low as 0.52 m with the exponential model) compared to pure physical model corrections.

2. *What advantages does the hybrid approach offer over purely physical or purely ML methods*

Both the hybrid approach and the pure ML method show clear advantages over the pure physical model, due to the involved training step with reference data. In line with other literature, this suggests that the estimation of penetration bias can be effectively addressed with ML and statistical methods, provided that the training data is sufficiently large and well-balanced, thereby outperforming pure physical models. The real advantage of the hybrid framework developed in this thesis over pure ML approaches is its superior generalization, particularly when the training data has limited diversity in acquisition parameters. This is demonstrated by excluding certain Height of Ambiguity ranges from the training data. The hybrid framework maintained significantly better estimation performance on those acquisition geometries that were not part of the training, even in the extrapolation case, whereas the pure ML clearly degrades in these situations. The integration of physical constraints helps to prevent unrealistic corrections while allowing sufficient flexibility to address complex penetration scenarios. This balance is crucial for operational applications over large ice sheet areas.

3. *How well does the framework generalize across different acquisition geometries and surface conditions?*

Analysis across multiple test scenarios (Interpolation and Extrapolation) demonstrates the framework's robust generalization

capabilities. For acquisition geometries, both hybrid models maintain stable performance when tested on excluded scenes, with the Exponential model achieving remarkably consistent error distributions (standard deviations of 0.67-0.97 m) and minimal bias (means of 0.03-0.28 m). The framework demonstrates particular strength in extrapolation scenarios, where, despite the challenge of predicting beyond the training range, it maintains reliable performance. This represents a significant improvement over pure physical models, which tend to overestimate shallower penetration bias, and over pure ML models which are not able to adequately predict unseen input features. The framework's ability to accurately adjust penetration estimates across the elevation range from Greenland's Summit to its East coast, while maintaining reliable performance for unseen acquisition geometries, makes it particularly valuable for large-scale ice sheet DEM generation where penetration conditions vary substantially with elevation.

5.4 SUMMARY AND OUTLOOK OF THE THESIS

Within this work, advanced hybrid AI-physical modeling frameworks are developed to retrieve crucial environmental parameters from InSAR observations. The developed frameworks are applied to two important applications: forest height estimation for ecosystem monitoring and penetration bias correction over ice sheets. In the case of forest height estimation, two specific applications are further investigated: one used only the single-pass TanDEM-X InSAR data, while the other integrated multi-modal data.

For forest height estimation, the proposed framework effectively improves the accuracy of the physical model in inferring forest height from the vertical reflectivity profile using TanDEM-X InSAR data. The performance was further improved by employing the Landsat multi-spectral data as complementary input features. Expanding the application of the proposed framework to the cryosphere domain demonstrated robust generalized estimation of the penetration bias over the Greenland ice sheet, adapting to varying penetration bias while maintaining consistent performance across different acquisition geometries.

A primary area for exploration lies in refining the integration of physical models within hybrid frameworks. For forest applications,

this involves developing a more sophisticated vertical structure profile to include multi-layer models that account for more complex forest structures, thereby better capturing the characteristics of the canopy structure. For ice sheet applications, a similar improvement can be made by introducing more sophisticated scattering models that represent multiple snow, firn, and ice layers, as well as varying density profiles. However, integrating such advanced physical models with the ML architecture would require them to be differentiable so that end-to-end training can be achieved along with physical consistency. This necessitates further development of physics-guided regularization, loss functions, and constraints. By further refining the physical models within the hybrid framework, the predicted parameters can more effectively preserve their physical knowledge and meaning across different environmental conditions.

Additionally, the successful integration of optical and InSAR data in the forest height estimation study indicates a promising potential for the fusion of multi-modality data. Combining multi-modal data for parameter retrieval can significantly improve the robustness of model predictions when the data quality or acquisition conditions vary. Future research should focus on developing more sophisticated fusion architectures that can adaptively weigh different data sources based on their quality and relevance. This could involve attention mechanisms that learn to focus on the most relevant features from each modality, which is particularly important when dealing with varying acquisition conditions or data quality. The framework demonstrates potential for integrating the GEDI waveform for the stratification of the vertical reflectivity profile and its application in upcoming missions such as BIOMASS and NISAR. The GEDI waveform could guide the learning process for vertical reflectivity profiles in forest applications, enabling informed profile transformations between different sensors. The framework would be valuable for the upcoming BIOMASS and NISAR missions, offering opportunities for cross-validation and enhanced parameter retrieval through complementary observations.

OUTLOOK: NEW DATASETS AND PROCESSES As new satellite missions and datasets become available, such as BIOMASS, NISAR, GEDI continuity, and ICESat-2, the frameworks developed in this

thesis can be further advanced to address additional scientific questions. These upcoming datasets will provide unprecedented temporal and spatial coverage, enabling the investigation of dynamic processes that drive environmental change. For forests, this includes improved monitoring of succession, disturbance, and carbon dynamics, leveraging the unique sensitivity of each mission to different aspects of forest structure and biomass. In the cryosphere, missions such as ICESat-2 and NISAR will enable detailed studies of firn compaction, melt–refreeze cycles, and surface mass balance. The integration of these new data sources within hybrid modeling frameworks will enable a deeper understanding of the mechanisms underlying observed changes, moving beyond static parameter retrieval to dynamic process inference.

MULTIFREQUENCY SAR OUTLOOK Beyond the fusion of different sensor modalities, the exploitation of multifrequency SAR data (e.g., X-, C-, L-, and P-band) presents a promising direction for future research. Combining different radar wavelengths will enable more comprehensive retrievals of vertical structure, as each frequency penetrates to different depths and interacts uniquely with vegetation and snow/ice layers. Multifrequency SAR data fusion will improve the robustness of parameter retrieval, reduce ambiguities arising from single-frequency observations, and provide enhanced sensitivity to both canopy and subcanopy features in forests, as well as to multi-layer structures in snow and ice. Advancing hybrid frameworks to jointly exploit multifrequency SAR will be key to achieving more accurate and reliable environmental monitoring.

LIMITATIONS OF THE CURRENT METHODS Despite the demonstrated advances, several limitations remain in the current hybrid frameworks. First, the single-baseline InSAR configuration leads to underdetermination in the retrieval of vertical profiles, limiting the ability to resolve complex structures without additional information. The frameworks are also dependent on the quality, representativeness, and amount of training data, making generalization to novel sites or conditions challenging if the training set is limited or biased. Site specificity remains an issue, as models trained in one region may not always transfer seamlessly to

others with different environmental characteristics. Scalability is another concern, as the computational cost of training and applying complex hybrid models to large-scale datasets can be substantial. Addressing these limitations will require further research into more efficient architectures, improved transfer learning strategies, and the integration of additional constraints or priors.

Operational considerations for large-scale implementation require attention to computational efficiency. Developing optimized processing chains will be crucial, potentially leveraging cloud computing infrastructure to handle large datasets. Several practical problems need to be addressed, such as the proper handling of temporal alignment and missing data, the careful development of cross-validation protocols and uncertainty quantification methods, standardized interfaces, and streaming data pipelines. These operational considerations become particularly important as we move towards real-time monitoring.

Although only two applications are presented in the thesis, the potential of these frameworks can be further adapted to other domains. The methodology could be adapted to various ecosystems, including dense tropical forests and sparse boreal landscapes, as well as different cryospheric environments, such as the Antarctic and alpine glaciers. It could also be extended to various regions of Greenland. Cross-domain applications enable transfer learning, in which principles developed in one domain are applied to another. This is demonstrated by transferring it from forest to ice applications. This could include applications in biomass estimation or snow depth monitoring.

A SYNTHESIS VIEW: HYBRID AI–PHYSICAL MODELING AS A UNIFYING PARADIGM The hybrid AI–physical frameworks developed in this thesis are not merely a sum of the three studies but explore a unifying paradigm that bridges data-driven and physical modeling approaches across Earth system domains. This inherently transferable approach allows the methodologies and insights gained in one domain (e.g., forests) to inform and accelerate progress in others (e.g., the cryosphere). The scientific importance of this paradigm lies in its ability to leverage the strengths of both AI and physical modeling, enabling robust, interpretable, and generalizable solutions to complex Earth observation challenges. As new

data sources and scientific questions emerge, hybrid frameworks will play a central role in advancing the understanding of dynamic Earth system processes.

In summary, advancements in hybrid AI-physical modeling frameworks provide a solid foundation for various Earth observation applications. Integrating physical models with data-driven techniques in a hybrid modeling framework allows for addressing current and future challenges in remote sensing. In particular, when exploring synergies among the different sensors and in scenarios with limited availability of reference data, the continued development of these methodologies will be crucial for advancing our understanding of Earth system processes and improving our ability to monitor and model environmental changes.

PUBLICATIONS

Peer-reviewed publications:

[1] I. **Mansour**, K. Papathanassiou, R. Hänsch, and I. Hajnsek, "Hybrid Machine Learning Forest Height Estimation From TanDEM-X InSAR," *IEEE Transactions on Geoscience and Remote Sensing*, vol. 63, 1, 2025. DOI: 10.1109/TGRS.2024.3520387.

[2] I. **Mansour**, G. Fischer, R. Hänsch, and I. Hajnsek, "Hybrid AI-physical Modeling for Penetration Bias Correction in X-band InSAR DEMs: A Greenland Case Study," 2175, 2025. DOI: 10.1109/CVPRW67362.2025.00205.

[3] I. **Mansour**, K. Papathanassiou, R. Hänsch, and I. Hajnsek, "Hybrid Machine Learning Model for Forest Height Estimation from TanDEM-X and Landsat Data," *IEEE Geoscience and Remote Sensing Letters*, submitted in March 2025.

Conference contributions:

[4] I. **Mansour**, G. Fischer, R. Hänsch, I. Hajnsek, and K. Papathanassiou, "Correction of The Penetration Bias for InSAR DEM Via Synergetic AI-Physical Modeling: A Greenland Case Study," in *IGARSS 2024 - 2024 IEEE International Geoscience and Remote Sensing Symposium*, 2024, 138. DOI: 10.1109/IGARSS53475.2024.10642748.

[5] L. M. Albrecht, N. Basargin, I. **Mansour**, R. Guliaev, N. Romero Puig, M. Pardini, and K. Papathanassiou, "Characterization of Forest Structure Changes Exploiting TanDEM-X and GEDI Synergies," in *International Geoscience and Remote Sensing Symposium (IGARSS)*, Athens, Greece: IEEE, 2024, 1.

[6] I. **Mansour**, K. Papathanassiou, R. Hänsch, and I. Hajnsek, "Synergizing AI and Physical Models for TanDEM-X InSAR Forest Height Estimation: A Hybrid Approach over the Gabon," in *TerraSAR-X / TanDEM-X Science Team Meeting 2023*, 2023.

[7] I. **Mansour**, K. Papathanassiou, R. Hänsch, and I. Hajnsek, "Combining AI Techniques with Physical Models: Forest Height Inversion from TanDEM-X InSAR Data Using a Hybrid Modeling Approach," in *BioGeoSAR Book of Abstracts*, 2023.

[8] I. **Mansour**, K. Papathanassiou, R. Hänsch, and I. Hajnsek, "Machine Learning in Model-Based Forest Height Inversion," in *POLinSAR Online Abstracts*, Proceedings of the ESA POLinSAR Workshop, 2023, 2023.

[9] I. **Mansour**, K. P. Papathanassiou, R. Haensch, and I. Hajnsek, "Towards a Symbiosis of Model-Based and Machine Learning Forest Height Estimation based on TanDEM-X InSAR," in *Proceedings of the European Conference on Synthetic Aperture Radar, EUSAR*, 2022.